CO_2 SEQUESTRATION:
CAPACITY, SECURITY, & ENHANCED GAS RECOVERY
IN CENTRAL NEW YORK STATE

NYSERDA Agreement # 10501

Task 6, Part B (Tasks 6.4, 6.5, 6.6 and 6.7)
Final Report, December 23, 2011
Final Revised Report, January 16, 2013

Contractor
Research Foundation of SUNY, on behalf of the University at Buffalo

Project Director and Editor: Dr. Robert Jacobi,
University at Buffalo
Geology Department, 411 Cooke Hall
Buffalo, New York 14260
(716) 645-4294
Email:rdjacobi@buffalo.edu

Co-Project Director: Dr. Terry Jordan
Department of Earth & Atmospheric Sciences
Snee Hall
Cornell University
Ithaca, New York 14853-1504

Co-Project Director: Rick Frappa
AMEC Geomatrix
90B John Muir Drive, Suite 104
Amherst, NY 14228

Co-Principal Investigators
Dr. Matt Becker (UB), Dr. Larry Brown (Cornell), Dr. Bea Csatho (UB),
Dr. Lou Derry (Cornell), Jason Phipps Morgan (Cornell)

Primary Funding from:
New York State Energy Research and Development Authority
Additional Sponsors:
AES, Anschutz, Fortuna, Norse Energy

Submitted to:
Dr. John Martin and Amanda Stevens, NYSERDA Project Managers
NYS Energy Research and Development Authority
17 Columbia Circle
Albany, NY 12203-6399

NOTICE

This report was prepared by Dr. Robert Jacobi, Dr. Terry Jordan, Rick Frappa, Dr. Matt Becker, Dr. Larry Brown, Dr. Bea Csatho, Dr. Lou Derry, and Jason Phipps Morgan in the course of performing work contracted for and sponsored by the New York State Energy Research and Development Authority and AES, Anschutz, Fortuna, and Norse Energy (hereafter the "Sponsors"). The opinions expressed in this report do not necessarily reflect those of the Sponsors or the State of New York, and reference to any specific product, service, process, or method does not constitute an implied or expressed recommendation or endorsement of it. Further, the Sponsors and the State of New York, and the contractor make no warranties or representations, expressed or implied, as to the fitness for particular purpose or merchantability of any product, apparatus, or service, or the usefulness, completeness, or accuracy of any processes, methods, or other information contained, described , disclosed, or referred to in this report. The Sponsors, the State of New York, and the contractor make no representation that the use of any product, apparatus, process, method, or other information will not infringe privately owned rights and will assume no liability for any loss, injury, or damage resulting from, or occurring in connection with, the use of information contained, described, disclosed, or referred to in this report.

ABSTRACT

The overarching goals of this research project are to determine 1) the CO2 capacity of the geological units in the central New York State region, 2) the feasibility of enhanced gas recovery via CO2 injection, and 3) the methodologies of measuring long-term security of the CO2 sequestration bedrock system. In order to accomplish these goals, the UB/Cornell/Geomatrix research groups are concentrating on: 1) traditional geological unit characterization, based on well logs and samples (including well cuttings and core), 2) seismic reflection analyses of the stratigraphy, sedimentology, and faulting of the units, 3) analysis of potential seals for the CO2 sequestration, 4) modeling of H2O-NaCl-CO2 fluid flow in reservoirs, including fracture modeling using TOUGH2 code, geochemical modeling using EOS and coupled hydrodynamic-geochemical finite element modeling, 5) compilation in a GIS environment all the fracture and fault data in the region of interest, 6) identification of lineaments from available satellite images, DEMs, and aeromagnetics, and 7) using published literature as a source to determine the optimal seismic wave propagation methodology to monitor CO2 flooding in the geological units. In Task 6.2 Jacobi, Zelazny, and Csatho (University at Buffalo) manipulated ASTER and DEM images in order to identify lineaments that might reveal both the fabric of the fracture sets across the entire project area and the major fault systems. Analyses of the resulting lineament database included determining the spatial density of all the lineaments, as well as the density of "filtered" lineaments—those of a particular orientation. The lineaments trend primarily NE and NW in both ASTER and DEM images across the entire project area. Faults can be recognized in the strings of linked density highs in the filtered density ASTER and DEM data. It appears that most, or all, of the AES power plants in central NYS are close to a relatively high density of lineaments that might indicate fault systems.

KEY WORDS

CO2 sequestration, lineaments, ASTER, DEM, Appalachian Basin

TABLE OF CONTENTS

LIST OF FIGURES

LIST OF TABLES

SUMMARY

The rationale for lineament extraction from remotely sensed images (ASTER and Landsat) and digital elevation models (DEMs) in the project area that covers much of central New York State was that the lineaments might reveal both the fabric of the fracture sets across the entire project area (similar to that observed in outcrop) and reveal the major fault systems. ASTER, Landsat and DEM images were manipulated for ease of identification of lineaments ASTER image processing included georeferencing, layer stacking, masking, georeferenced mosaicing, principal components (PC) transformation, and a low pass Gaussian filtering. A color composite of band combination of R(2), G(3N), B(1) provided the greatest color contrast for extracting linear features and the PC band combination of R(PC2), G(PC1), B(PC3) provided the best overall image in terms of enhanced linear features and tonal differences. For the 10 m resolution DEMs a solar elevation angle of 25° was used for hillshading because lower sun angles were more effective in enhancing subtle topographic changes in low relief regions and the illumination angle of 0° was utilized for the entire project area. After testing Landsat against ASTER, Landsat was dropped from the program for lineament identification across the project area because of the superior lineament recognition available with the ASTER images. Lineaments were identified and digitized at various scales from 1:25,000 (Cayuga subset); 1:65,000 (the test Grid 1) and 1:125,000 (entire project area), and the minimum length of digitized lineaments was 0.5 km, 0.5 km and 1 km, respectively. Weekly QC was performed to maintain consistency in lineament identification.

Analyses of the resulting lineament data included determining the spatial density of all the lineaments, as well as the density of "filtered" lineaments—those of a particular orientation. The present lineament data was also tested against previous lineament studies in the same region and against previously published fracture data and proposed/observed faults.

The lineaments that were identified and digitized at a scale of 1:125,000 have dominant trends of NE and NW in both ASTER and DEM images across the entire project area. In the more detailed Cayuga subset where lineaments were digitized at a scale of 1:25,000, the ASTER lineament trends are similar to those in the project area as a whole. The prevalence and the orthogonality of the dominant lineaments might suggest that they delineate a single fracture fabric for the entire project area. However, in the eastern focus area, the NE and NW lineament trends do not correlate with the observed fracture set trends: Set II fractures strike WNW and Set I fractures strike NNE/N. Set III (J1) fractures that strike ENE (65^0) do occur in the eastern focus area as well, but this trend also is not the distinctly NE trend of the lineaments. In fact the strikes of the rarest fracture sets in outcrop correspond to the greatest numbers of lineament orientations in the eastern focus area. Farther west Set I and Set II fractures strike closer to the lineament orientations, but the NE and NW-trending lineaments remain distinctly mis-oriented with respect to the general Set I and set II fracture trends. The NE lineament trends are similar to the trend of faults that affect basement, based on aeromagnetic anomalies. It may be that the NE-NW general lineament fabric is a result of fractures associated with fault systems combined with the effects of fracture Set III (J1) that strike nominally ENE.

Locally, fractures in outcrop coincide with lineament trends at the same buffered location, but the general NE-NW lineament fabric does not represent the Set I and set II fractures that arc across the project area.

Faults can be recognized in the strings of linked density highs in the filtered density ASTER and DEM data. Some of these strings coincide with fault systems that have been previously recognized or proposed. For example, the ENE-striking faults in the southern parts of the western and eastern focus areas are recognizable by ENE-trending strings of high density in the DEM filtered data. Other proposed fault systems that can be recognized in the strings of high density in the DEM filtered lineament data include the northerly (N and NNW) and easterly striking faults near the Finger Lake shores, and the NE-striking faults discussed above. However, a significant proportion of the proposed faults are not represented by sufficient lineaments to be recognized in the lineament data. Thus, the presence of a density high string can be used to demonstrate the probability of a fault in the region of the string, but the absence of a density high string does not necessarily mean that the area is free from faults.

The implications of the lineament analyses for potential CO_2 subsurface sequestration near the AES power plants can be summarized as the following: in each analysis of lineament data, it appears that most, or all, of the AES power plants in central NYS are close to a relatively high density of lineaments that might indicate fault systems. Furthermore, some power plants are near known faults or fault systems that are associated with lineaments (e.g., Hickling and Greenidge). Thus, it is necessary for any Phase II CO_2 subsurface sequestration research to include a 3D seismic survey in the region of proposed detailed study to determine the extent of the faulting.

TASK 6: FAULTS AND FRACTURES IN THE FOCUS AREAS, PART B

SUBTASK 6.4: LINEAMENTS FOR FOCUS AREAS FROM NEW FUSED LANDSAT AND ASTER IMAGES, SUBTASK 6.5: LINEAMENTS FOR FOCUS AREAS FROM A DEM, SUBTASK 6.6: GROUNDTRUTHING LINEAMENTS, AND SUBTASK 6.7: ESTIMATES OF FRACTURE CHARACTER NEAR THE AES POWER PLANTS BASED ON SUBTASKS 6.4, 6.5 AND 6.6

Robert Jacobi, Melissa Zelazny, Bea Csatho, University at Buffalo

INTRODUCTION

Task 6, Part B integrates Subtasks 6.4, 6.5, 6.6, and 6.7 (lineaments from remotely sensed data, lineaments from topography, groundtruthing, and implications from these two Subtasks for CO2 storage, respectively). The objective of Subtask 6.4 was to determine the best combination of new LandSat and ASTER images ('fused images") for lineament recognition, and then identify and map the lineaments from the fused image. The objective of Subtask 6.5 was to determine the best image of a digital elevation model (DEM) for lineament recognition, and then identify and map the lineaments from the DEM. The objective of Subtask 6.6 was to perform limited "groundtruthing" of the lineaments to verify that the lineaments represent structures. The objective of Subtask 6.7 was to use the compiled database of lineament and inferred structural information from Subtasks 6.4 to 6.6 to determine the possibility and character of faults and fractures near the AES power plants.

The overarching objective of this research was to identify and map lineaments in central New York State (NYS) to assist in characterizing the fabric of faults and fractures near potential sites for carbon dioxide (CO_2) subsurface sequestration. The present report was prepared by Jacobi. Much of this report is based on a M.S. thesis by Zelazny (Zelazny, 2011, Csatho and Jacobi were co-major thesis advisors); some sections are excerpted directly from the thesis. However, views in the Discussion and Conclusion sections are by Jacobi and do not reflect the Zelazny (2011) thesis.

The study area is located in the Finger Lakes region of Central NYS and covers eight counties (Figure 6.4,5&6-1). The counties are Yates, Steuben, Schuyler, Chemung, Cayuga, Tompkins, Chenango, and Broome (Figure 6.4,5&6-2). The study area encompasses five AES power plants that are prospective sites for the CO_2 capture and storage project. The power plants considered for potential CO_2 sequestration in the project are AES Cayuga, AES Greenidge, AES Hickling, AES Jennison, and AES Westover (Figure 6.4,5&6-3).

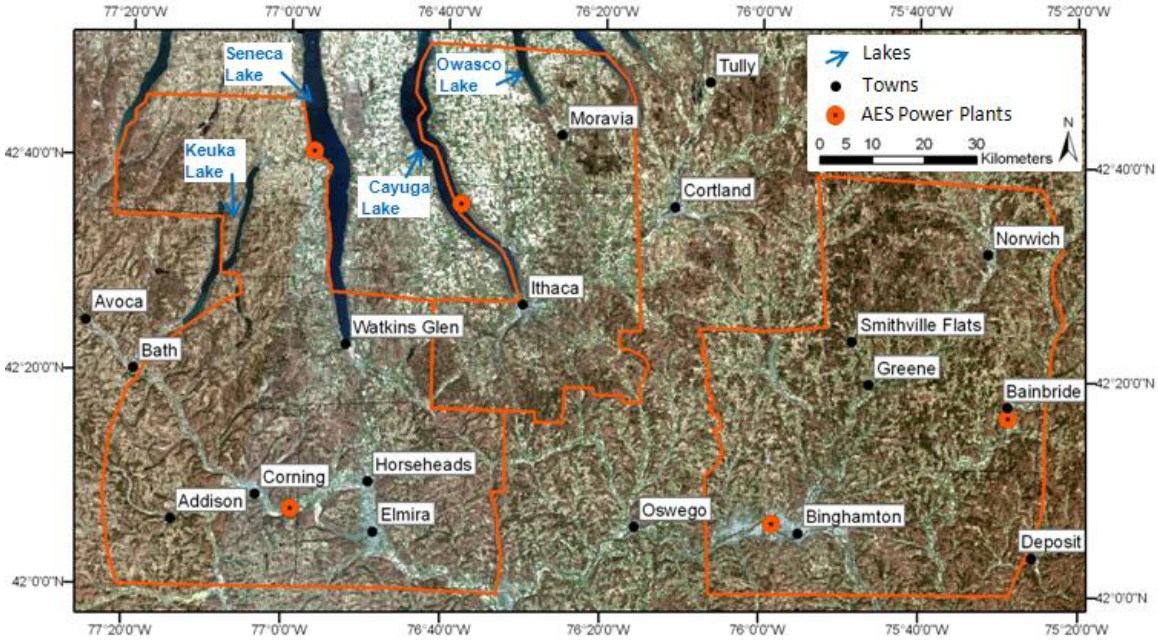

Figure 6.4,5&6-1. Site map with AES power plants, project boundary, town names and lake names. Base map is a Landsat ETM+ true-color composite mosaic, April, 2001. Figure from Zelazny et al. (2010) and Zelazny (2011).

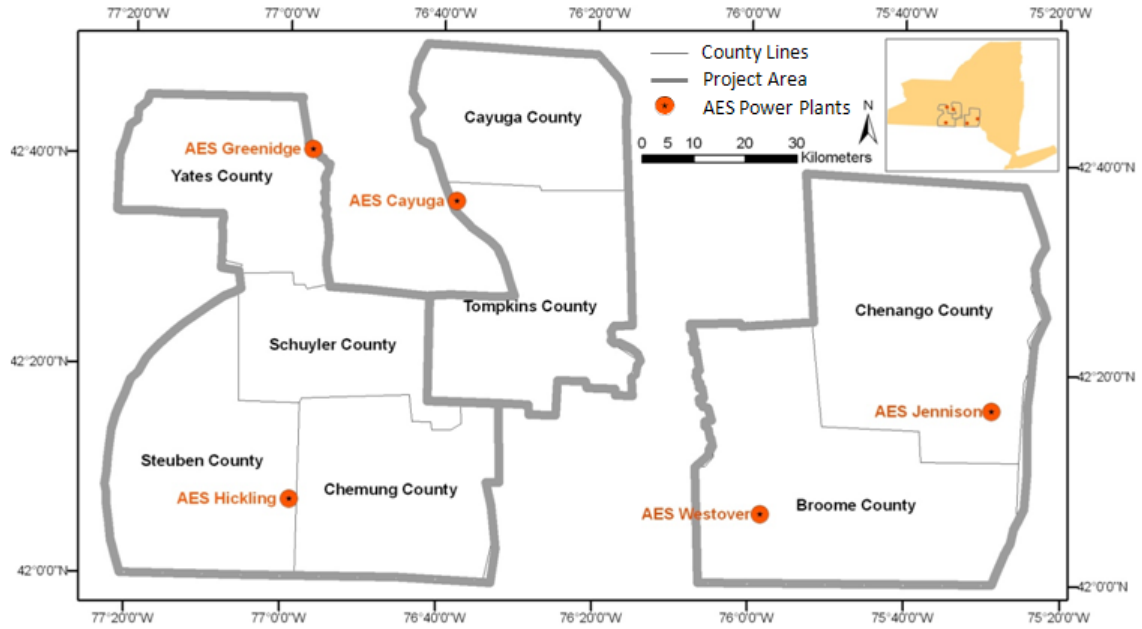

Figure 6.4,5&6-2. Site map with AES power plants, project boundaries, county lines and names with western, central and eastern focus areas included. Figure from Zelazny (2011).

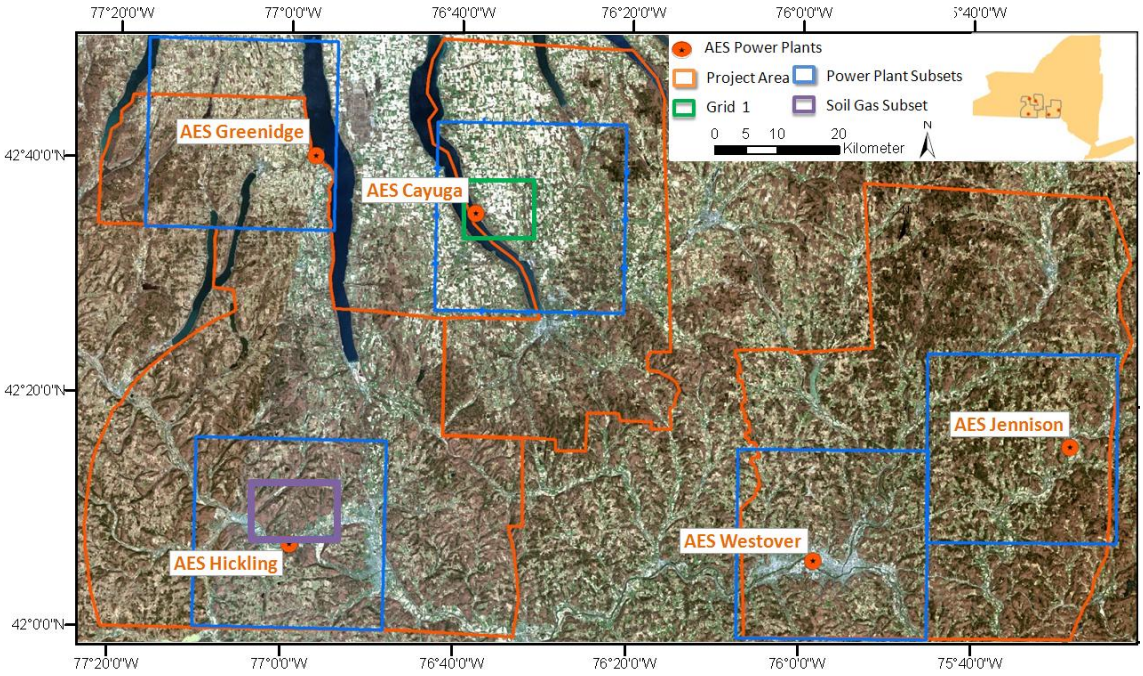

Figure 6.4,5&6-3. Site map with AES power plants, project boundaries, important subsets for detailed studies and Grid 1 for Phase 1 tests. Base map is a Landsat true-color composite. From Zelazny (2011).

Phase I of this project involved digitizing lineaments from 15 satellite images and DEM shaded relief representations in a 225 km^2 area surrounding the AES Cayuga Power plant ("Grid 1", Figure 6.4,5&6-3) to test which methodologies yield optimal results. Lineaments were digitized for the entire project area during Phase II. The project area was sub-divided into three subareas, western, central and eastern focus areas (Figure 6.4,5&6-2). The boundaries of these focus areas were used to separate analyses performed during Phase II. During Phase III a larger area around Grid 1 and the AES Cayuga power plant was chosen for a more detailed investigation; this region is labeled as the Cayuga Subset in Figure 6.4,5&6-3.

Stratigraphy

The Phanerozoic sedimentary sequence in the project area varies from ~6,000 ft (1800 m) thick in the north to about 12,000 ft (3600 m) in the south and is comprised primarily of Cambrian through Devonian interbedded shales, siltstones and sandstones with significant Cambrian-Ordovician, Silurian and middle Devonian carbonates (e.g., Van Broughton et al., 1966; Isachsen et al., 1991). All the units that outcrop in the project area are Devonian in age. The units in the project area outcrop in "belts" that trend approximately east-west and are younger in the southern part of the project area since the units dip south at 1° to 2° (Figure 6.4,5&6-4; e.g., Isachsen et al., 1991). The oldest unit in the project area is the Middle Devonian Hamilton Group (aqua color in Figure 6.4,5&6-4). This unit is mostly gray shale interbedded

with siltstones and sandstone, with rare thin limestones; this group includes the now well-known Marcellus black shale at the base of the sequence (e.g., Isachsen et al., 1991; Brett et al., 2007). The coarsening-up sequences from black shale to gray shale interbedded with sands and silts represent shallowing-up marine sequences in a shallow basin (e.g., Ettensohn and Barron, 1981). Although the basal black shale was formerly thought to mark the axis of the shallow basin (e.g., Ettensohn and Barron, 1981), the black shale has recently been proposed to have been deposited on the ramp of the western margin of the basin (e.g., Smith and Leone, 2011). The overlying Middle to Upper Devonian sequence is a textured lime green color in Figure 6.4,5&6-4 and consists the Tully Limestone overlain by the Genesee Group which is in turn overlain by the Sonyea Group. The Geneseo black shale marks the base of the Genesee Group (e.g., Smith and Jacobi, 2000). In western NYS the Middlesex black shale forms the base of the Sonyea Group, but in much of central NYS the coarser facies of interbedded turbiditic sands and shales of the Rock Stream Group characterize the entire Sonyea Group (Figure 6.4,5&6-4c). These sequences represent similar depositional environments as those in the underlying Hamilton Group (e.g., Ettensohn and Barron, 1981; Smith and Leone, 2011). The upper sequence in the project area is the Upper Devonian West Falls Group (light-yellow color in Figure 6.4,5&6-4). In western NYS the Rhinestreet black shale denotes the base of the West Falls Group, but in much of central NYS the coarser sands and shales dominate the basal section.

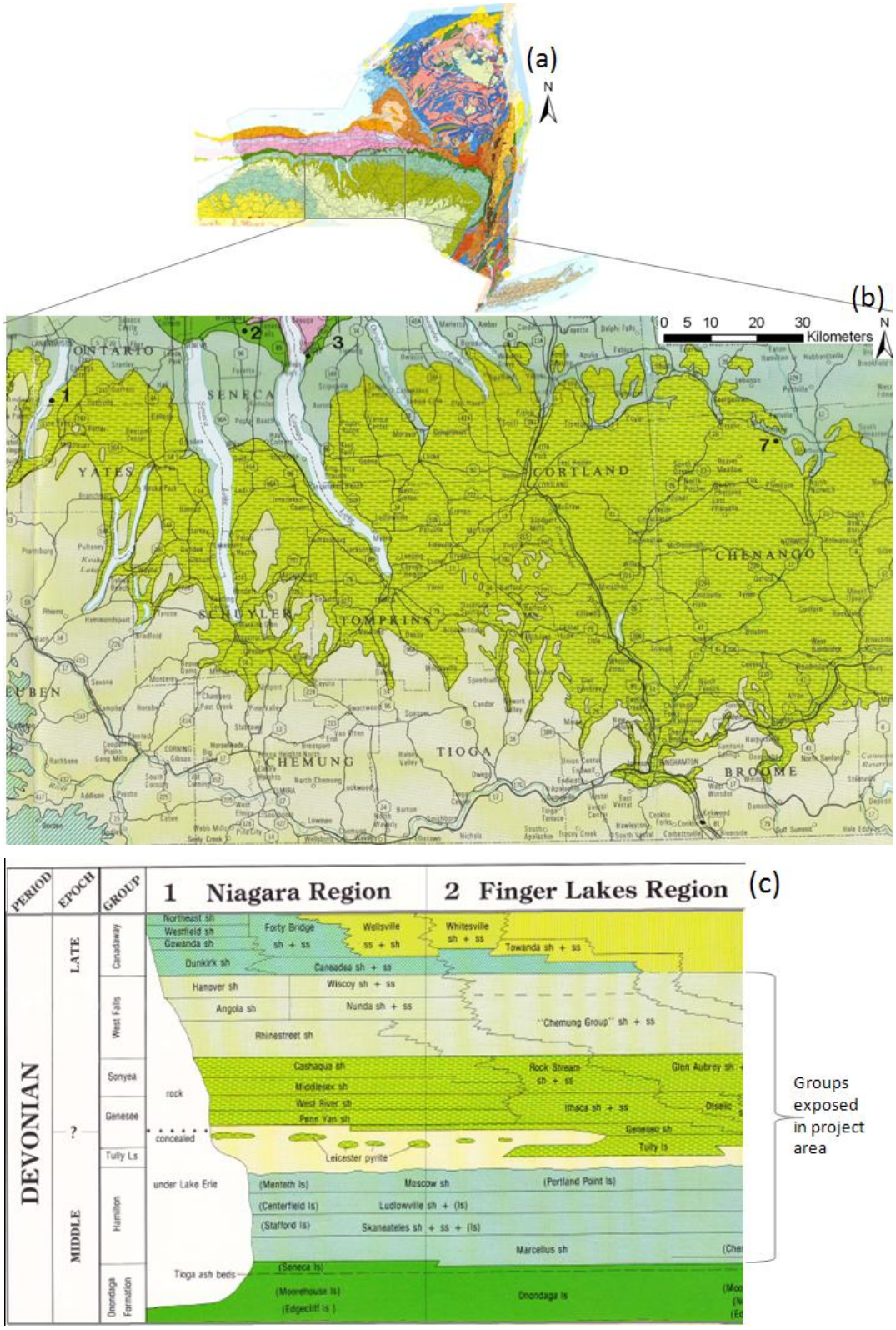

Figure 6.4,5&6-4. (a) Geologic map of New York State (b) Geologic map section of project area and (c) geological strata exposed in the project area (maps after Isachsen et al., 1991; figure from Zelazny (2011)

Alleghanian Orogeny and Related Fractures

The Alleghanian Orogeny occurred from 330 to 250 million years ago when the Gondwana (proto-Africa) continent collided with the east coast of Laurentia (proto-North America) (e.g., Hatcher, 2002). The Alleghanian Orogeny initiated with an oblique approach of proto-Africa (Gondwana), forming a peripheral bulge and subsequent erosion of most of the Mississippian and some Devonian sediments (Lash and Engelder, 2006). After this initial collision the principal stresses rotated clockwise as proto-Africa pivoted about a vertical axis and collided "head-on" with Laurentia (e.g., Hatcher, 2002; Engelder and Lash, 2008). Lash and Engelder (2006) proposed that this initial phase may have promoted northerly-striking fractures in the peripheral bulge region in western New York State (NYS); Engelder and Whitaker (2006) and Engelder and Lash (2008) proposed that consistently ENE-striking fractures (J1 or Set III fractures; e.g., Engelder and Geiser, 1980) across the entire northern Appalachian Basin resulted from the early Alleghanian phase as well. The later Alleghanian phase resulted in fractures that strike radially across the Appalachian Basin of NYS (NW to northerly-striking; called J2 or Set I or cross-strike or cross-fold set; e.g. Engelder and Geiser, 1980; Zhao and Jacobi, 1996; Figure: 6.4,5&6-5), and also resulted in NE to EW to WNW-striking fractures arcing (in plan view) across NYS (called SetII or strike parallel or fold parallel). Set I fractures were further subdivided into set Ia and Ib, based on orientation (Engelder and Geiser, 1980).

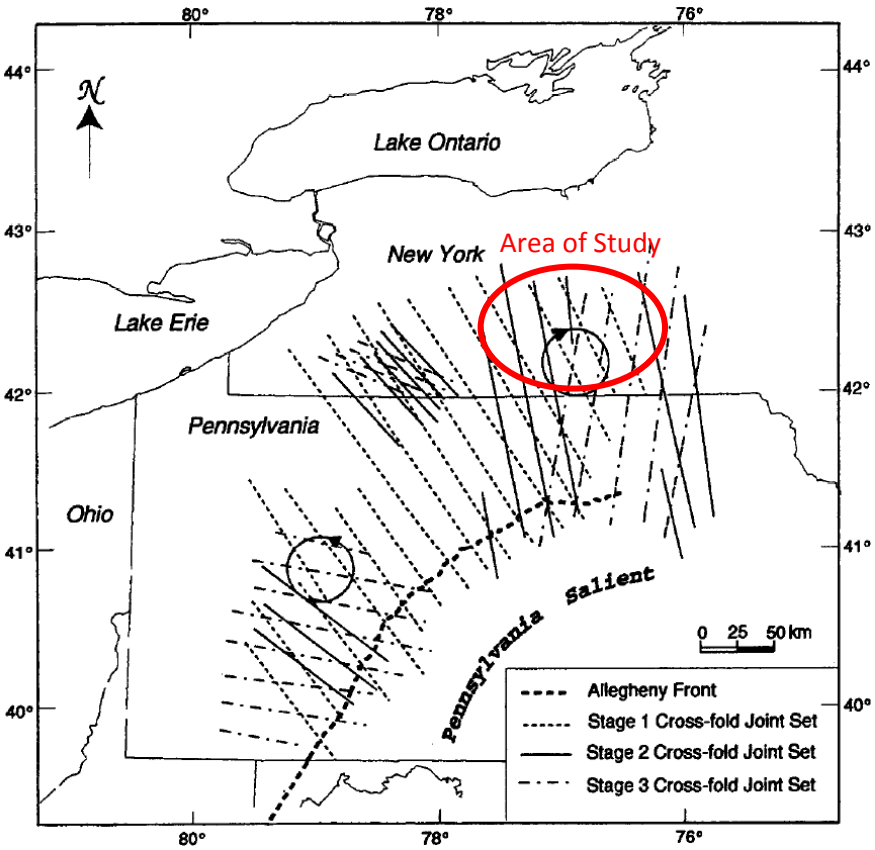

Figure 6.4,5&6-5. Cross-fold joint sets trajectories and rotation directions (indicated by circles with arrows) of the maximum compressive stresses during the Alleghanian Orogeny (after Zhao and Jacobi, 1996)

In the project area overall fracture sets Ia and Ib vary in orientation from 316° in the west to 17° in the east (Figure 6.4,5&6-6; Engelder and Geiser, 1980. The mean fracture strikes observed in the project area for Joint Set Ia and Joint Set Ib were 004° and 337° (West Falls Group), 001° and 342° (Sonyea Group), 005° and 340° (Genesee Group) (Engelder and Geiser, 1980). Fracture Set II varies in orientation from 112° in the west to 241° in the east with an arcuate pattern (Figure 6.4,5&6-6; Engelder and Geiser, 1979; 1980). Joint Set III is consistently oriented at about 060° in all outcrops (Engelder and Geiser, 1979; 1980). The angular difference between Set III and Set II increases toward the west with the largest difference apparent near the Steuben/Chemung County border. It is difficult to distinguish between Set III and Set II in the eastern section of the study area so eastern fractures with the same orientations were defaulted to Joint Set II.

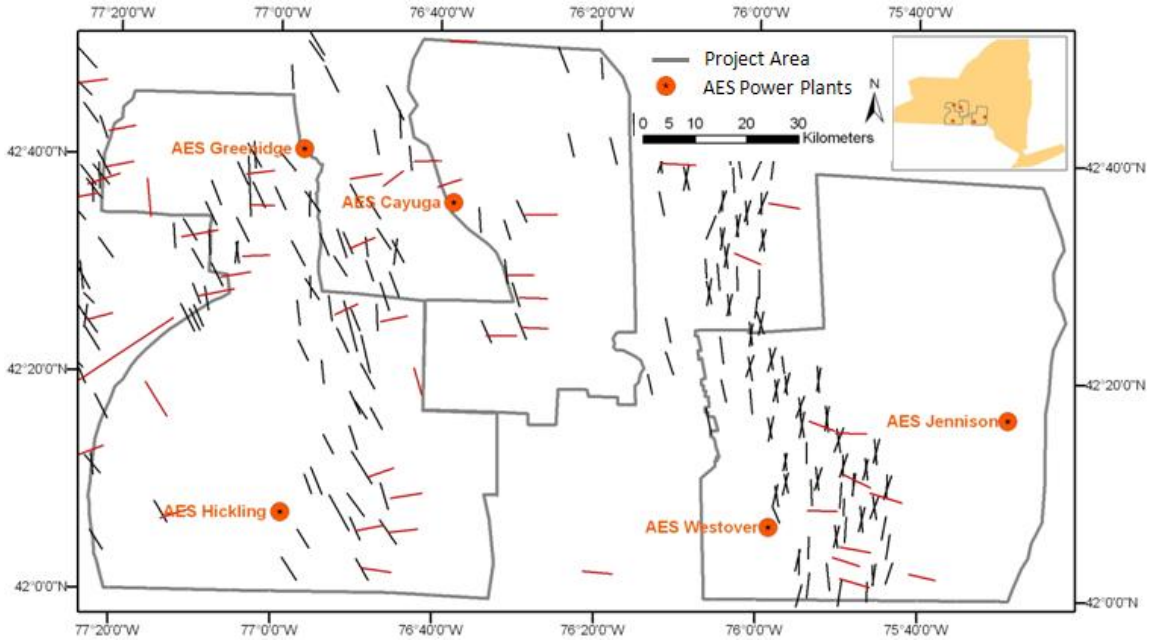

Figure 6.4,5&6-6. Set Ia and Ib (black) and Set II (red) joints mapped by Engelder and Geiser (1980) in the project area. Figure from Fisher et al. (2010) and Zelazny (2011).

In eastern NYS in primarily Chenango County fractures were measured in the field by Terech et al. (2005), Terech (2006), McGuire et al. (2006), McGuire (2007), and Jacobi (2007 b) (Figure 6.4,5&6-7). The following attributes were recorded for all fractures of each fracture set identified in each outcrop: the fracture spacing, strike, dip, apparent fracture length, apparent fracture height, fracture abutting relationship, fracture planarity, fracture decorations, lithology of fractured bed(s), and lithology thickness(es). Predominant fracture orientations mapped in the north are NNE (20° – 29°) and WNW (290° – 299°) (Terech et al., 2005; Terech, 2006; Jacobi, 2007) (Figure 6.4,5&6-8). The most abundant

fracture orientations for the more southerly region in the Chenango area are NNE (9° – 40°), WNW (282° – 304°) and NS (345° – 9°) (McGuire et al., 2006; McGuire, 2007; and Jacobi, 2007b) (Figure 6.4,5&6-9).

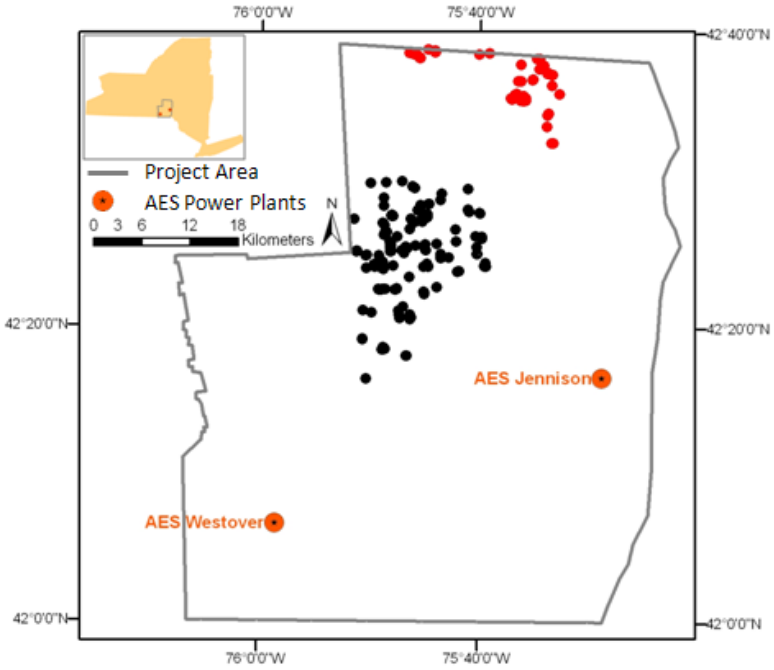

Figure 6.4,5&6-7. Outcrops where fracture data were collected by Terech et al. (2005), Terech (2006), and Jacobi (2007) (red circles) and by McGuire et al. (2006), McGuire (2007), and Jacobi (2007b) (black circles). Figure from Zelazny (2011).

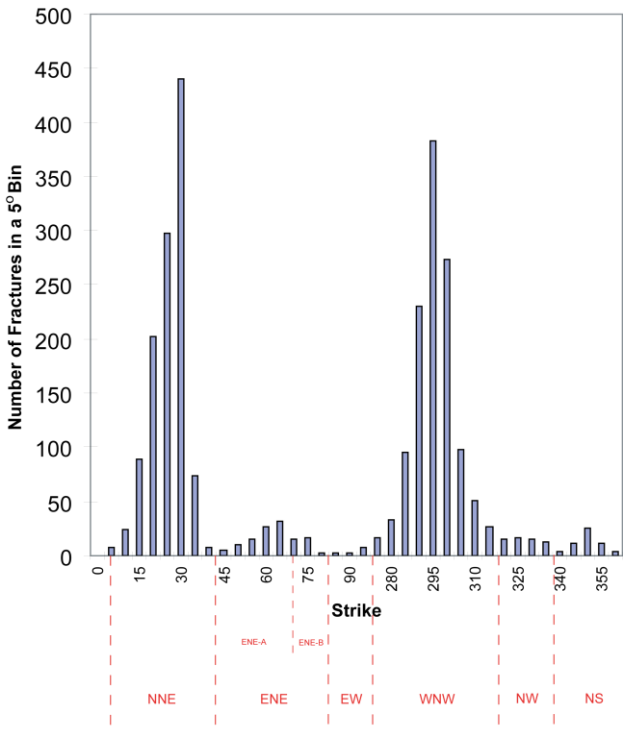

Figure 6.4,5&6-8. Fracture distribution in the northern study area of the Chenango County region and orientation boundaries of the fracture sets. Figure after Terech et al. (2005) and Terech (2006), from Jacobi (2007b).

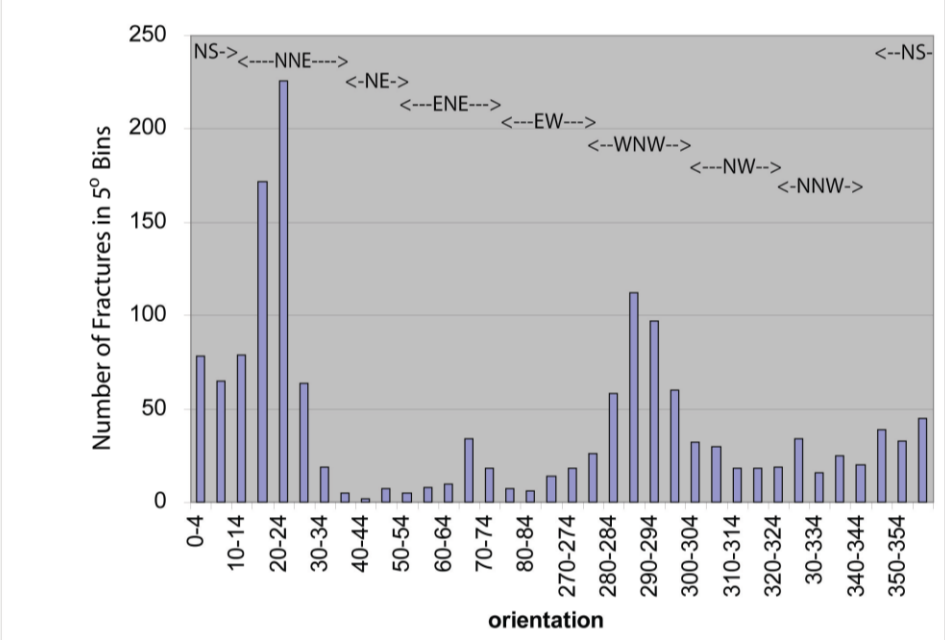

Figure 6.4,5&6-9. Fracture distribution in the southern study area of the Chenango County region and orientation boundaries of the fracture sets. Figure after McGuire et al. (2006), McGuire (2007), and from Jacobi (2007b).

Fracture Intensification Domains (FIDs)

Fracture Intensification Domains (FIDs) exhibit relatively closed spaced fractures and are relatively narrow zones across strike, and long parallel to strike. The fracture spacing is generally greater than 4 fractures/m; the width of the zone is less than 0.5 km and commonly much narrower (on the order of 50 meters or even less), and the length can be greater than 0.5 km (e.g., Jacobi and Zhao, 1996b; Jacobi, 2002; Jacobi et al, 2002). Although many FIDs are defined by the locally master fracture set, the fracture set defining the FID is not necessarily the regional, or even local, master set (e.g., Jacobi, 2007a, b). FIDs in many cases have been shown to be associated with fault systems observed in the field, imaged in seismic reflection profiles, inferred from stratigraphic offsets and from anomalous soil gas contents (e.g., Jacobi and Fountain, 2002). Many FIDs are coincident with lineaments of the same trend, and these lineaments are typically longer than 0.5 km. (Jacobi, 2002). In the Chenango County region of eastern NYS (in the eastern focus area), FIDs commonly are coincident with topographic lineaments identified in DEMs (Figures 6.4,5&6-10 and 6.4,5&6-11; e.g., Terech, 2006; McGuire, 2007; Jacobi, 2007). In the western focus area, fractures and FIDs were also found to coincide with lineaments (see discussion below; e.g., Drechsel et al., 2004; Cruz et al., 2005; Cruz, 2005; Jacobi, 2007a).

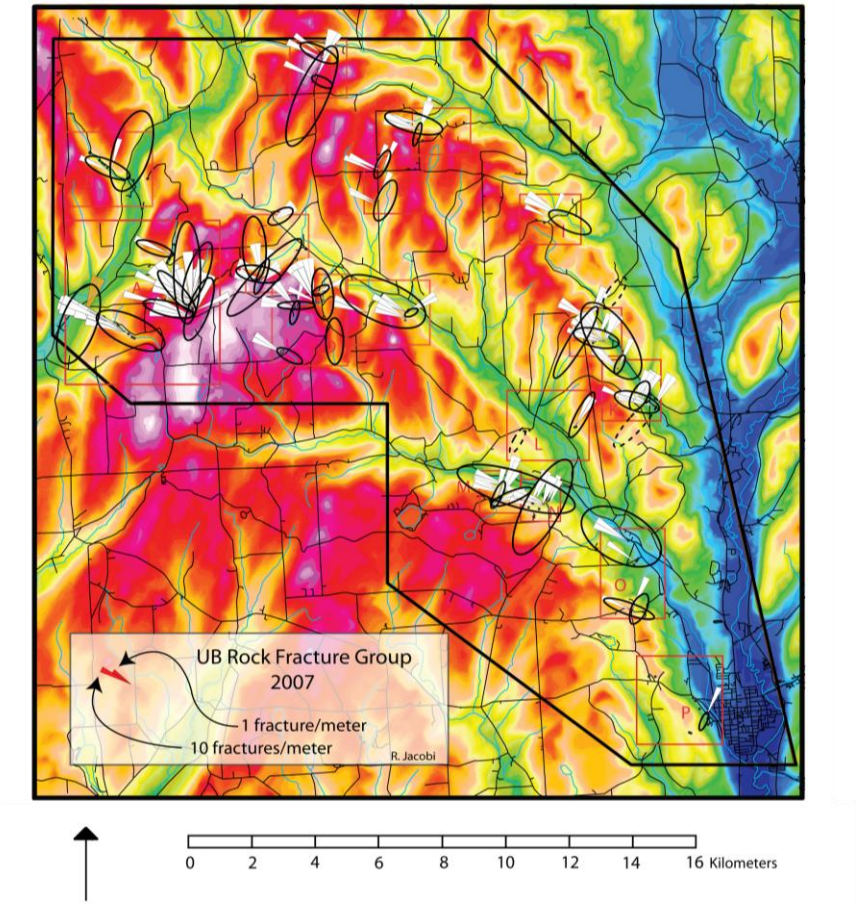

Figure 6.4,5&6-10. Spatial correspondence between fracture intensification domains (FIDs) and nearby topographic features in the northern study area of the Chenango County region (see Figure 6.4,5&6-7 for location of sites in project area). Ellipses indicate a coincidence between the location and trend of a topographic feature (generally a valley) and an FID, defined here as more than 4 fractures/meter. Note that all the major valleys have nearby sites with FIDs that trend collinearly with the valley. Figure from Jacobi (2007b).

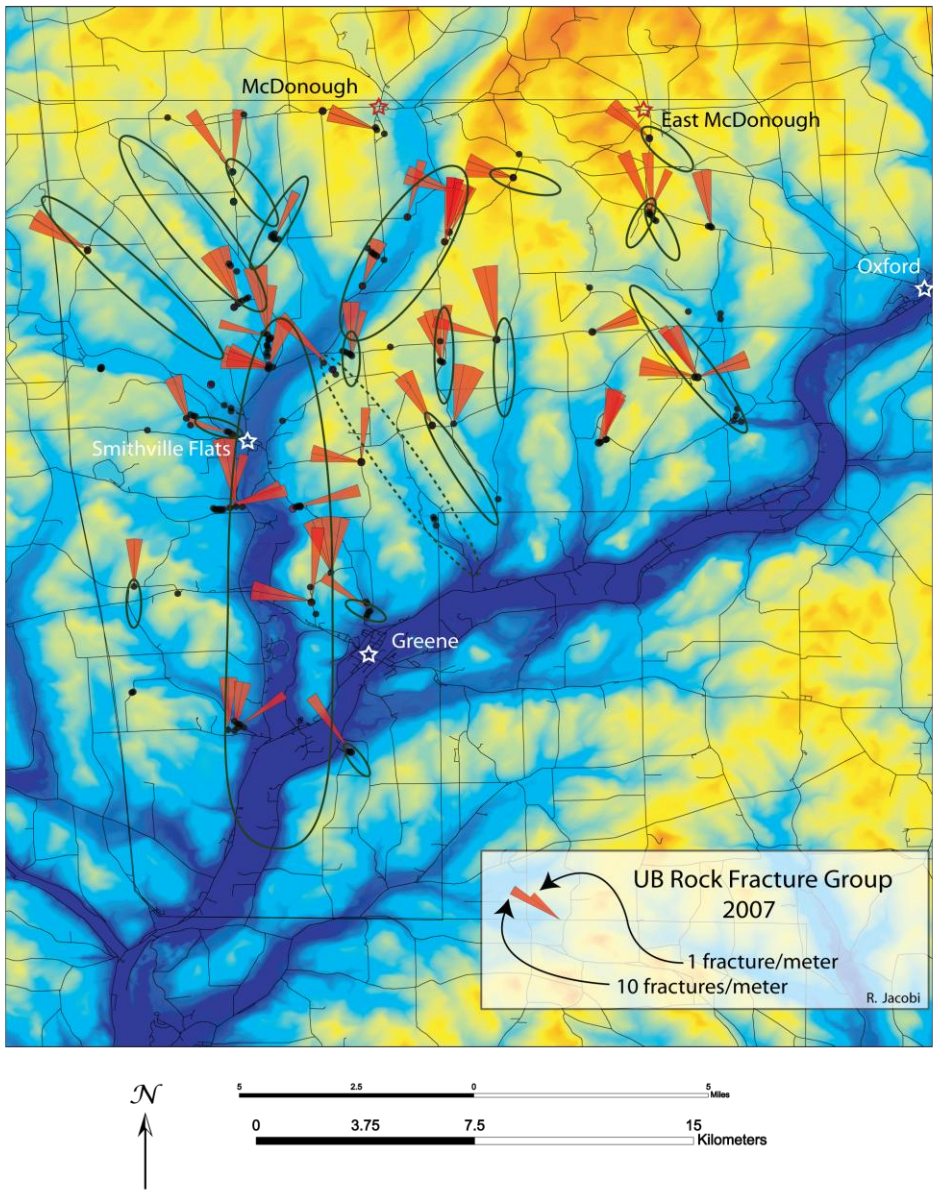

Figure 6.4,5&6-11. Spatial correspondence between fracture intensification domains (FIDs) and nearby topographic features in the southern study area of the Chenango County region. Ellipses indicate a coincidence between the location and trend of a topographic feature (generally valley) and an FID. Note that all the major valleys have sites nearby with FIDs that trend collinearly with the valley. Figure from Jacobi (2007b).

Fault Systems

Bradley et al. (1941). Bradley et al. (1941) mapped faults from bedrock exposures at streambeds, road cuts and quarries across Yates and Steuben counties in the western focus area. The faults were nearly vertical normal faults and high-angle thrust faults with trends of northeast, north-northwest, east-west and

north-south (Figure 6. 2-12). Bradley et al. (1941) also mapped micro-faults and folds in shale units which were interpreted as zones of syn-depositional deformation and display both brittle and ductile deformation (Figure 6.4,5&6-12).

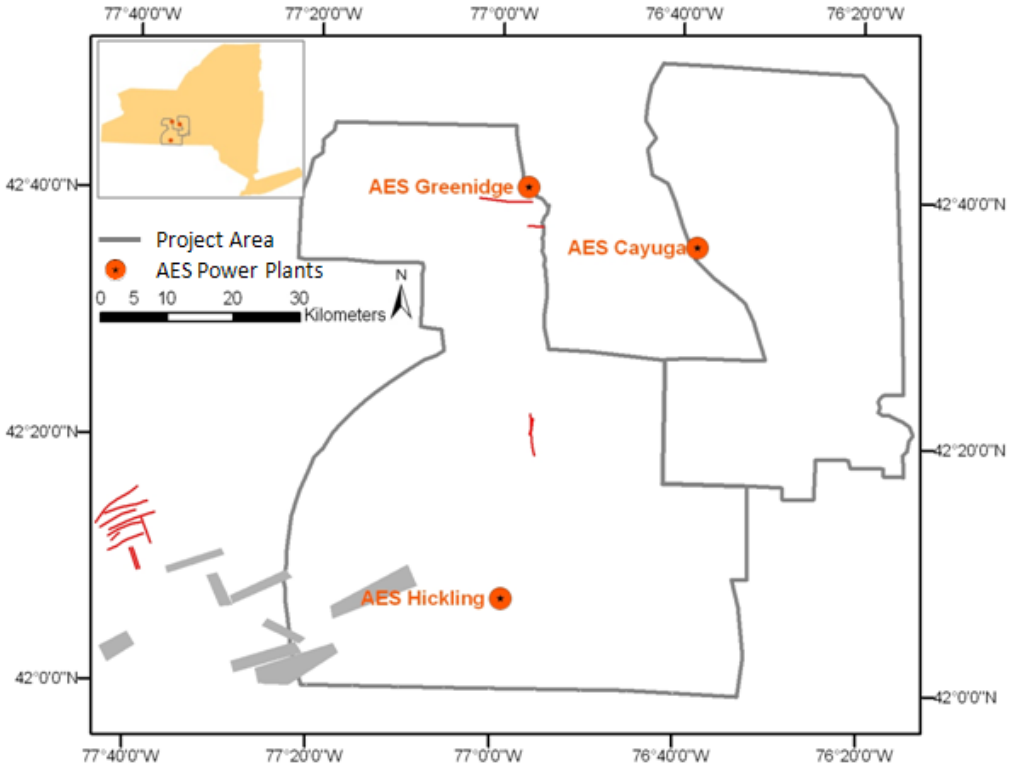

Figure 6.4,5&6-12. Faults (red) and fault zones (gray) mapped by mapped by Bradley et al. (1941). Figure from Fisher et al. (2010) and Zelazny (2011).

Isachsen and McKendree (1977). Isachsen and McKendree (1977) transcribed fault information from the 1971 New York State Geologic Map with additional details added from the general literature (e.g., published theses, maps, reports and field notes from 1971 to 1977). Some details on the map include dip of fault planes, separation, location and width of breccias. Isachsen and McKendree (1977) also identified linear features from Landsat Earth Resource Technology Satellite (ERTS) multispectral bands 5 and 7 images at a scale of 1:500,000 and 1:250,000. (Dated from 1972 to 1974, and with 70 to 80 meter resolution). Isachsen and McKendree's (1977) faults and lineations are shown in Figure 6.4,5&6-13.

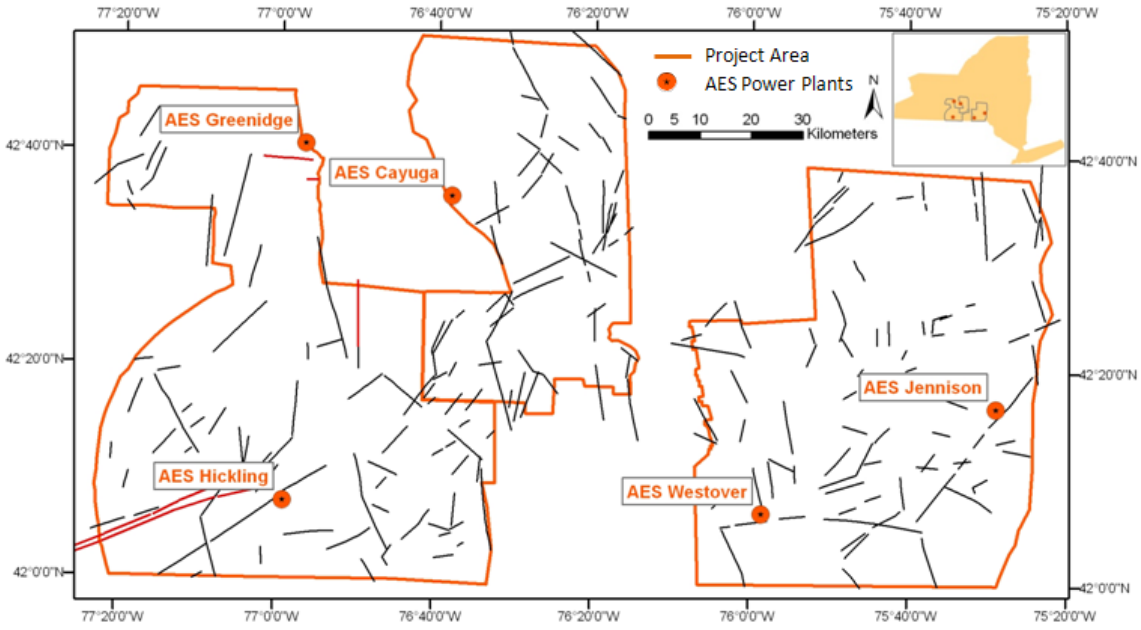

Figure 6.4,5&6-13. Linear features (black) and faults (red) compiled from previous geologic maps and Landsat imagery (Isachsen and McKendree, 1977). Figure from Fisher et al. (2010) and Zelazny (2011).

Murphy (1981). Murphy (1981) inferred faults primarily from well logs and Landsat lineaments as part of the National Waste Terminal Storage Program (Figure 6.4,5&6-14). Abrupt changes in unit thickness and depth between adjacent wells were interpreted as indicating the presence of a fault between the wells. Thrust faults were indicated in well logs with over-thickened sections and/or repetition of formation horizons.

Murphy (1981) proposed two right-lateral strike slip fault zones; one extends from Himrod, NY near the Greenidge power plant toward Pennsylvania along the western shore of Seneca Lake (Figure 6.4,5&6-14). The second fault is an echelon right-lateral strike-slip tear fault of the Cayuga Creek Valley that extends from west of Ithaca southward toward Pennsylvania (Figure 6.4,5&6-14). This study also proposed a 25 km long oblique-slip fault (normal fault with some right-lateral motion) near Keuka Lake.

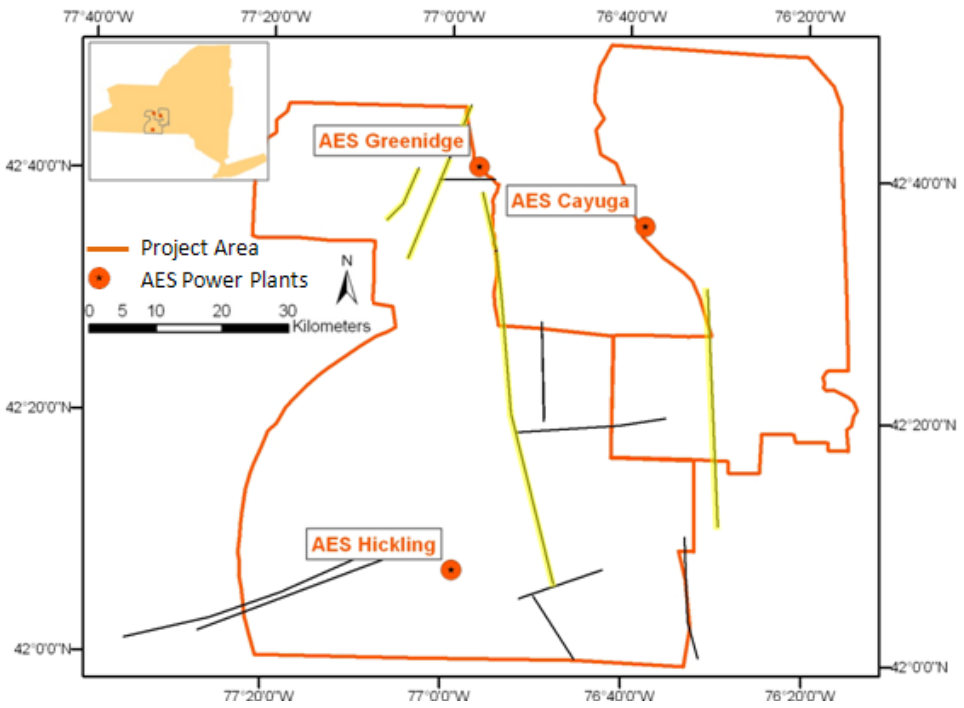

Figure 6.4,5&6-14. Map of south-central NY and the western and central focus areas with Murphy's (1981) proposed faults. Faults in yellow are discussed in text. Figure from Fisher et al. (2010) and Zelazny (2011).

Jacobi (2002), Jacobi (2007a, b), Jacobi (2010); Jacobi (2011a, b). Beginning in 2002, Jacobi (2002) has followed a nine-year program integrating field studies with subsurface data to determine the general distribution of faults in NYS. For the 2002 study, Jacobi (2002) identified lineament bundles in the EarthSat (1997) lineament data; these lineament bundles were based on density and continuity of the EarthSat (1997) lineaments. Where the UB Rock Fracture Group had data, these bundles showed a spatial relationship to FIDs, faults observed in outcrop, soil gas anomalies, faults observed in a limited number of seismic reflection profiles, inferred from well logs, aeromagnetic and gravity anomaly trends. Jacobi therefore suggested that the bundles represented fault systems (Figure 6.4,5&6-15). A number of research projects since that time have continued to confirm the general view that the Appalachian Basin of NYS is cut by hundreds of reactivated faults, and has refined the locations and movement histories of the faults (e.g., Jacobi 2007; Jacobi et al., 2011a, b.)

The faults described by Jacobi (2007a) were mapped as part of a Department of Energy (DOE) and New York State Energy Research and Development Authority (NYSERDA) project to gain a better understanding of the Ordovician Trenton/Black River and its natural gas potential in the Appalachian Basin of NYS. Jacobi (2007a) combined traditional and innovative techniques to determine fault locations in the central and western focus areas of this project. Jacobi (and Fountain and students) utilized multiple datasets that included detailed fracture analyses, soil gas, 2D seismic reflection, outcrop stratigraphy, well logs,

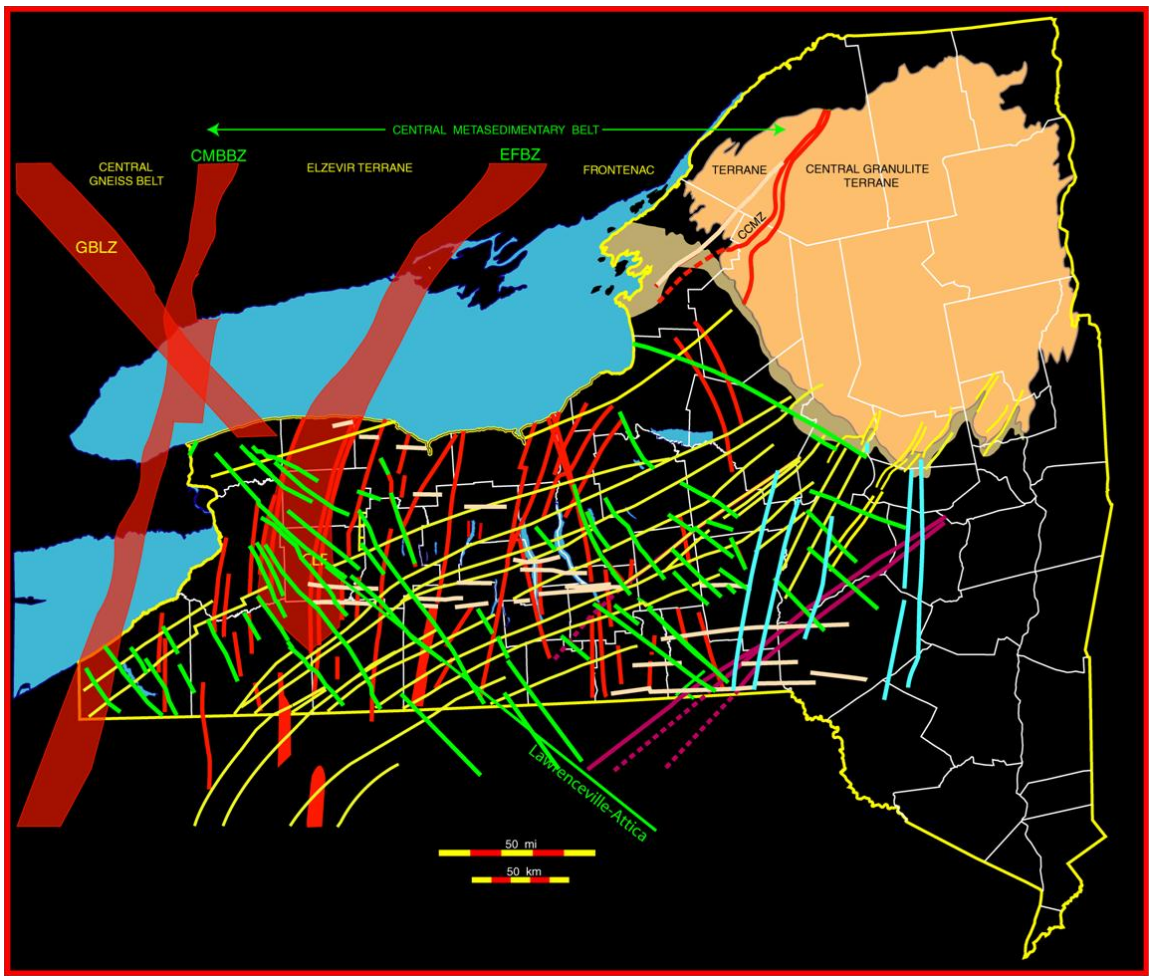

Figure 6.4,5&6-15. Map of selected faults in the Appalachian basin of New York State. Colors indicate different sets of faults in terms of orientations and motion histories. From Jacobi (2002).

horizontal oriented core, and aeromagnetic and gravity anomalies. The main fault trends identified by Jacobi and Fountain (2007) were ENE and EW with northerly-striking cross faults, all of which had been reactivated numerous times (Figure 6.4,5&6-16).

The focus of Jacobi (2010) was the arcuate (in map view) fault set across the Appalachian basin of NYS. These faults, imaged in both 2D and 3D seismic reflection data began as Iapetan opening faults and were reactivated during each successive orogeny. Jacobi (2011a, b) summarized the advances in the understanding of the fault systems based on extensive 3D seismic data in eastern NYS (in the eastern focus area of the project) and in western NYS, combined with 2D seismic elsewhere and surface studies now across central and western NYS.

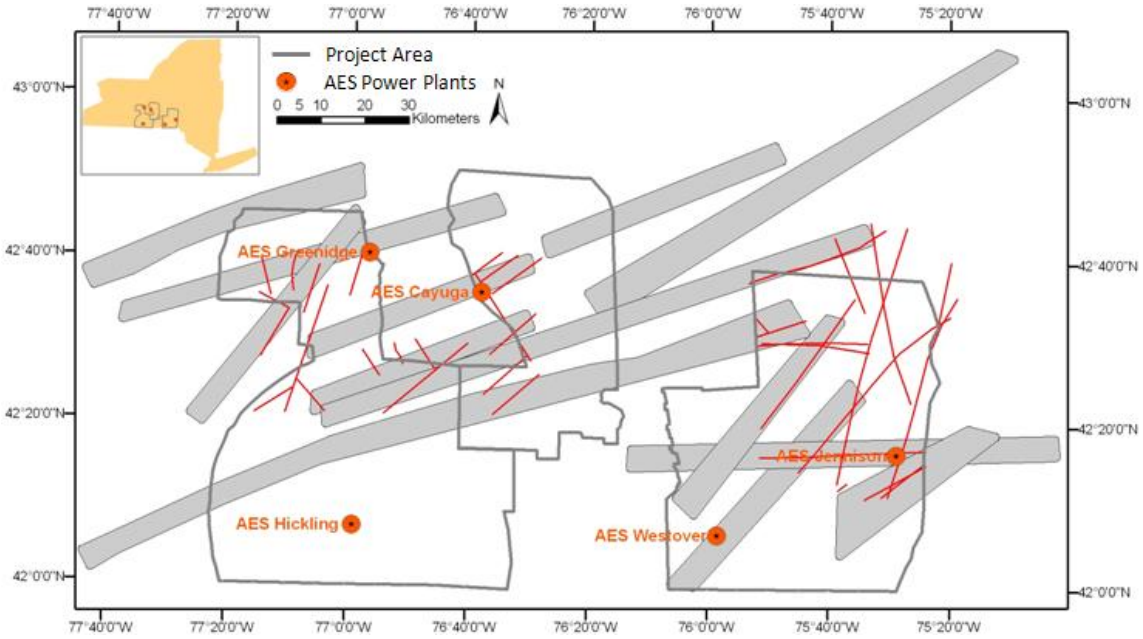

Figure 6.4,5&6-16. Map of fault zones (in gray) that Jacobi (2002) inferred from EarthSat (1997) lineaments and selected faults (in red) from Jacobi (2007a). Figure from Fisher et al. (2010) and Zelazny (2011).

Lineament Mapping.

Lineaments are surface expressions of structural features on the surface as geomorphological features. Lineaments previously identified in the project area have been related to the structural geology of the region (e.g., EarthSat, 1997; Jacobi, 2002; Everett et al., 2003; Cruz et al., 2005). Jacobi (2002) suggested that faults that were previously overlooked due to their subtle properties can be mapped by identifying and groundtruthing lineaments. Lineaments longer than 0.5 km regularly relate to fracture intensification domains (FIDs) and shorter lineaments around 100 m are found to be parallel to fractures (Jacobi et al., 2002). Lineament identification and digitizing projects in NYS that intersect the present project area include Isachsen and McKendree (1977), EarthSat (1997), Everett, et al. (2003), Everett et al. (2004), Drechsel et al. (2004), Cruz et al. (2005), and Cruz (2005). Previously identified lineament trends in NYS include NS, NW, EW, and an arcuate NE (western NYS) to ENE-striking (central and eastern NYS) (Jacobi, 2002, 2010).

Isachsen and McKendree (1977). Linear features were mapped by Isachsen and McKendree (1977) using multiple sources to compile and create the preliminary brittle structure map of New York State. Lineaments were defined and identified as "any relatively sharp, straight, alignment of drainage, topography, or tonal contrast which may be of natural origin" (Isachsen and McKendree, 1977). Isachsen and McKendree (1977) identified linear features from Landsat Earth Resource Technology Satellite (ERTS) multispectral bands 5 and 7 images at a scale of 1:500,000 and 1:250,000 (dated from 1972 to 1974, and with 70 to 80 meter resolution).

EarthSat (1997), Everett et al. (2003), Everett et al. (2004). The 1997 EarthSat project created digital lineaments for fracture analysis to assess potential fractured reservoirs for hydrocarbon production in NYS (EarthSat, 1997). Ten Landsat Thematic Mapper (TM) images acquired from 1984 to 1986 were mosaiced to cover most of NYS and displayed with a band-weighted combination R(7) G(4) B(2) using proprietary principal component analysis and other tools. The mosaic was divided into four image maps at a scale of 1:250,000. Lineaments were digitized on these four images by mapping lithologic boundaries, structure and unusual or anomalous vegetation patterns (Figure 6.4,5&6-17).

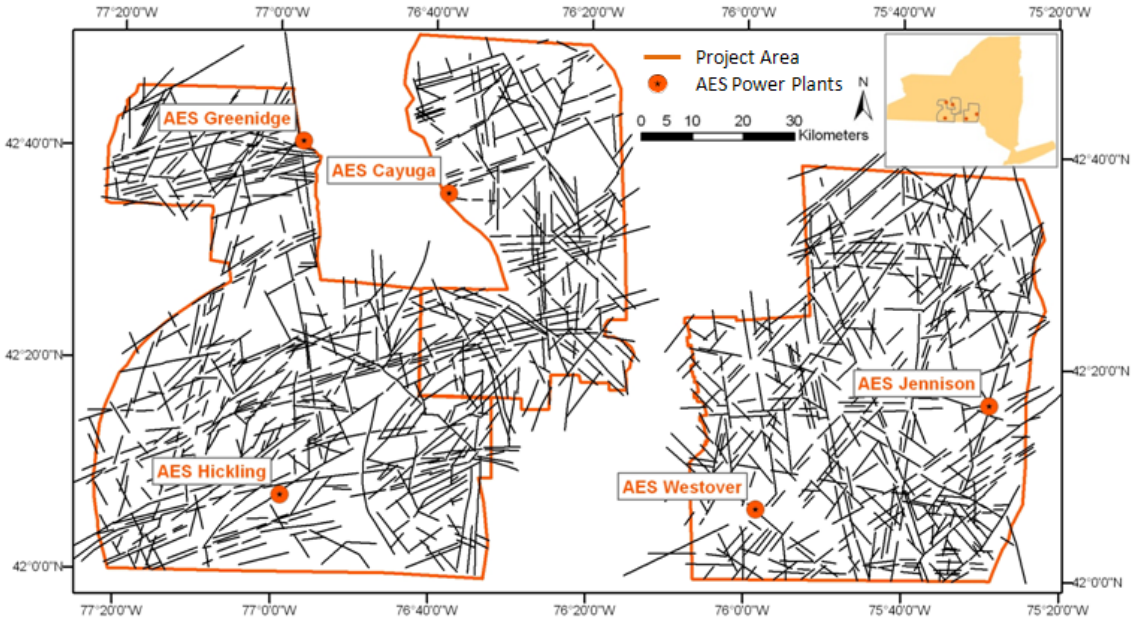

Figure 6.4,5&6-17. Lineaments mapped by EarthSat (1997) from Landsat TM imagery in the present project area. Figure from Zelazny (2011).

The Landsat mosaic was also used to digitize regional tectonic features such as basins, basin boundaries, uplifts, and major fault/fracture zones at a scale of 1:500,000. The mean lineament trend of the 2,869 lineaments in the Finger Lakes region is 60°. Everett et al. (2003, 2004) reinterpreted new Landsat and ASTER images in light of better imaging techniques and geological control.

Drechsel et al. (2004), Cruz et al. (2005), and Cruz (2005). The objective of this project was to investigate optimal image enhancements for lineament mapping and test these lineaments against known structure data in the same area. Cruz (2005) applied a Principal Component Analysis for fusing Landsat and Advanced Spaceborne Thermal Emission and Reflection Radiometer (ASTER) satellite imagery to enhance linear features. Cruz (2005) found the fused ASTER/Landsat composite optimal for identifying lineaments that relate to strike parallel fractures (ENE trending and EW trending) and PC ASTER image optimal for identifying lineaments related to cross strike fractures (NW trending and NNW trending). Lineaments were identified at various scales that include 1:200,000, 1:50,000 and 1:25,000; these lineaments where then merged into a single file (Figure 6.4,5&6-18). The study area in Cruz (2005) was located primarily in the region between Cayuga and Seneca Lakes - mostly outside the project area - but a slight overlap in the western focus area of the present project allowed for some comparison of lineaments.

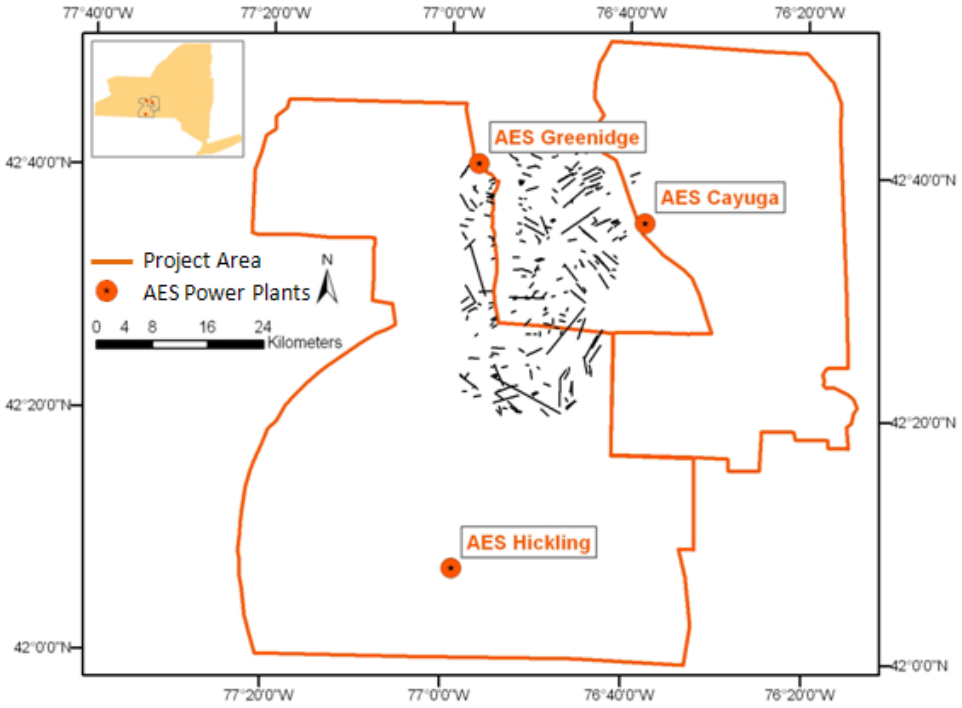

Figure 6.4,5&6-18. Lineaments mapped from ASTER PCA as a color composite R(PC2), G(PC1), B(PC4) by Drechsel et al. (2004), Cruz et al. (2005), and Cruz (2005). Figure from Zelazny (2011).

Other Lineament Studies. Other lineament studies were conducted by various UB Rock Fracture Group students as part of their detailed fracture studies in specific areas that are located within the present project area: Terech's (2006) and Jacobi's (2007) topographic lineament study in the northern most part of the eastern focus area, McGuire's (2007) and Jacobi's (2007) topographic and airphoto study in the central part of the eastern focus area; and Stroup et al's (2006) and Jacobi's (2011c) topographic lineament study in the northern part of the central focus area. In all cases the studies found that the fabric of the lineaments can be related to the fabric of the fractures and faults, but that the lineaments in many cases do not provide a one-to-one "road-map" of the fractures and faults. In general, more individual fractures and faults, and even trends, occur than are indicated by the lineaments.

DATA

Most of the data used in this project were acquired using remote sensing tools. The main data sets were Landsat and Advanced Spaceborne Thermal Emission and Reflection Radiometer (ASTER) satellite images, and Digital Elevation Models (DEM) obtained from USGS and National Aeronautics and Space Administration (NASA) websites. Auxiliary data sets used as GIS layers include streams, roads, railroads, and digitized drumlin outlines.

Landsat Imagery (Subtask 6.4)

Landsat images are easily accessible and frequently used for lineament identification (e.g., Rahiman and Pettinga, 2008). Landsat Enhanced Thematic Mapper Plus (ETM+) imagery is obtained from a sensor that orbits the Earth at a height of 705 km on a sun-synchronous orbit (Jensen, 2005). The sun-synchronous orbit aids in identifying structural features because a specific location on an image will have the same sun illumination angle on multiple images. Moreover, sun-synchronous satellites pass over any given latitude at almost the same local time during each orbital pass, resulting in roughly the same illumination angle at neighboring images, making them ideal for generating image mosaics. Landsat ETM+ multispectral imagery consists of six 28.5 meter resolution spectral bands in the Visible and Near Infrared (VNIR) and Shortwave Infrared (SWIR) domains (wavelengths: 0.45µm to 2.35µm), as well as one 15 meter resolution panchromatic visible band and one thermal band (Jensen, 2005). The size of a Landsat scene is 185 km by 185 km, covering 31,450 km^2. Because the multispectral visible bands of Landsat imagery have lower spatial resolution than that of ASTER (28.5 m vs. 15 m), Landsat data were only used in the experimental stages (Phase I) for Grid 1, which is a small 225 km^2 area around the AES Cayuga power plant (Figure 6.4,5&6-3).

Landsat images were obtained free of charge from the Earth Resources Observation and Science (EROS) Center of USGS by using the Global Visualization viewer (http://glovis.usgs.gov/). The images captured by the Landsat sensors are identified with their path (longitudinal) and row (latitudinal) designations in a

Worldwide Reference System (WRS). Four Landsat scenes were needed to cover the project area with the following paths: 15 & 16, and rows: 30 & 31 (Figure 6.4,5&6-19).

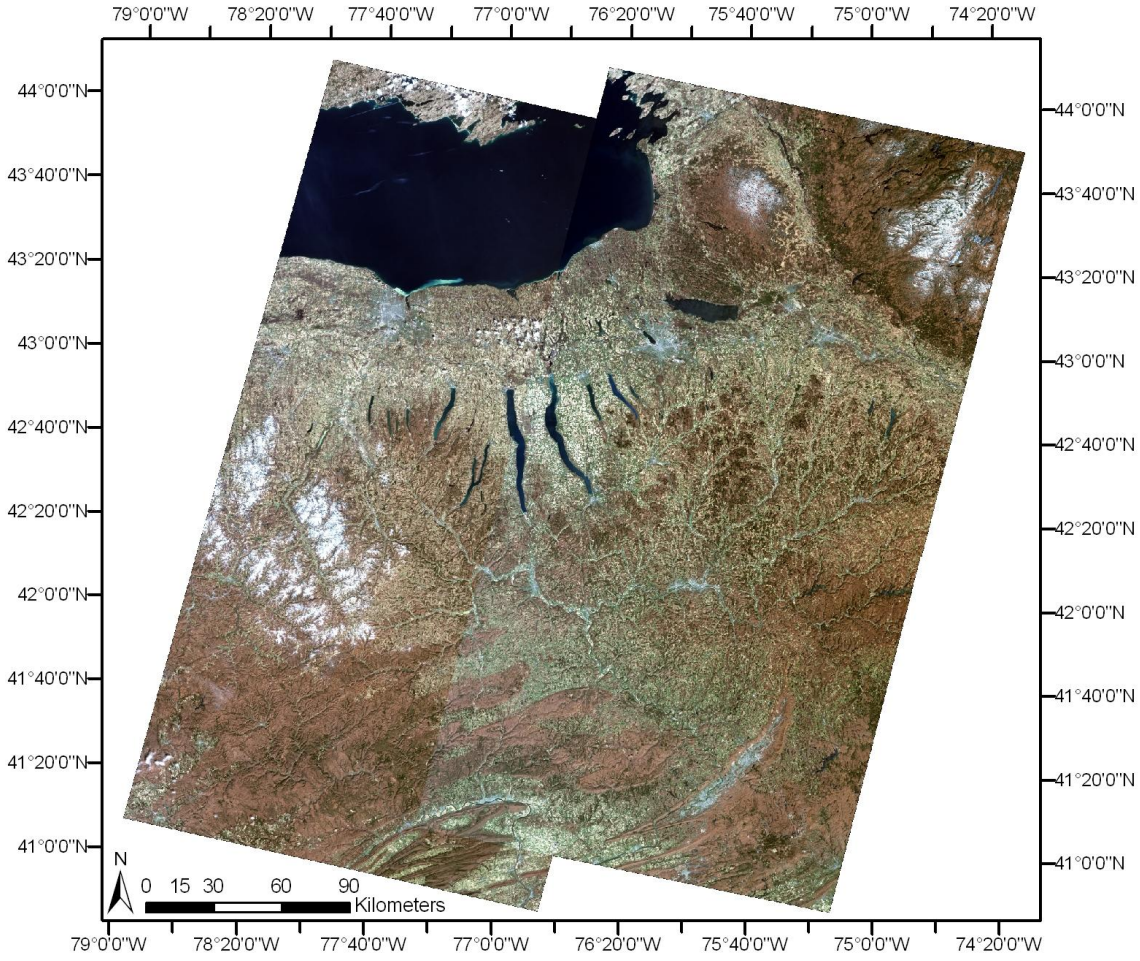

Figure 6.4,5&6-19. Landsat imagery – true-color composite R(3) B(2) G(1) covering the project area with four scenes. Figure from Zelazny et al. (2010) and Zelazny (2011).

The Landsat satellite passes over the same location on the Earth every 16 days, resulting in a temporal resolution of 16 days. Various acquisition times throughout the seasons provide images with different snow cover, tree canopy coverage and soil moisture content providing a robust and diversified dataset for lineament identification. Image selection was based on the following criteria:

(1) time of year, preferably leaf-off canopy conditions and no snow in early spring or late fall;

(2) cloud cover (less than 30%);

(3) the ability to use the image as part of a mosaic (the availability of other cloud-free images, preferably from the same year/season).

Based on the above criteria a total of 12 Landsat 7 ETM+ images were selected with dates of April 28th 2001, June 15th 2001 and October 16th 1999 that covered Grid 1. The images for the final mosaic were dated April 19th 2001 and April 28th 2001 that covered the project area. The georeferenced Landsat images were downloaded in GeoTIFF image format.

ASTER Imagery (Subtask 6.4)

Advanced Spaceborne Thermal Emission and Reflection Radiometer (ASTER) imagery is a rich source of geologic information because of its good spectral resolution in the short-wave infrared domain (Jensen, 2005). The ASTER mission started in 2000; its sensor captures high spatial resolution images with a scene size of 60 km by 60 km and 14 spectral bands, ranging from visible to thermal wavelengths (Jensen, 2005). The temporal resolution of the ASTER images is 16 days with a sun-synchronous polar orbit. Images obtained by the Visible and Near-Infrared Radiometer (VNIR) and Shortwave Infrared Radiometer (SWIR) in band-1 to band-9 with wavelengths ranging from 0.52 µm to 2.430 µm were used for this study. The VNIR bands have a resolution of 15 m and the SWIR bands have a resolution of 30 m.

All ASTER Images were obtained from NASA's Earth Observing System (EOS) Clearinghouse (ECHO) Warehouse Inventory Search Tool (WIST) website (http://wist.echo.nasa.gov). Eleven ASTER images were required to cover the project area; these images were selected to provide seamless transitions and proved suitable for a mosaic (Figure 6.4,5&6-20). Image selection was based on the same criteria as for Landsat imagery:

(1) time of year, preferably leaf-off canopy conditions in early spring or late fall;

(2) cloud cover (less than 30%);

(3) the ability to use the image as part of a mosaic (the availability of other cloud-free images, preferably from the same year/season).

Based on the criteria above, 11 September images from a four-year time period were selected. These images, used for the final mosaic shown in Figure 6.4,5&6-20, were dated September 3rd 2001, September 6th 2002, September 20th 2004, September 5th 2005 and September 14th 2005. Downloaded images were Level L1A and were processed as validated images plus radiometric and geometric coefficients. All ASTER images were downloaded in Hierarchical Data Format (HDF) image format.

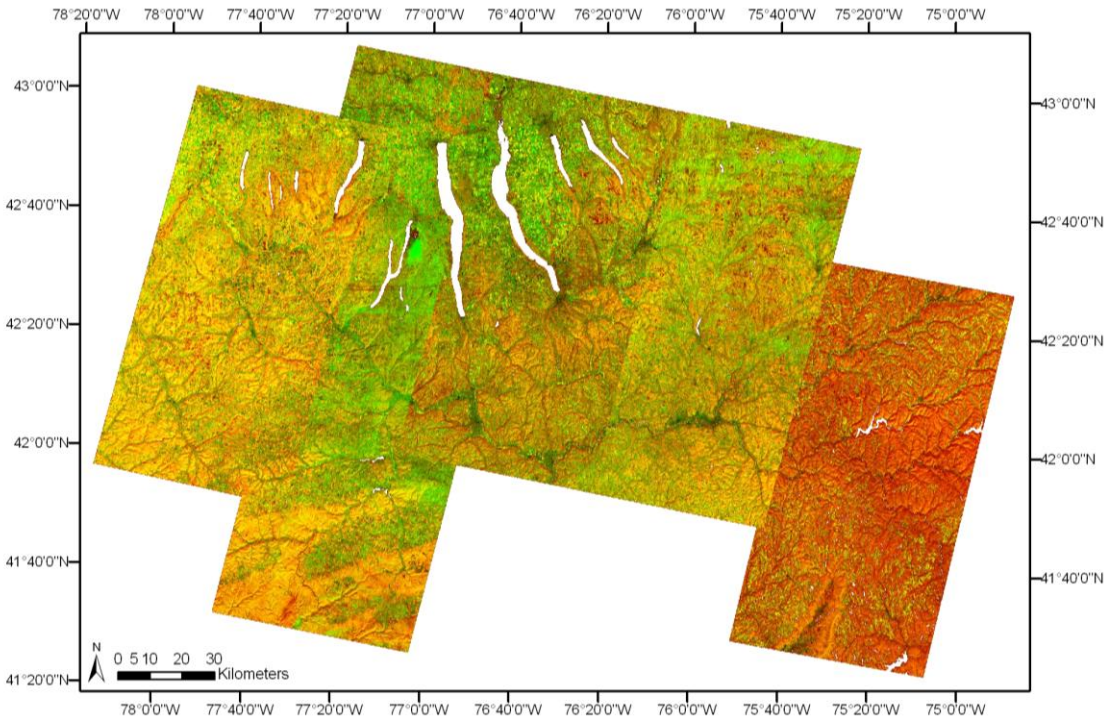

Figure 6.4,5&6-20. Principal component composite of 11 ASTER images mosaiced to cover the project area and displayed with PC composite bands R(PC2), G(PC3N). Figure from Zelazny et al. (2010) and Zelazny (2011).

Digital Elevation Model (Subtask 6.5)

A Digital Elevation Model (DEM) is a representation of the surface topography sampled in a regular grid. Bare-earth DEMs represent the Earth's surface after removing man-made objects and vegetation; therefore, they are especially useful for identifying geomorphological features and mapping topographic lineaments. USGS's National Elevation Data set (NED) contains bare-earth DEMs at three resolutions- 1 arc-second (~30 m), 1/3 arc-second (~10 m) and 1/9 arc-second (~3 m). The NED layers are derived from a variety of data sources including cartographic, photogrammetric, and Light Detection And Ranging (LIDAR). The DEM for the present project area was available at a resolution of 10 m or 1/3 arc-second from the U.S. Geological Survey's National Map Seamless Server website (http://seamless.usgs.gov/). The bounding coordinates of the selected DEM are North: 42°58'56.33", South: 41°57'28.44", West: 77°44'39.00", and East: 75°17'7.25". The DEM was downloaded in six Tagged Image File Format (Tiff) images (Figure 6.4,5&6-21).

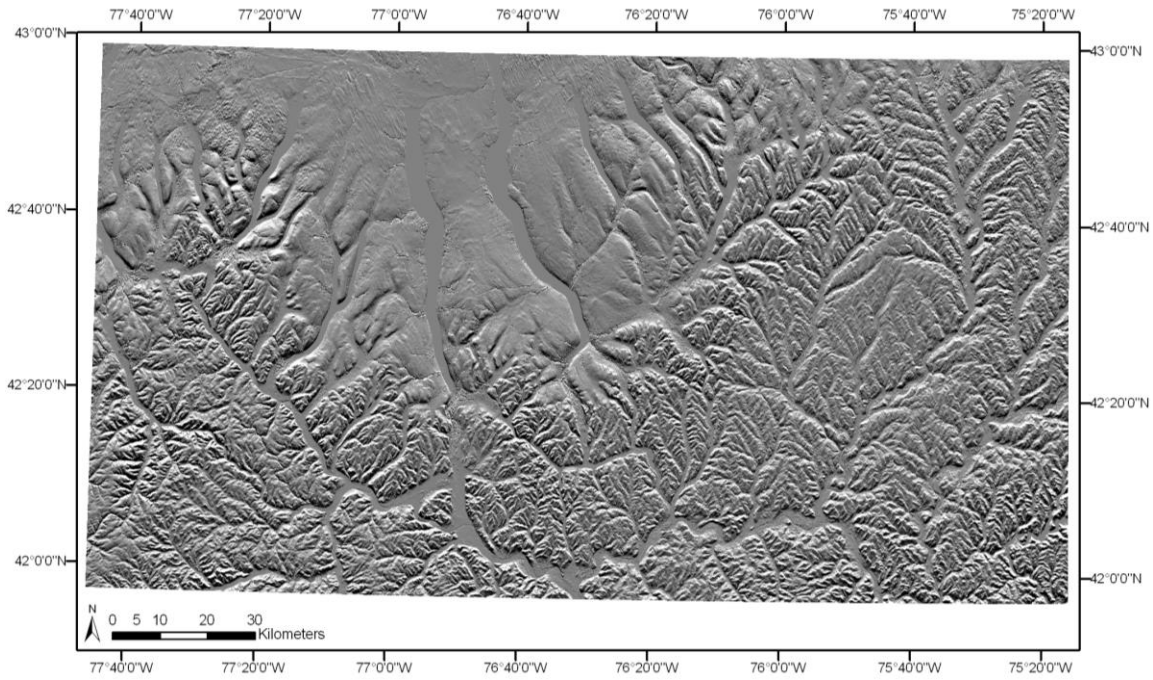

Figure 6.4,5&6-21. Shaded relief DEM from six, 10-meter resolution DEM tiles; sun angle/elevation is 25° and sun azimuth is 0°. Figure from Zelazny et al. (2010) and Zelazny (2011).

Auxiliary Data (Subtasks 6.4 & 6.5)

Other datasets were used to aid in visual interpretation, lineament identification, and digitizing. Most of the data were available from Cornell University Geospatial Information Repository (CUGIR - http://cugir.mannlib.cornell.edu/mapbrowse.jsp?series=counties). Each dataset was downloaded for each of the eight counties listed below from the 2000 census. The counties include Yates, Steuben, Schuyler, Chemung, Cayuga, Tompkins, Chenango, and Broome (Figures 6.4,5&6-22 – 6.4,5&6-25). The digitized drumlins were obtained directly from Dr. Dale Hess (Hess, 2009). The drumlins were manually digitized from a DEM and resulted in two datasets. The first dataset is digitized polygons along the outline of the drumlins (Figure 6.4,5&6-25) and the second dataset is digitized lines along the longest axis of the drumlin (Hess, 2009). The GIS vector layers depicting roads, railroads, and streams were downloaded from the Cornell University Geospatial Information Repository (CUGIR) website (www.cugir.mannlib.cornell.edu).

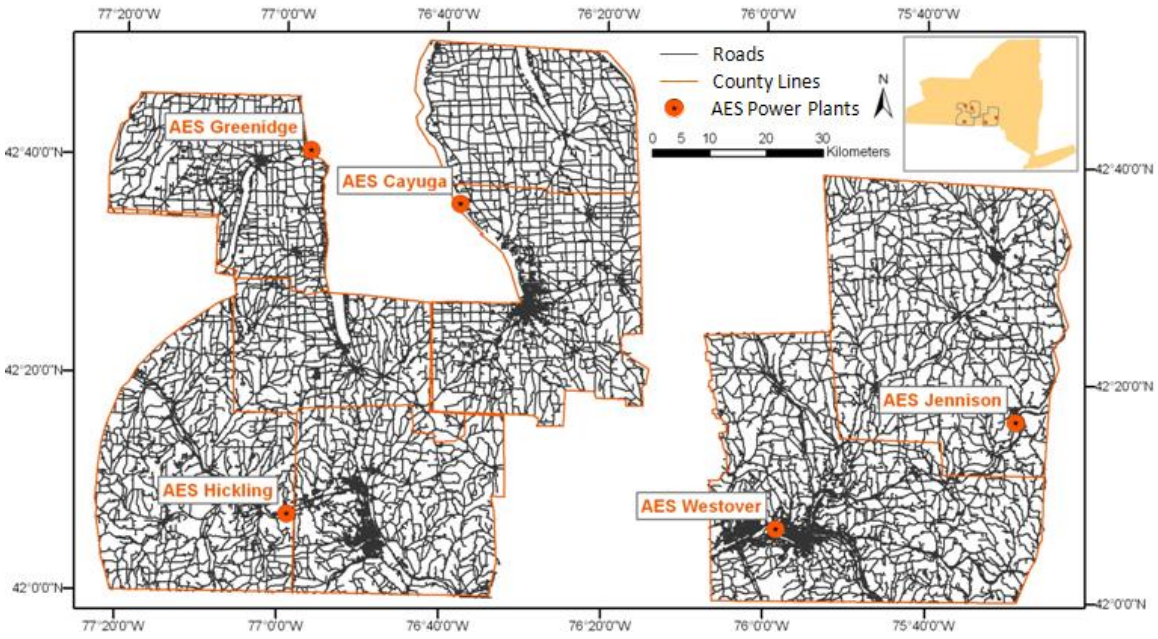

Figure 6.4,5&6-22. Major roads within the project area, downloaded from CUGIR. Figure from Zelazny (2011).

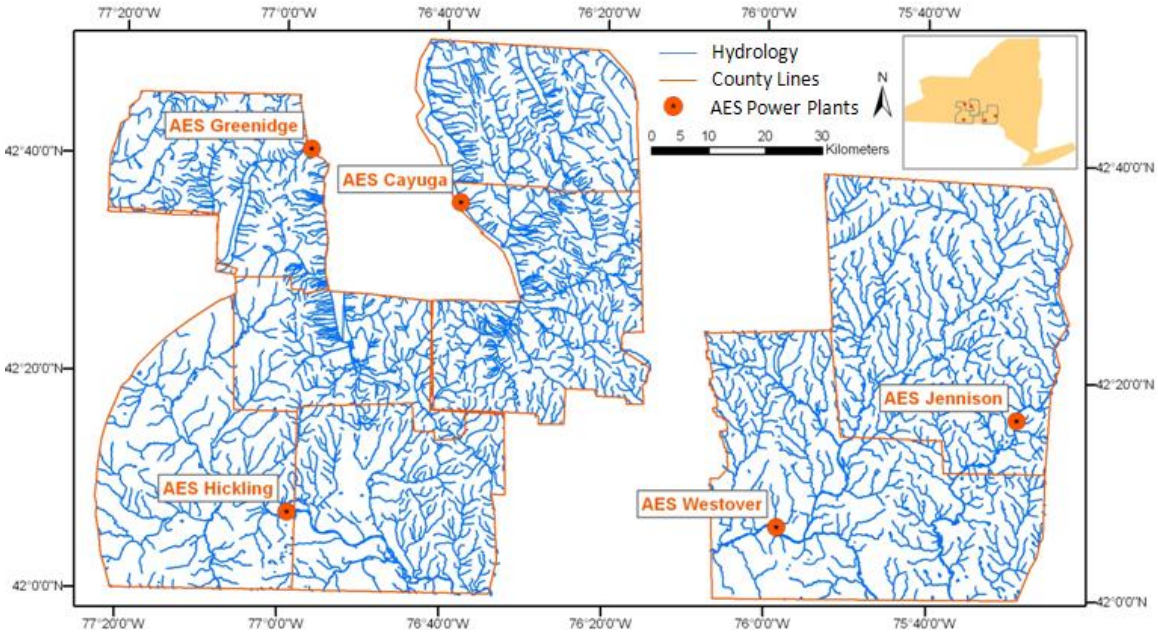

Figure 6.4,5&6-23. Major hydrologic features, such as rivers and streams, within the project area, downloaded from CUGIR. Figure from Zelazny (2011).

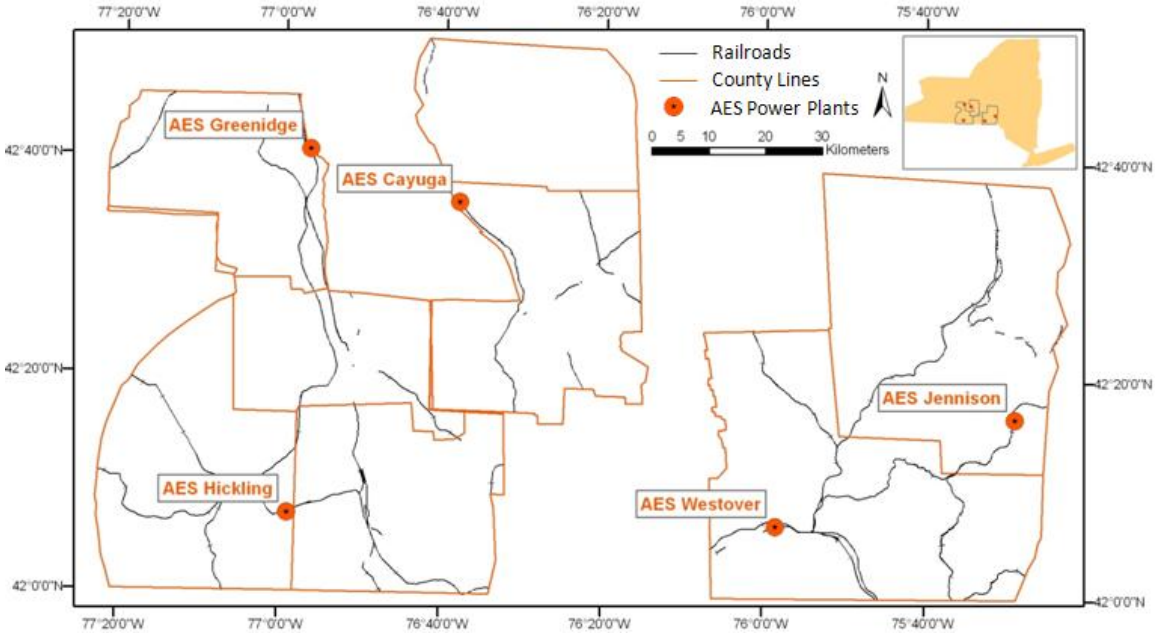

Figure 6.4,5&6-24. Railroad tracks within the project area, downloaded from CUGIR. Figure from Zelazny (2011).

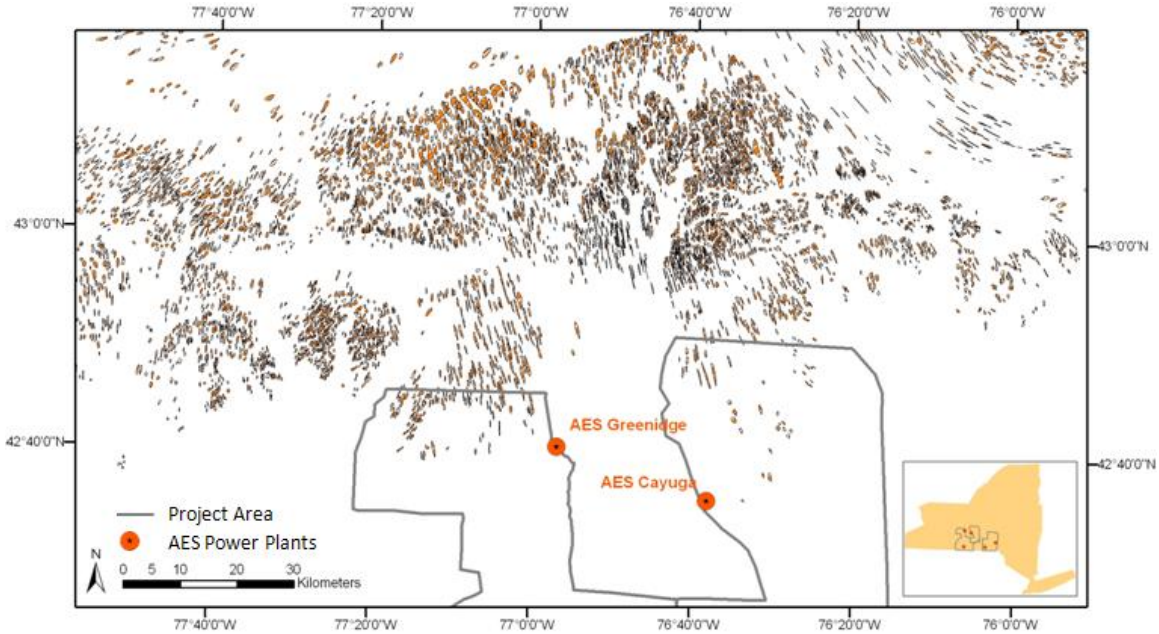

Figure 6.4,5&6-25. Drumlins in western NYS, digitized from a DEM by Hess (2009). Figure from Zelazny (2011).

METHODOLOGY

This project was accomplished by completing the methodology outlined in Figure 6.4,5&6-26.

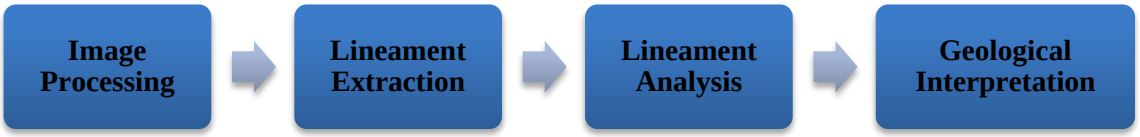

Figure 6.4,5&6-26. Steps used to complete project. From Zelazny (2011).

Remote Sensing Background (Subtasks 6.4 & 6.5)

Lineaments are rectilinear or slightly curvilinear mappable surface linear features that differ distinctly from the patterns of adjacent features and presumably reflects a subsurface phenomenon (O'Leary et al., 1976). According to Rahiman and Pettinga (2008), the subsurface of the Earth can be investigated using lineaments as evidence for tectonic fractures in the bedrock which are emphasized on the surface by geomorphological features such as topography, drainage, and vegetation. Lineaments are mapped from images by detecting changes in the surface reflectivity due to changes in vegetation coverage and topography. The satellite imagery used in this project includes Landsat Enhanced Thematic Mapper Plus (ETM+) and Advanced Spaceborne Thermal Emission and Reflection Radiometer (ASTER) imagery (Jensen, 2005; Abrams, 2000). DEM shaded relief representations are used for identifying lineaments that can be interpreted as topographic expressions.

Image processing techniques based on spectral and spatial variation of reflectivity and topography enhance differences in moisture content, vegetation health, topographic changes and overall tonal patterns, providing improved detection of lineaments. A commonly used technique for lineament mapping is band combinations, where various combinations of image bands are selected as RGB channels for color display. Principle component analysis is also commonly used, which is a statistical digital image processing technique used to reduce the redundancy of multispectral remote sensing images (Lillesand et al., 2004). A shaded-relief representation of Digital Elevation Models (DEM) enhances the expression of lineaments for identification and digitizing by creating shadows based on the direction of artificial sun illumination. Throughout this work, "R(x)" is used for the red channel, "G(x)" for the green channel, "B(x)" for the blue channel of color composite images and "x" for band numbers.

Image Processing and Enhancement (Subtasks 6.4 & 6.5)

Digital image processing is the manipulation of images using a series of procedures to improve their appearance for visual analysis and interpretation (Jensen, 2005; Lillesand et al., 2004). Different image

processing methods were used for enhancing the appearance of linear features by emphasizing tonal, topographic and textural changes. For example, a false-color composite display of different band and principal component combinations of ASTER and Landsat imagery and shaded-relief representations of the DEM with different illumination angles make the identification of lineaments easier and more robust. Image mosaicing is used to combine multiple scenes to produce a single image file. Color balancing was used to minimize the brightness and contrast differences between the different scenes; the master scene was selected interactively based on the image with the most balanced color (not too dark or light). The positioning of images and the selection of the image used for the mosaic in regions where several images overlapped were done interactively. All image processing was performed using ENVI 4.5 software (ITT Visual Image Solutions).

Landsat Imagery (Subtask 6.4). The preprocessing and processing steps of Landsat images included layer stacking, cropping, georeferenced mosaicing, band combinations and principal components (PC) transformation. The layer-stacking tool combines the VNIR, SWIR, and LWIR bands into a new multiband file which enables the manipulations of all bands simultaneously. The cropping tool was used to remove artifacts along the edges of the images. The four images, covering the focus area, were combined into a seamless mosaic by utilizing the georeferenced mosaicing tool.

Color composite images were created from different band combinations. The false color composite that combines one visible (VIS), one near-infrared (NIR) and one short-wave infrared (SWIR) band (R(7), G(4), and B(2)) usually shows a large color variation for different surface materials and is therefore frequently used for geologic interpretation (Figure 6.4,5&6-27). This composite shows the vegetation in green color, due to the high reflectance of vegetation in NIR, and detects differences in vegetation and moisture content (Jensen, 2005). The true or natural color composite of R(3), G(2), B(1) shows the image in its natural state as if the viewer were on the satellite platform (Figure 6.4,5&6-28). Band combination R(4), G(5), B(3) enhances the water-land boundaries within the image (Jensen, 2005). The combination of R(5), G(3), B(4) was found to highlight drainage patterns (e.g., Fernandes da Silva et al., 2005). This project relied primarily on true color and R(7) G(4) B(2) false color composites; experiments for this project indicated that the other two composites did not provide additional information so they were excluded from the study.

Principal Component Analysis (PCA) is a very effective method for analyzing multispectral satellite imagery. Previous research demonstrated the suitability of false color composite images using PC band combinations, for example R(PC2) G(PC1) B(PC4) for lineament extraction (Cruz et al., 2005; Drechsel et al., 2004; Everett et al., 2003; Everett et al., 2004). PCA transforms the original image bands into uncorrelated output bands. The maximum variance of the original data set is retained in the first PC band and the variance decreases toward higher order PC bands. The first three principal component bands typically provide more than 90% of the variance. PCA is often used for dimensionality reduction and for

creating color composite images with maximum information content. Comparison of different color composites indicated that the PC band combination of R(PC1), G(PC2), B(PC3) provided the best enhancement of linear features and tonal differences for this study (Figure 6.4,5&6-29). Lastly a Gaussian low pass filter was applied to reduce the noise in the image.

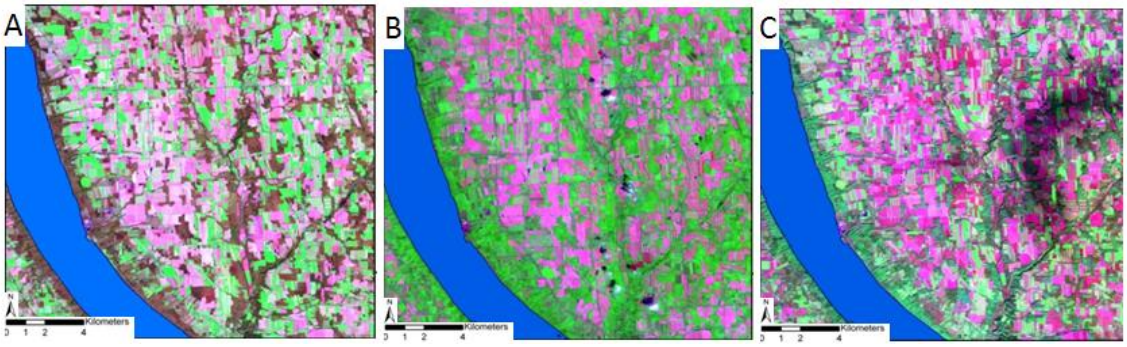

Figure 6.4,5&6-27. False color Landsat color composite; band combination R(7), G(4), B(2) for Grid 1. (A) image acquired April 28th 2001, (B) image acquired June 15th 2001, and (C) image acquired October 16th 1999. Figure from Zelazny et al. (2010) and Zelazny (2011).

Figure 6.4,5&6-28. True color Landsat color composite; band combination R(3), G(2), B(1) for Grid 1. (A) image acquired April 28th 2001, (B) image acquired June 15th 2001, and (C) image acquired October 16th 1999. Figure from Zelazny et al. (2010) and Zelazny (2011).

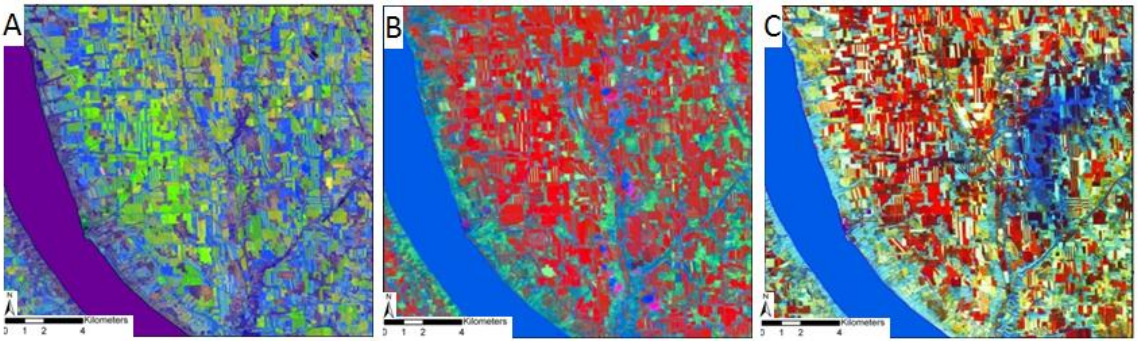

Figure 6.4,5&6-29. Principal component Landsat color composite; band combination R(PC1), G(PC2), B(PC3) for Grid 1. (A) image acquired April 28th 2001, (B) image acquired June 15th 2001, and (C) image acquired October 16th 1999. Figure from Zelazny et al. (2010) and Zelazny (2011).

ASTER Imagery (Subtask 6.4). ASTER image processing included georeferencing, layer stacking, masking, georeferenced mosaicing, principal components (PC) transformation, and a low pass Gaussian filtering. The first step of the processing was to create a geometrically and radiometrically corrected, geographically referenced image from the full resolution, unprocessed instrument data (Level 1A) using the georeferencing tool of ENVI. The layer stacking tool was used to combine the VNIR and SWIR bands into a new multiband, 15 meter resolution file, enabling the manipulation of all bands simultaneously. A mask was applied to all images to remove the water bodies within the image to improve further image processing (exclusion of low reflectivity values over large bodies of water improves the performance of principal component analyses, e.g., Cruz et al., 2005). The eleven ASTER scenes were combined to form a single image using the georeferenced mosaicing tool with color balancing to create a final mosaic. Finally, a low pass Gaussian filter was applied to reduce the noise in the image.

A color composite of band combination of R(2), G(3N), B(1) provided the greatest color contrast for extracting linear features (Figure 6.4,5&6-30a) among all attempted possible band combinations. The PC band combination of R(PC2), G(PC1), B(PC3) provided the best overall image due to its enhanced linear features and tonal differences (Figure 6.4,5&6-30b). All VNIR and SWIR bands were used for the PCA.

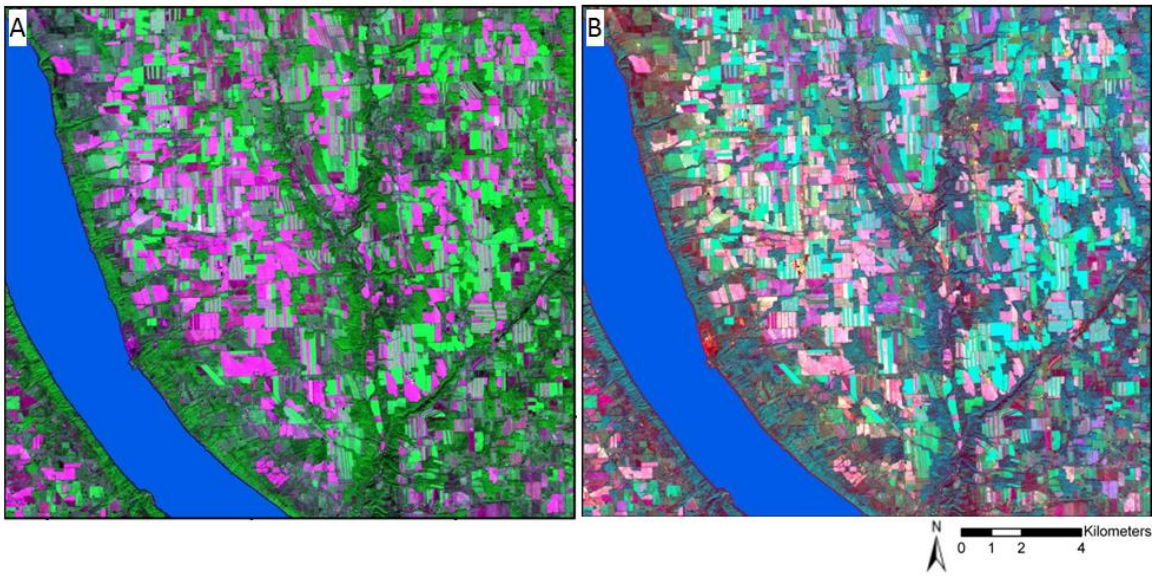

Figure 6.4,5&6-30. ASTER September 14th 2005 image for Grid 1. (A) color composite of R(2), G(3N), B(1); (B) color composite of R(PC2), G(PC1), B(PC3) principal components. Figure from Zelazny et al. (2010) and Zelazny (2011).

Digital Elevation Model (DEM) (Subtask 6.5). National Elevation Data set (NED) DEMs do not require any preprocessing. However, attention should be paid to selecting DEM visualizations suitable for lineament mapping. Although a simple gray scale or color image of a DEM depicts the general topography of the terrain, it lacks subtle details and therefore is not suitable for lineament mapping. Different visualization methods, especially shaded relief representations of DEMs, have been effectively used for enhancing terrain features to support lineament extraction. For example, Peña and Abdelsalam (2006) mapped lineaments using shaded relief DEMs in Southern Tunisia. For a shaded relief representation, the brightness of a grid cell is determined by the angle between the surface normal and illumination direction, creating an illusion of a terrain illuminated from a user defined position of the sun.

The two main inputs the user provides for creating a hill shade map are the solar elevation angle (angle from the horizon) and the solar illumination angle or azimuth (orientation of the sun's rays with respect to north). A solar elevation angle of 45° was initially selected, but the angle was changed to 25° because lower sun angles were more effective in enhancing subtle topographic changes in low relief regions such as the prospect area. The lower sun angle resulted in more shadows, thus increasing the ease of lineament identification. Varying the sun illumination angle promotes identification of more lineaments on the different views of the same area, since the lineaments orthogonal to the illumination angle are enhanced. Solar illumination directions of 0°, 45°, 90°, 270° and 315°, perpendicular to the prominent lineaments in the region, were selected to enhance the linear features (Figure 6.4,5&6-31). Four illumination angles were used for Grid 1, but only 0° was utilized for the entire project area; this illumination angle resulted in a

reduced number of north-south trending DEM lineaments (parallel to the solar illumination direction) compared to north-south trending lineaments in the other images.

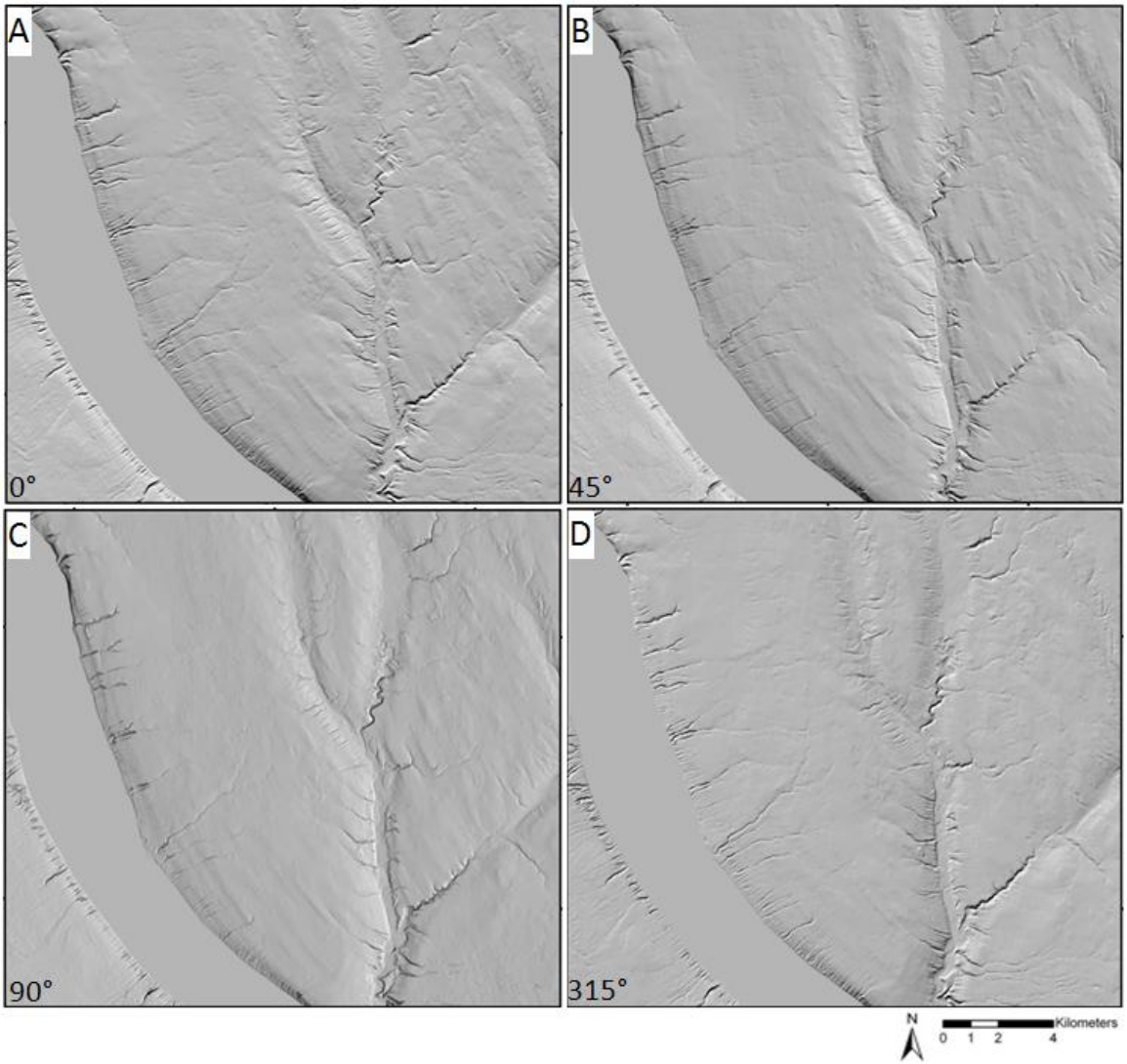

Figure 6.4,5&6-31. 10m resolution NED DEM for Grid 1 with shaded relief representation with sun angle 45° and azimuth of (A) 0°, (B) 45°, (C) 90° and (D) 315°. Figure from Zelazny et al. (2010) and Zelazny (2011).

<u>Lineament Extraction and Analysis (Subtasks 6.4, 6.5, and 6.6).</u>

The methodology utilized in this project was similar to the that followed by several researchers, such as Cruz (2005) and Rahiman and Pettinga (2008), who used four major steps in lineament analysis: (1) acquisition of lineament data from multiple images, (2) analysis to identify significant data, (3) presentation as statistical and spatial plots, and (4) comparison of lineaments with fracture data from the field.The lineament extraction and analysis of this project was accomplished in three phases. Phase I was primarily

focused on digitizing and analyzing lineaments in a small area (Grid 1) using multiple satellite imagery and shaded relief DEMs at a scale of 1:65,000 in order to realize the optimal image processing techniques for this region. In Phase II lineaments were extracted and analyzed for the entire project area from ASTER PC color composites and shaded relief DEMs illuminated from the north at a scale of 1:125,000. In Phase III lineaments were extracted and analyzed for the Cayuga power plant subset at a scale of 1:25,000 for a detailed study.

Lineament Extraction (Subtasks 6.4 & 6.5). Color composite images and shaded relief DEMs were imported into an ArcGIS 9.3 project and displayed with auxiliary data including roads, railroads, drumlin outlines and hydrology. The auxiliary data were overlain on the image mosaic or map to assure that man-made features were not mistakenly identified as a structurally-related lineament. This operation created a situation in which geological structures coincident with man-made features could mistakenly be excluded.

To store the digitized lineaments as polylines together with associated lineament information such as the length, orientation and category, a geodatabase was created using ESRI's ArcCatalog. The category described the type of lineament based on the clues used for mapping, namely drainage pattern, tonal variation, vegetation difference, or the presence of a series of connecting lakes. A lineament was selected if its straight (non-curved) length was greater than a pre-determined minimum length. For curved lineaments multiple strength line segments were used to digitize the lineament. The lineament extraction, which includes identification and digitizing, was accomplished in three phases. The scale at which lineaments were digitized varied from 1:25,000 (Cayuga subset); 1:65,000 (Grid 1) and 1:125,000 (entire project area), and the minimum length of digitized lineaments was 0.5 km, 0.5 km and 1 km, respectively.

For quality control weekly meetings were held throughout the lineament identification process with Dr. Jacobi and Dr. Csatho. The previous week's work was reviewed by Dr. Jacobi to ensure that all possible lineaments were identified. Both Jacobi and Csatho confirmed identified lineaments and identified new ones. Each meeting included a discussion of the criteria used for lineament identification and why a given linear feature was classified as a lineament (or not). This process helped re-focus the operator's eyes and provided different viewpoints of the lineament identification.

Lineament Analysis (Subtasks 6.4 & 6.5). According to Peña and Abdelsalam (2006), the objective of a lineament analysis is to derive information about geological structures from the length, azimuth direction and spatial distribution of lineaments. The statistical analyses of the lineaments in the present study were based on the length and orientation of the lineaments; the analyses provided the total count (number of lineaments) and the total, maximum, median length and average length as well as the standard deviation of the length (all in meters). This analysis was accomplished by converting the ArcGIS geodatabase into a Microsoft Excel spreadsheet where the analysis was performed.

Rose diagrams were generated to show the orientation distribution of the lineaments. Grapher Six (Golden Software Inc.) and RockWorks (RockWare) software tools were utilized to construct rose diagrams. Since ArcGIS, the program in which the lineaments were digitized, does not calculate the orientation of lineaments automatically, a data field was added and named orientation/azimuth in the attribute table of the ArcMap geodatabase. With the assistance of Cheri Cruz, a script downloaded from http://www.ian-ko.com/ calculated and stored the azimuth of the lineament in the new orientation/azimuth field. After this step was completed, rose diagrams were made using RockWorks.

After the completion of phases I, II, and III, additional analyses beyond the basic statistics and rose diagrams were performed. Additional analyses performed on the digitized lineaments for the entire project area and the Cayuga power plant subset included the generation of histograms, spatial rose diagram analysis and generation of lineament density maps. Histograms of lineaments in orientation bin sizes of 2° were made using the histogram tool in the RockWorks Utility.

A spatial rose diagram analysis was performed to determine if the trends of lineaments digitized from the ASTER images change across the entire project area (including the Cayuga power plant subset). The lineaments in question for the Cayuga subset were digitized at a scale of 1:25,000 and had a minimum lineament length 0.5 km, and for the entire project area the lineaments were digitized at a scale of 1:125,000 and had a minimum lineament length 1.0 km). For spatial rose diagram analysis, the prospect area was gridded and rose diagrams were produced for each grid cell. A grid cell size of 7.5 km by 7.5 km ($56.25 km^2$) was selected for the Cayuga subset and 15 km by 15 km ($225 km^2$) grid for the entire project area. All lineaments that were fully and partially within a grid cell were considered for the rose diagram of that particular grid cell. The result was 13 rose diagrams for the Cayuga subset and 55 rose diagrams for the entire project area. Each rose diagram was based on the number of lineaments (count) in each orientation bin of 10°. These rose diagrams were then overlaid on a grey scale Landsat image mosaic (Band 8, panchromatic, 15 m resolution band) to show changes in the patterns and distribution of the lineaments based on primary and secondary trends. The rose diagrams across the project area and Cayuga subset were then examined to determine variations in lineament orientations that may be related to, or influenced by, variance in the tectonic stresses.

Lineament density maps were also constructed to improve our overall understanding of the clustering of lineaments with specific orientations. Density maps display the number of lineaments per defined area, which facilitates the identification of regions with a relatively high number of lineaments (and possibly fractures or faults) density and areas lacking lineaments. To obtain a density map, a grid structure is defined and each lineament that is at least partially within a grid cell it is counted toward the total number of lineaments in this grid cell. Density maps for the entire project area and the Cayuga power plant subset

were compiled from the lineaments extracted from ASTER imagery and from the shaded relief DEM. Density maps for all orientations as well as for specific orientation ranges were generated using RockWorks and Surfer. The specific orientation ranges used in the density maps were defined by the distribution of lineament orientation populations for lineaments digitized during Phase II and Phase III. Density maps were computed from all lineament orientations as well as for lineaments with the specific orientation groups determined in this project (Figure 6.4,5&6-54): WNW (285° – 301°), NW (301° - 335°), NNW (335° – 350°), NS (350° – 11°), NNE (11° -21°), NE (21° – 59°), ENE (59° – 79°) and EW (79° – 105°). These density maps with specific lineament orientation groups will be referred to as filtered density maps or density map of specific orientation.

Density maps, based on lineament count, were made using the lineation gridding tool in RockWorks Utilities. Different grid cell sizes (node spacing) were used for the whole project area (.333 square mile for all orientations and 0.125 square mile for the specific orientations) and the Cayuga subset (.05 square miles). The density grid files were then exported from RockWorks, converted into a format that could be imported into Surfer utilizing MatLab and then imported into Surfer 8 (Golden Software) because of its better contouring capabilities. Maps were then created for all orientations and for specific orientations; two additional maps show a density grid from all lineament orientations with lineaments and roads overlaid.

Geologic Interpretation (Subtask 6.6). The geologic interpretation for this project was accomplished by two analyses - fabric and stratigraphic analysis. The fabric analysis compared various datasets (e.g., faults, fractures and fault zones) to the digitized lineaments, and the results were reported in fabric compilation tables and maps.

In order to test whether Set I & Set II fractures of Engelder and Geiser (1979, 1980) are coincident with similarly-oriented lineaments, Set I & Set II fracture data from Engelder and Geiser (1979, 1980) were imported into ArcGIS by digitizing the field site locations and fracture trends from figures 3 and 6 in Engelder and Geiser (1979, 1980). To allow for possible mislocation of fracture sites in georeferencing Engelder and Geiser's (1979, 1980) figures, and because the fractures in the maps of figures 3 and 6 of Engelder and Geiser (1980) were portrayed as 5 km long lines, the digitized fractures were represented by 5 km-long linear features oriented along the fracture trend. In ArcGIS a buffer was then applied to the digitized linear features that represent the fractures. A buffer is a zone around a map feature that covers an area up to a predetermined distance away from the feature (Figure 6.4,5&6-32). A buffer is a circle around a point feature (e.g., location of a fracture measurement) and a corridor along a linear feature (e.g., a fault; Figure 6.4,5&6-32). The buffers applied to Engelder and Geiser's (1980) fracture linear features were 1 km, resulting in a 7 km long, 2 km wide buffer for each of Engelder and Geiser's (1980) fracture measurement. ASTER lineaments that intersect these buffers and are oriented within 20° of the fracture trends were then identified. The selected ASTER lineaments and the corresponding fracture sites were used

to generate the fabric tables, as well make maps and rose diagrams for the entire project area, western focus area, central focus area and eastern focus area. The fabric compilation table shows the number and total length of fracture data and ASTER lineaments within determined orientations of EW (259° – 281°), WNW (281° – 304°), NW (304° – 326°), NNW (326° – 348°), NS (348° – 11°), NNE (11° – 34°), and ENE (56° – 79°). For other fracture data, the process was slightly different: the fractures were represented by point data with a 1 km buffer applied to the point, resulting in a circle for a buffer (Figure 6.4,5&6-32). For the Terech (2006) fracture data, Terech's (2006) orientation boundaries were utilized of EW (265° – 277°), WNW (277° – 322°), NW (322° – 342°), NS (342° – 7°), NNE (7° – 45°), and ENE (45° – 85°). For McGuire's (2007) fracture data, orientations of EW (265° – 282°), WNW (282° – 304°), NW (305° – 323°), NNW (323° – 344°), NS (345° – 9°), NNE (9° – 40°), NE (41° – 55°), and ENE (56° – 84°) were used. From these tables the orientations of ASTER lineaments that are best supported by mapped geologic structures such as fractures, faults, and fault zones were determined.

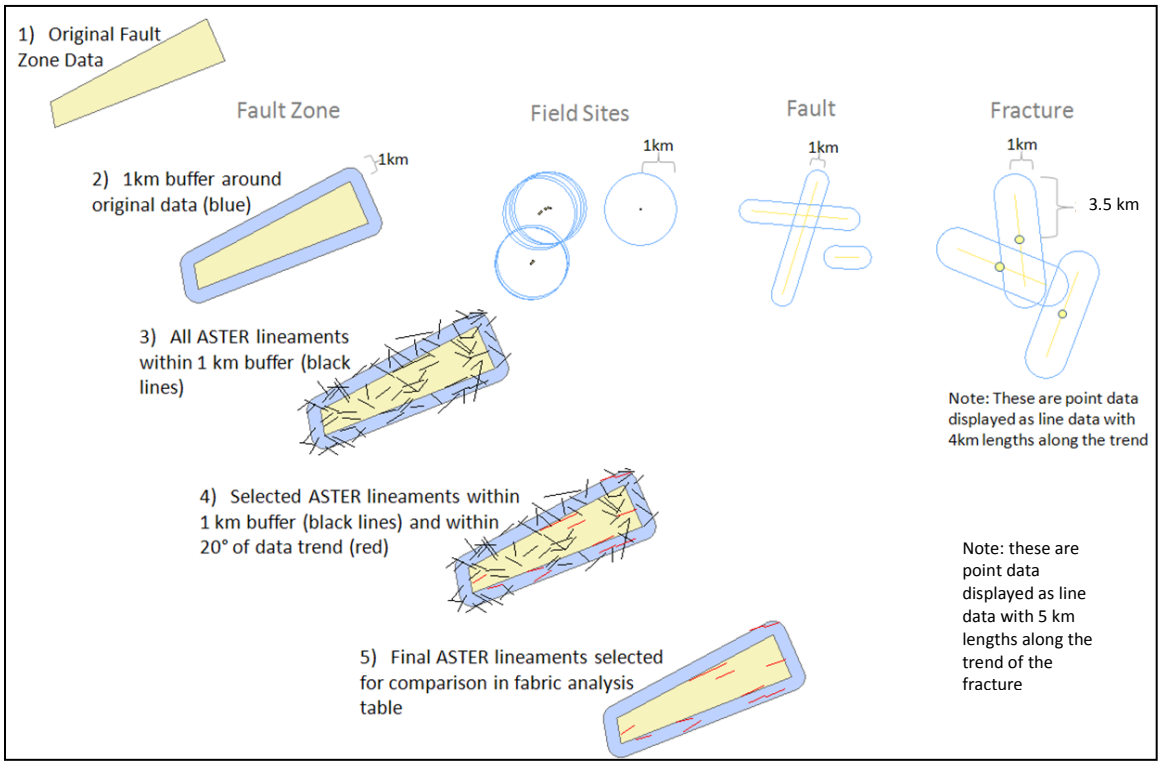

Figure 6.4,5&6-32. Schematic showing the buffering of geologic structures for ASTER lineament selection. ASTER lineament and structure orientations are compared in the fabric analysis tables (Tables 6.4,5&6-1 – 6.4,5&6-4). Figure from Zelazny (2011).

For fault and fault zone data from Bradley et al. (1941), Isachsen and Mckendree (1977), Murphy (1981) and Jacobi (2002, 2007a, b), the process was similar to that for the fractures of Engelder and Geiser (1980).

The fault or fault zone was digitized from the published source, and a 1 km buffer was created around the digitized linear feature. The intersecting ASTER lineaments with orientation within 20^0 of the fault trend were then compiled into a fabric analysis table, as well as maps and rose diagrams.

Another analysis that aided in the geologic interpretation was the stratigraphic analysis which was used to gain insight into possible variations of lineament orientation with respect to the age and tectonic history of different geologic formations. Three depositional groups exposed in the project area were utilized: (1) the Hamilton Group, (2) the Tully Ls, Genesee and Sonyea groups (combined in geologic map) and (3) the West Falls Group. The geologic map of NYS (Isachsen et al., 1991) was used as a basemap in ArcGIS to identify the boundaries between the three groups. ASTER lineaments within the geologic units were selected and separated into individual files in ArcGIS; these files were used to make rose diagrams in RockWorks.

RESULTS

Lineament Mapping (Subtasks 6.4, 6.5, and 6.6)

Phase I – Selection of Best Remote Sensing Data and Image Processing Methods for Lineament Mapping (Subtasks 6.4 and 6.5). The purpose of this initial phase was to select the best images and DEM representations for lineament mapping from a comprehensive set of products (Table 6.4,5&6-1). A small test site, covering a 225 km^2 region east of Cayuga Lake and including the AES Cayuga power plant, was selected for this part of the study (Figure 6.4,5&6-3, Grid 1). This region was also previously studied by Cruz (2005). Lineaments were identified from 15 different satellite image products and shaded relief DEMs at a 1:65,000 scale (Figures 6.4,5&6-33 to 6.4,5&6-37). Only lineaments longer than 0.5 km were mapped; previous work by Jacobi (2002) and Jacobi et al. (2002) suggested lineaments in excess of 0.5 km correlated best with fracture intensification domains (FIDs). This phase of the lineament identification process took place between April 2009 and July 2009.

Landsat Imagery – *April 28th 2001, June 15th 2001 and Oct. 16th 1999*
True-Color composite R(3),G(2), B(1)
False-Color composite R(7),G(4), B(2)
Principal Component R(PC1),G(PC2), B(PC3)
ASTER Imagery – Sept. 14th 2005
Color composite R(2),G(3N), B(1)
Principal Component R(PC2),G(PC1), B(PC3)
DEM – *Sun elevation angle 45° - Shaded relief map*
Sun Illumination 0°
Sun Illumination 45°
Sun Illumination 90°
Sun Illumination 315°

Table 6.4,5&6-1: Satellite image composites and shaded relief DEMs generated in Phase I. Table from Zelazny (2011).

In Phase I, various image enhancing and visualization techniques were tested for ease of lineament recognition by increasing the contrast of the image. Of all 15 images reviewed for lineaments, the ASTER PC composites and shaded relief DEM with sun illumination angle of 0° had the highest lineament count and total length. Lineaments were more easily recognized on these images. Therefore only these data products were used for the remainder of the project.

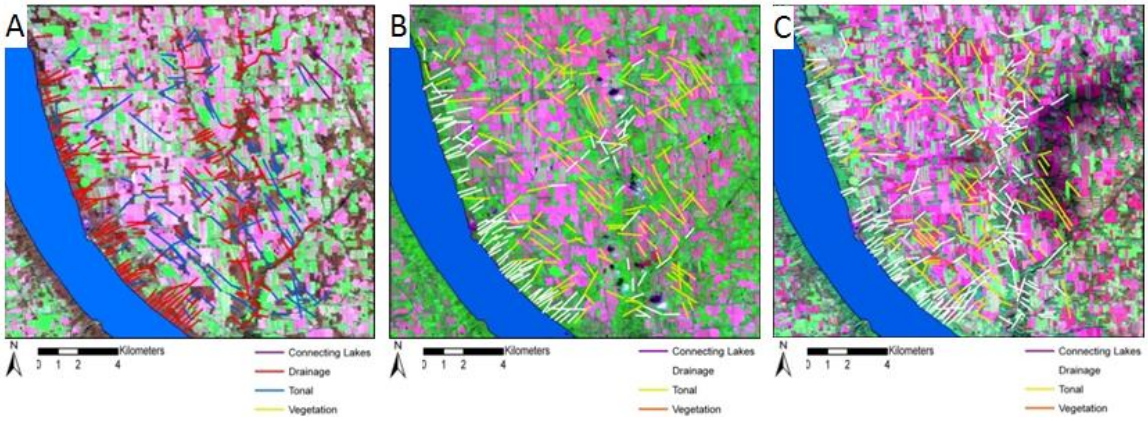

Figure 6.4,5&6-33. Phase I - False color Landsat color composite; band combination R(7), G(4), B(2) for Grid 1 with digitized lineaments. (A) image acquired April 28th 2001, (B) image acquired June 15th 2001, and (C) image acquired October 16th 1999. Figure from Zelazny Zelazny et al. (2010) and (2011).

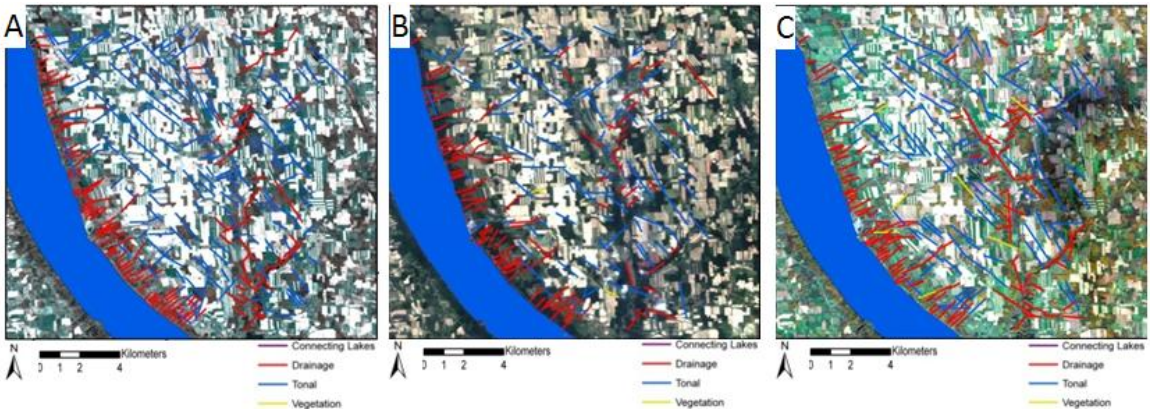

Figure: 6.4,5&6-34. Phase I - True color Landsat color composite; band combination R(3), G(2), B(1) for Grid 1 with digitized lineaments. (A) image acquired April 28th 2001, (B) image acquired June 15th 2001, and (C) image acquired October 16th 1999. Figure from Zelazny et al. (2010) and Zelazny (2011).

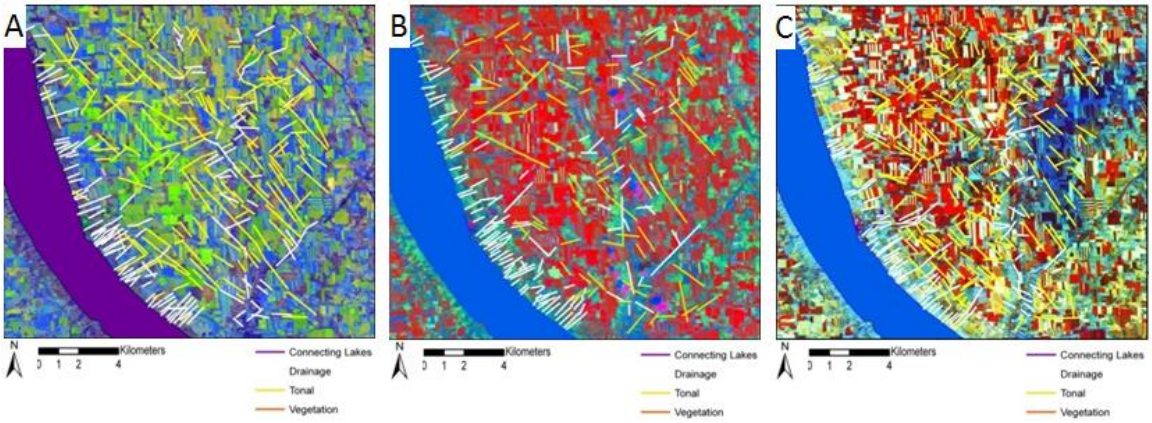

Figure 6.4,5&6-35. Phase I - Principal component Landsat color composite; band combination R(PC1), G(PC2), B(PC3) for Grid 1 with digitized lineaments. (A) image acquired April 28th 2001, (B) image acquired June 15th 2001, and (C) image acquired October 16th 1999. Figure from Zelazny et al. (2010) and Zelazny (2011).

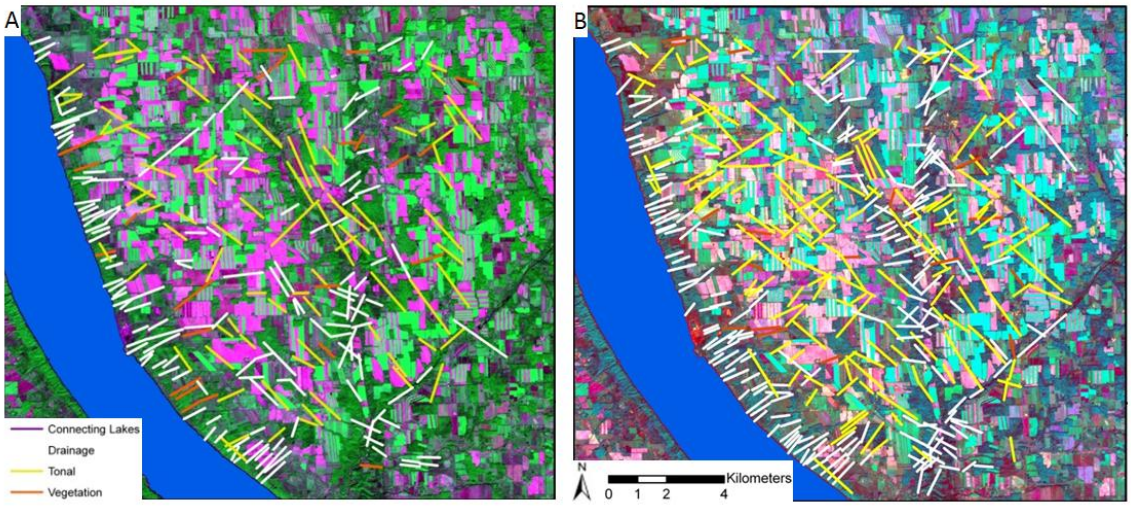

Figure 6.4,5&6-36. Phase I - ASTER September 14th 2005 image for Grid 1 with digitized lineaments. (A) color composite of R(2), G(3N), B(1) and (B) color composite of R(PC2), G(PC1), B(PC3) principal components. Figure from Zelazny et al. (2010) and Zelazny (2011).

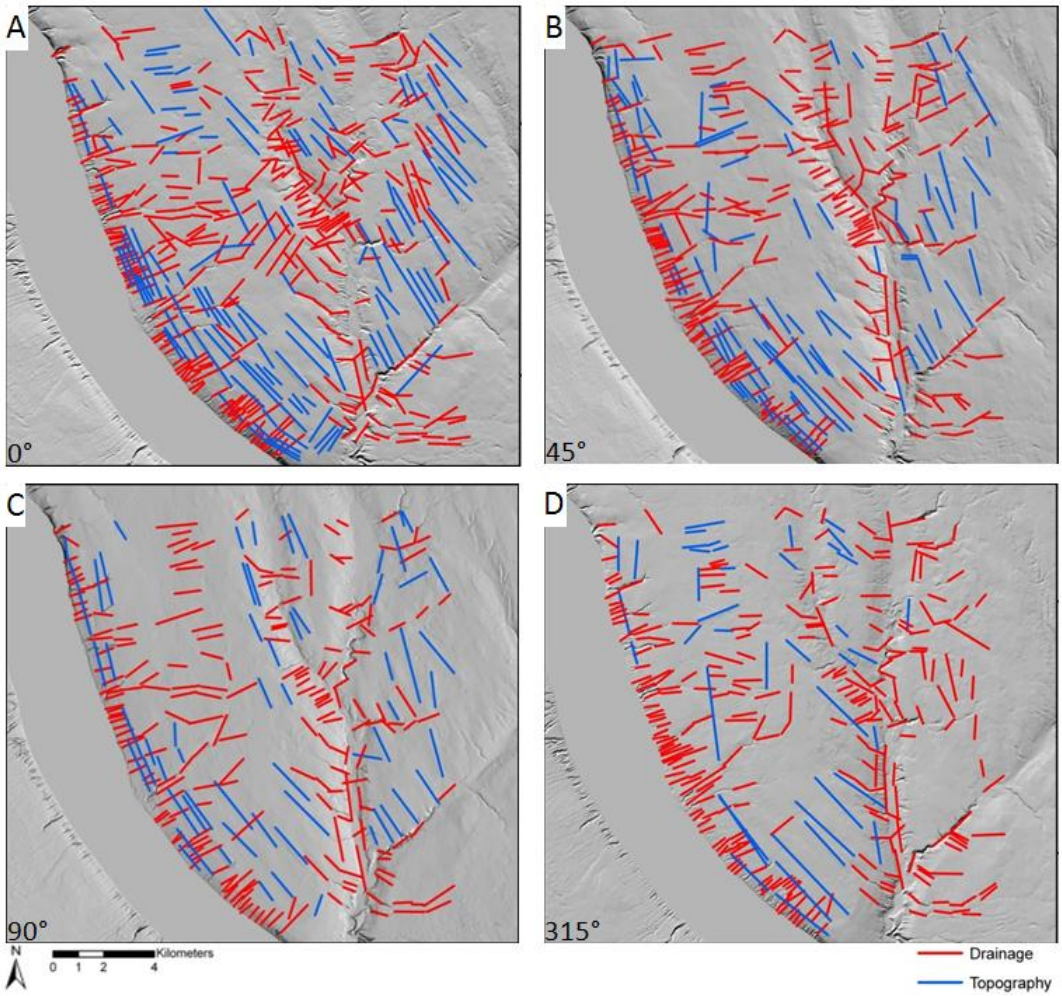

Figure 6.4,5&6-37. Phase I - 10m resolution NED DEM, shaded relief representation for Grid 1 showing digitized lineaments with sun elevation/angle 45° and azimuth of (A) 0°, (B) 45°, (C) 90° and (D) 315°. Figure from Zelazny Zelazny et al. (2010) and (2011).

Basic statistics of the lineaments (i.e. count, total length, average length, median length, maximum length, and standard deviation of length) are shown in Table 6.4,5&6-.2. The distribution of lineament orientations displayed on rose diagrams with 10° bins (Figures 6.4,5&6-38 to 6.4,5&6-40). The lineaments digitized from most satellite images revealed a primary trend of 55° and a secondary trend of 315°. Lineaments digitized from all shaded relief DEMs typically had a primary trend of 65° and a secondary trend of 325°. These trends indicate that the lineaments identified could be related to ENE and NW trending fractures and faults in the region (e.g., Engelder and Geiser, 1980; Jacobi, 2002, 2007).

	Total Count	Total Length m)	Average Length m)	Median Length (m)	Standard Deviation
ASTER Imagery					
Sept. 2005 Color Composite	252	221,044	887	802	164
Sept. 2005 Principal Component Composite	364	320,762	839	733	168
Digital Elevation Model					
Shaded Relief DEM with sun azimuth (0°)	454	404,530	858	688	167
Shaded Relief DEM with sun azimuth (90°)	270	233,561	861	655	151
Shaded Relief DEM with sun azimuth (45°)	357	299,702	890	773	139
Shaded Relief DEM with sun azimuth (315°)	300	243,598	874	727	281
Landsat Image					
April 2001 True Color Composite	281	254,040	746	741	158
April 2001 False Color Composite	267	227,942	800	688	123
April 2001 Principal Component	292	302,306	940	844	138
June 2001 True Color Composite	189	170,027	849	808	157
June 2001 False Color Composite	256	229,003	868	790	135
June 2001 Principal Component	209	190,473	867	754	237
Oct. 1999 True Color Composite	229	222,011	970	775	315
Oct. 1999 False Color Composite	277	227,335	825	724	128
Oct. 1999 Principal Component	294	246,950	823	749	165

Table 6.4,5&6-2. Phase I - Statistics of lineaments extracted from different remote sensing data in Grid 1. Lineament extraction scale was 1:65,000 and minimum lineament length is 0.5 km (see Table 6.4,5&6-1 for details on band combinations). From Zelazny (2011).

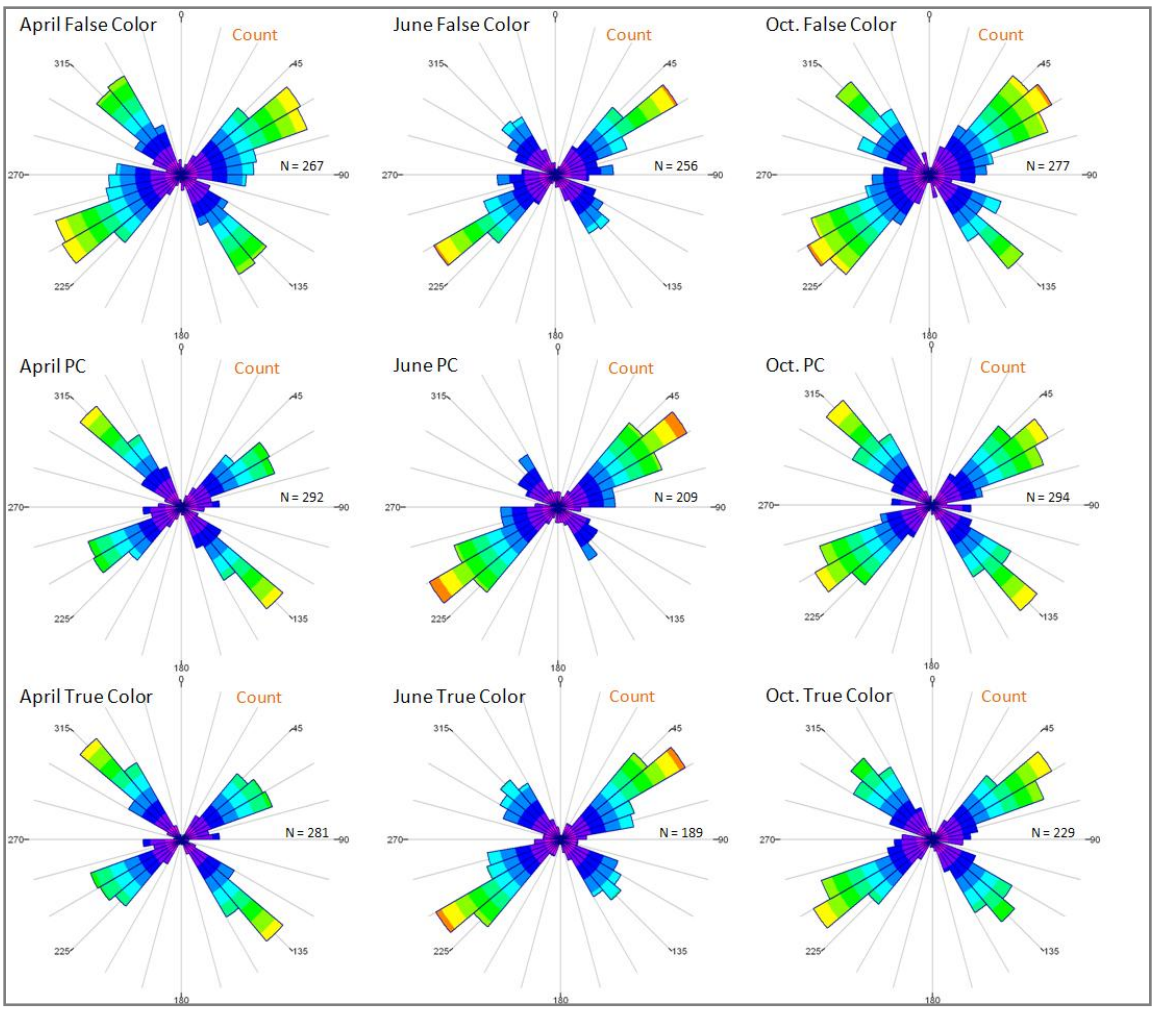

Figure 6.4,5&6-38. Rose diagrams of Landsat lineament orientations in Grid 1 from Phase 1. Lineaments digitized from Landsat ETM+ imagery. Lineament extraction scale was 1:65,000 and minimum lineament length is 0.5 km. N is the total number of lineaments digitized from the image. From Zelazny (2011).

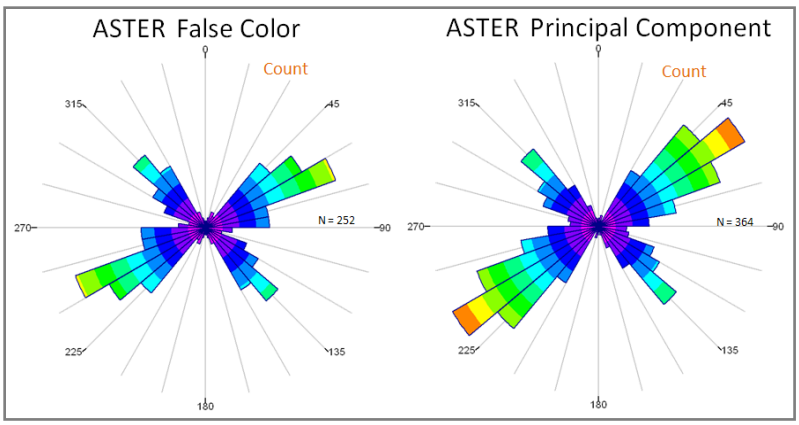

Figure 6.4,5&6-39. Rose diagrams of ASTER lineament orientations in Grid 1 from Phase I. Lineaments digitized from ASTER imagery. Lineament extraction scale was 1:65,000 and minimum lineament length is 0.5 km. N is the total number of lineaments digitized from the image. From Zelazny (2011).

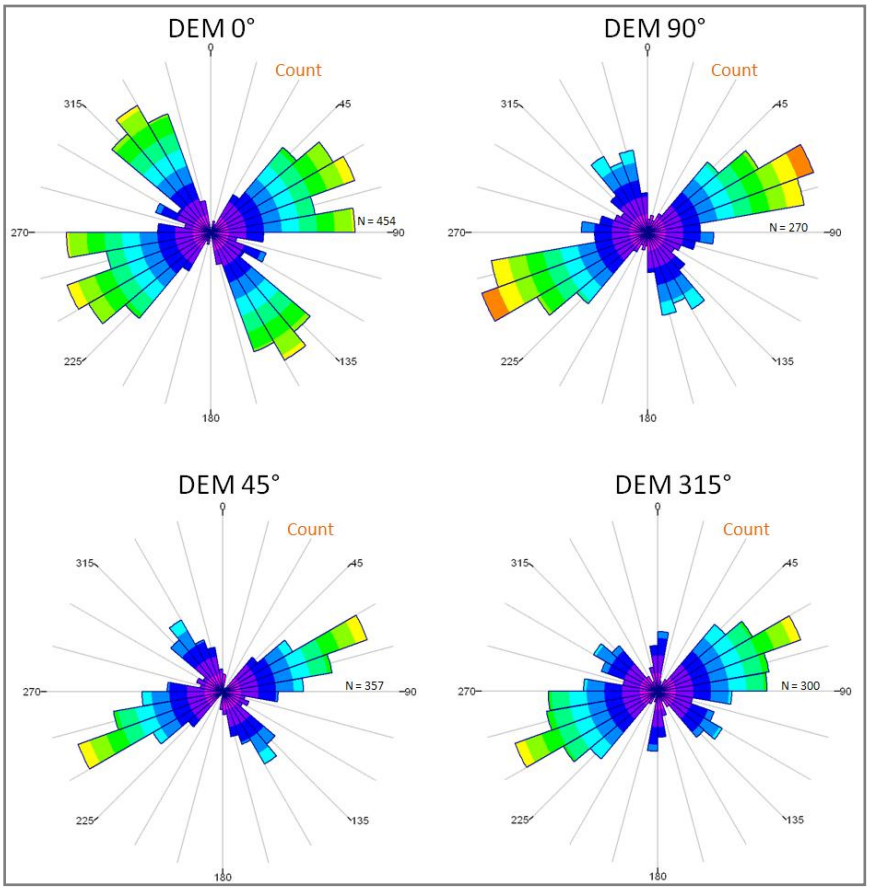

Figure 6.4,5&6-40. Rose diagrams of topographic lineament orientations in Grid 1. Lineaments digitized from shaded relief DEMs. Solar illumination (azimuth) angles are 0, 45, 90 and 315 degrees, solar elevation angle is 45 degrees, lineament extraction scale was 1:65,000 and minimum length is 0.5 km. N is the total number of lineaments digitized from the image. From Zelazny (2011).

Phase II – Lineament analysis of the entire project area(Subtasks 6.4 and 6.5). Phase II encompassed the entire project area of eight counties (Figure 6.4,5&6-3). For this larger region, a smaller scale of 1:125,000 and a larger minimum lineament length of 1 km were used. Based on the result of the Phase I analysis, the ASTER Principal Component composite of (R(PC2), G(PC1), B(PC3)) was selected and shaded relief DEMs with a sun illumination angle of 0° for lineament mapping was utilized (Table 6.4,5&6-3; Figures 6.4,5&6-41 and 6.4,5&6-42; for more detailed images with lineaments for the western, central, and eastern focus areas, see Appendix A).

ASTER Imagery
Principal Component R(PC2), G(PC1), B(PC3)
DEM – *Sun elevation angle 25°*
Sun Illumination 0°

Table 6.4,5&6-3. ASTER color composites and shaded relief DEMs used in Phase II. From Zelazny (2011).

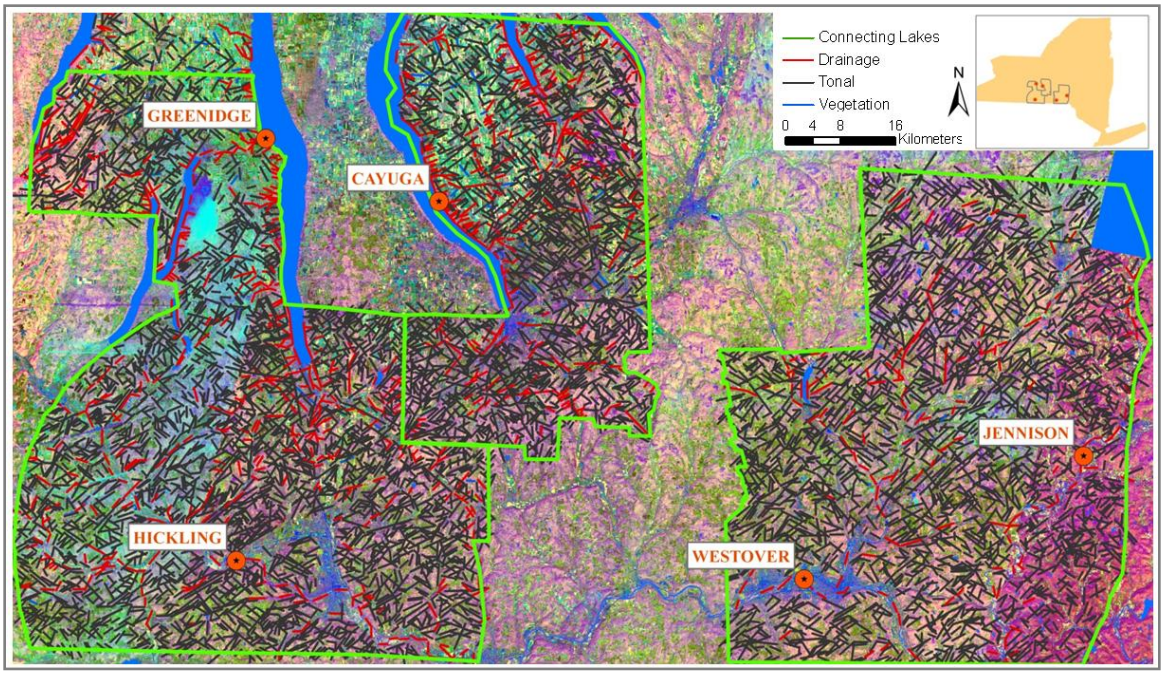

Figure 6.4,5&6-41. Phase II –ASTER principal component color composite mosaic with digitized lineaments over the entire project area; Principal Component composite R(PC2),G(PC1), B(PC3). From Zelazny et al. (2010) and Zelazny (2011).

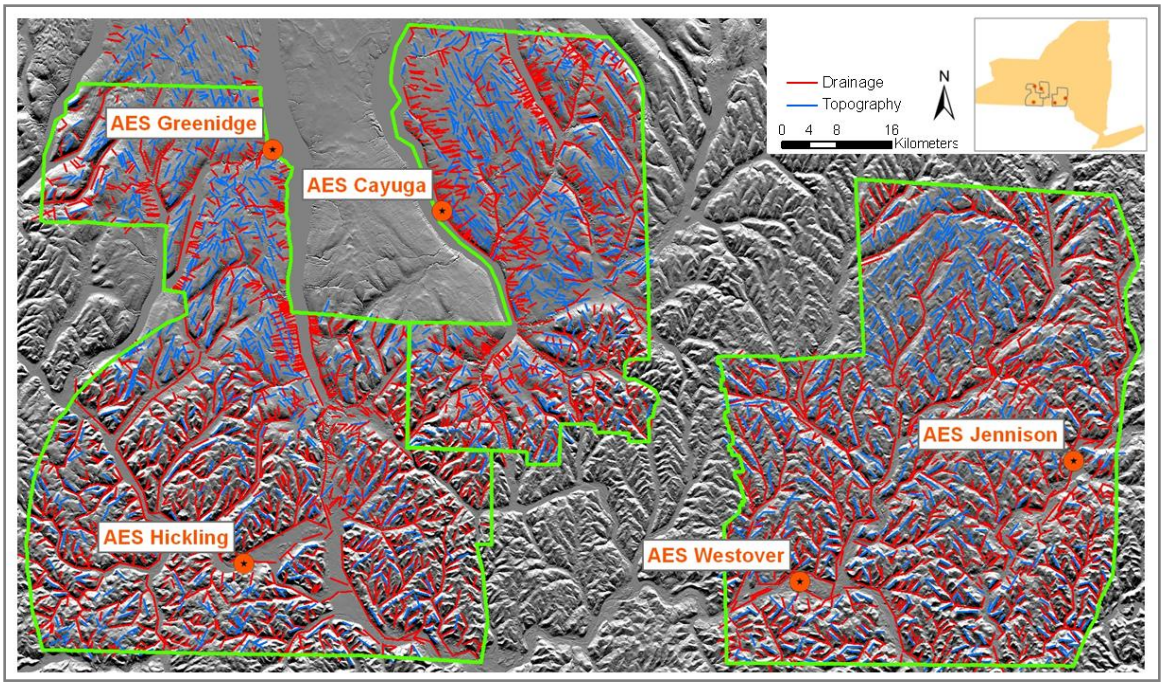

Figure 6.4,5&6-42. Phase II – DEM shaded relief representation displaying digitized lineaments over the entire project area; sun elevation/angle is 25° and sun azimuth is 0°. From Zelazny et al. (2010) and Zelazny (2011).

The statistical lineament analysis for Phase II was conducted on the entire population of lineaments as well as on the lineaments of western, central and eastern focus areas separately. Analyzing lineaments within individual focus areas could identify any regional fault and fracture trends or changes across the project area related to the regional tectonics. Variations in relationships between lineaments and land use/cover can also be analyzed by separating the lineaments of these focus areas. Basic statistics of the lineaments (i.e. count, total, average, median and maximum length, and standard deviation of length) are shown in Table 6.4,5&6-4. RockWorks (RockWare Inc.) software was used to create the rose diagrams for the entire project area, as well as the western, central and eastern focus areas. Each rose diagram was created with petals of 10° and based on total count (Figure 6.4,5&6-43 and Table 6.4,5&6-5).

	Total Count	Total Length (m)	Average Length (m)	Median Length (m)	Maximum Length (m)	Standard Deviation
Project Area						
ASTER Principal Component Composite	7,113	12,957,610	1,822	1,581	9,597	834
Shaded Relief DEM with sun azimuth (0°)	5,025	8,299,260	1,652	1,418	13,206	760
Western Focus Area						
ASTER Principal Component Composite	3,246	5,615,555	1,730	1,494	9,597	789
Shaded Relief DEM with sun azimuth (0°)	2,049	3,327,423	1,624	1,393	13,206	786
Central Focus Area						
ASTER Principal Component Composite	1,715	3,024,483	1,763	1,529	7,719	791
Shaded Relief DEM with sun azimuth (0°)	1,334	2,071,999	1,553	1,350	7,586	656
Eastern Focus Area						
ASTER Principal Component Composite	2,168	4,357,595	2,010	1,783	8,190	902
Shaded Relief DEM with sun azimuth (0°)	1,652	2,921,826	1,769	1,523	8,961	790

Table 6.4,5&6-4. Phase II - Length statistics of lineaments digitized from ASTER imagery and shaded relief DEM. (From Zelazny, 2011)

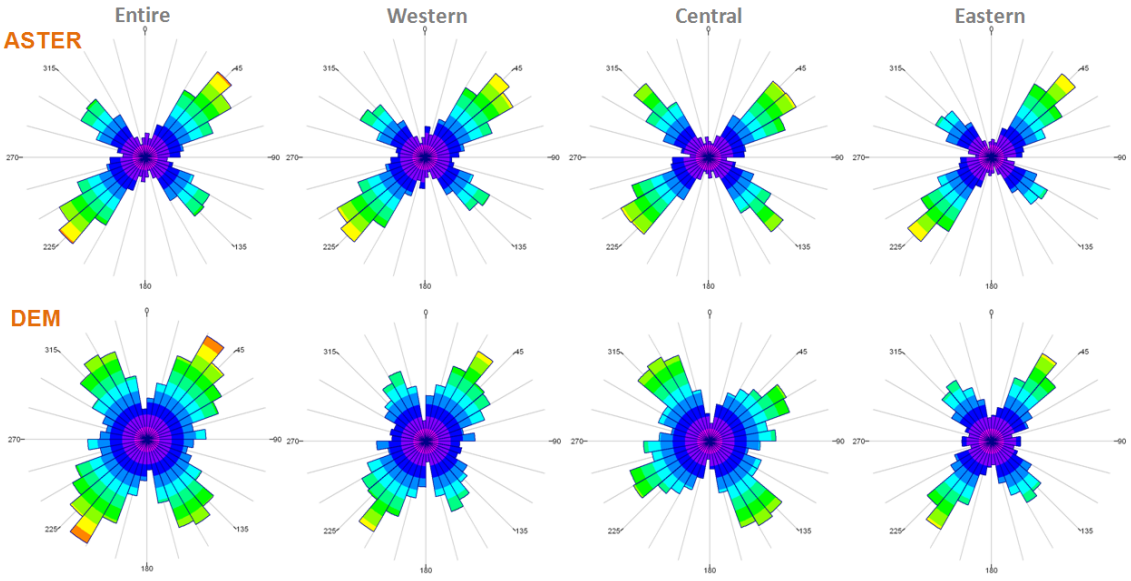

Figure 6.4,5&6-43. Phase II - Rose diagrams of lineament directions digitized from ASTER imagery and shaded relief DEMs. See Table 6.4,5&6-4 for total lineament counts. From Zelazny (2011).

	Primary Trend	Secondary Trend	Max Bin Population	Max Bin Percent
Project Area				
ASTER Principal Component Composite	NE (45°)	NW (310°)	919	6.45%
Shaded Relief DEM with sun azimuth (0°)	NNE to NE (35°)	NW to NNW (330°)	488	4.79%
Western Focus Area				
ASTER Principal Component Composite	NE (45°)	NW (305°)	404	6.21%
Shaded Relief DEM with sun azimuth (0°)	NNE to NE (35°)	NNW (330°)	212	5.15%
Central Focus Area				
ASTER Principal Component Composite	NE (50°)	NW (315°)	206	6.00%
Shaded Relief DEM with sun azimuth (0°)	NW (325°)	NE to ENE (60°)	119	4.44%
Eastern Focus Area				
ASTER Principal Component Composite	NE (45°)	NW (305°)	313	7.21%
Shaded Relief DEM with sun azimuth (0°)	NNE to NE (30°)	NW to NNW (325°)	207	6.07%

Table 6.4,5&6-5. Phase II – Primary and secondary orientation trends of lineaments digitized from ASTER imagery and shaded relief DEMs. From Zelazny (2011).

Phase III – Detailed study around Cayuga Power Plant (Subtasks 6.4 and 6.5). Phase III focused on a smaller area around the AES Cayuga power plant because this plant was favored for CO_2 sequestration based on preliminary data from other group members of this multidisciplinary project. The Phase III study encompassed an area of 225 km^2 with the AES Cayuga power plant centered latitudinally (Cayuga Subset – see Figure 6.4,5&6-3 for location). A scale of 1:25,000 was selected for digitizing to obtain a detailed data set with the minimum lineament length of 0.5 km. Lineaments were digitized both on the ASTER PC color composite image and on the 0° illumination angle shaded relief DEM with sun elevation angle 25° (Figures 6.4,5&6-44 and 6.4,5&6-45). Statistics and rose diagrams of the lineaments from the Cayuga Subset are shown in Tables 6.4,5&6-6 and 6.4,5&6-7 and in Figure 6.4,5&6-46.

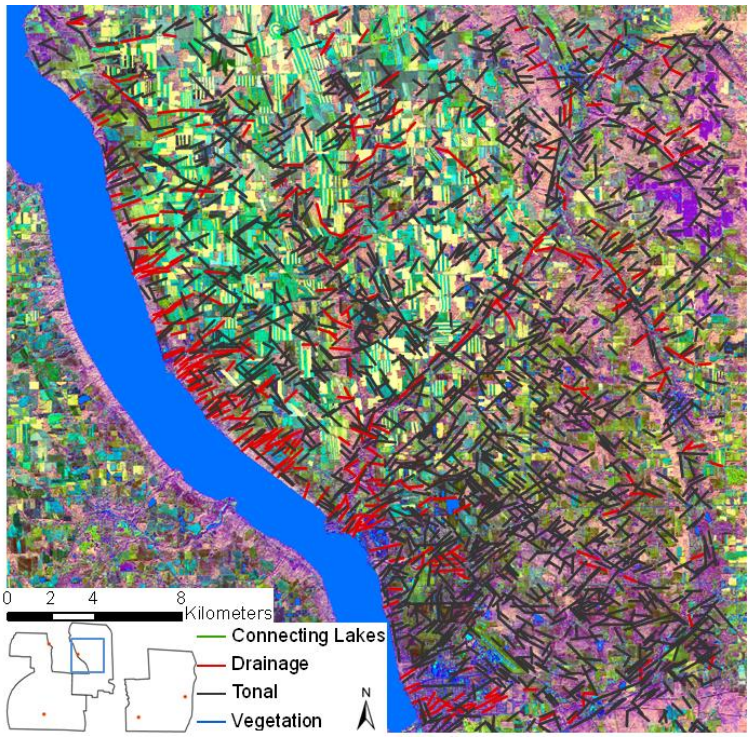

Figure 6.4,5&6-44. Phase III – ASTER principal component color composites with digitized lineaments in the Cayuga Subset; Principal Component composite R(PC2), G(PC1), B(PC3). From Zelazny (2011).

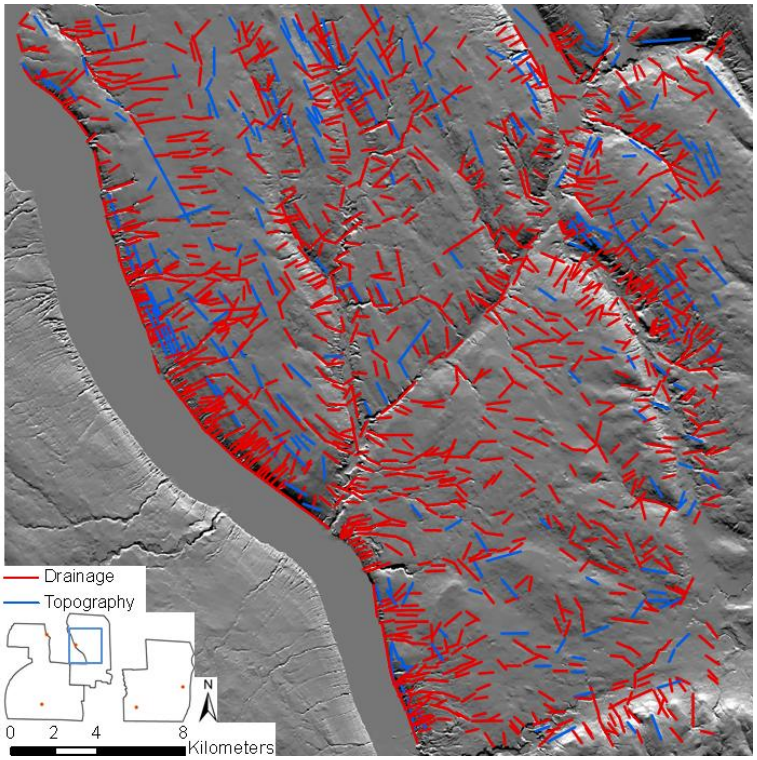

Figure 6.4,5&6-45. Phase III – Shaded relief DEM with digitized lineaments for Cayuga subset; 25° sun elevation and 0° sun illumination direction. From Zelazny (2011).

	Total Count	Total Length (m)	Average Length m)	Median Length (m)	Maximum Length (m)	Standard Deviation
Cayuga Subset						
ASTER Principal Component Composite	2,048	1,498,832	719	650	3,524	246
Shaded Relief DEM with sun azimuth (0°)	1,398	1,018,360	728	640	4,042	275

Table 5.6. Phase III - Length statistics of lineaments digitized from ASTER imagery and shaded relief DEM, Cayuga subset. From Zelazny (2011).

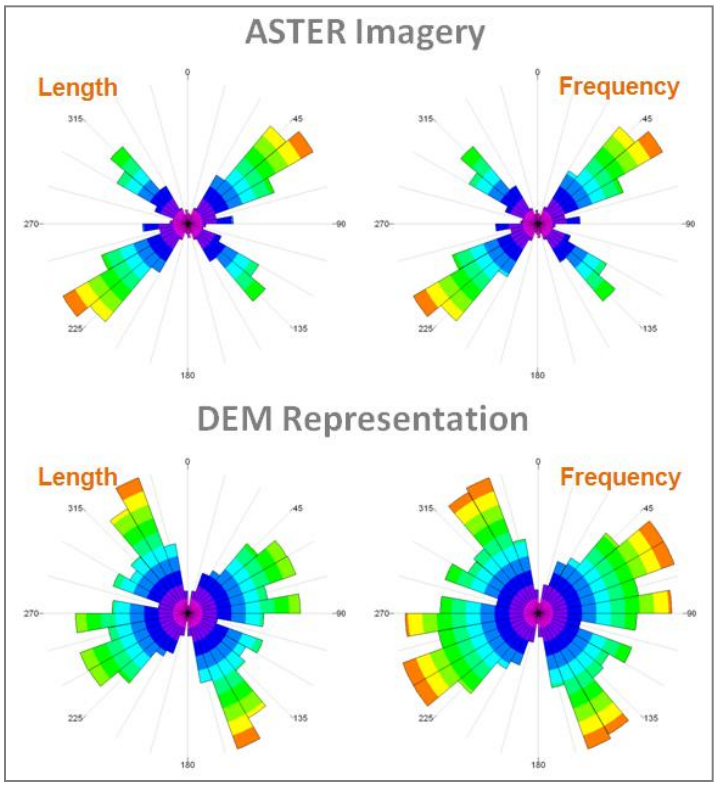

Figure 6.4,5&6-46. Phase III - rose diagrams showing orientation distribution of lineaments digitized from ASTER imagery and shaded relief DEM, Cayuga subset. See Table 6.4,5&6-6 for total counts. From Zelazny (2011).

	Primary Trend	Secondary rend	Max Bin Population	Max Bin Percent
Cayuga Subset				
ASTER Principal Component Composite	NE (55°)	NW (315°)	348	8.35%
Shaded Relief DEM with sun azimuth (0°)	NNW (340°)	NE to ENE (60°)	128	4.58%

Table 6.4,5&6-7. Phase III - Primary trends identified with statistics and secondary trends of ASTER and shaded relief DEMs digitized lineaments for the Cayuga subset. From Zelazny (2011).

Additional Analyses: 1) Histograms (Subtasks 6.4 and 6.5). In order to gain a better understanding of the distribution of the digitized lineaments, histograms were made for each dataset based on lineament orientation. Five histograms were made, including the ASTER and DEM lineaments for the entire project area, the ASTER and DEM lineaments for the Cayuga power plant subset datasets, and a histogram with all datasets combined (Figures 6.4,5&6-47 to Figure 6.4,5&6-51). In order to define orientation groups that could be used for all datasets, the histogram with all lineaments (project area and Cayuga subset) was used. After reviewing the modes in the combined histogram, it was determined that there was a total of eight groups, which include WNW (285 – 301), NW (301 - 335), NNW (335 – 350), NS (350 – 11), NNE (11 - 21), NE (21 – 59), ENE (59 – 79) and EW (79 – 105) (Figure 6.4,5&6-52). Each of these groups were separated by noticeable breaks in the histogram distribution; the breaks occur approximately at 285°, 301°, 335°, 350°, 11°, 21°, 59° and 79°.

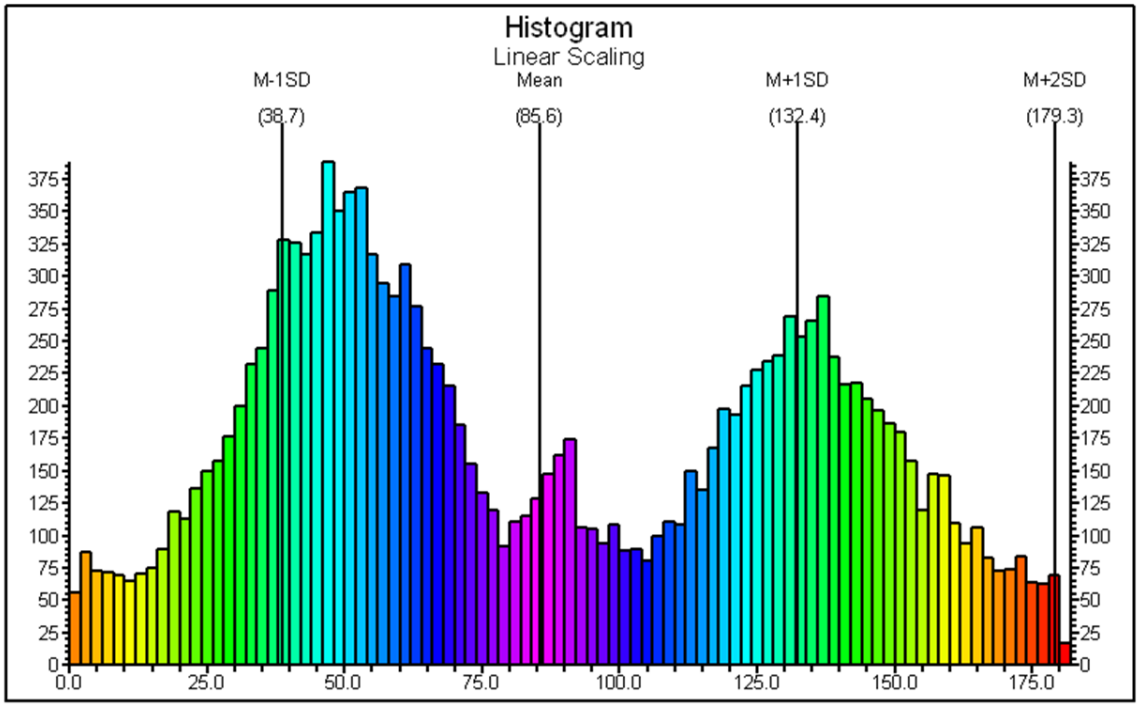

Figure 6.4,5&6-47. Histograms of all digitized lineaments (ASTER and DEM) for the entire project area and Cayuga subset. Horizontal axis is direction (°), bin size of 2°, vertical axis is lineament count. From Zelazny et al. (2010) and Zelazny (2011).

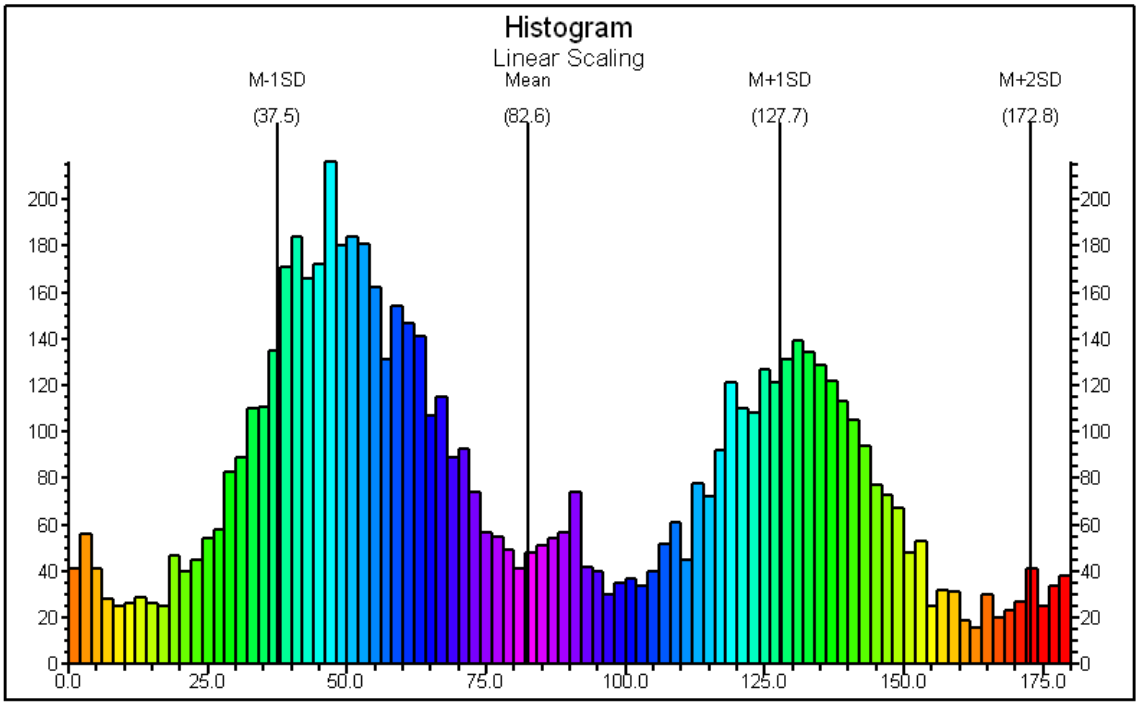

Figure 6.4,5&6-48. Histogram of ASTER digitized lineaments for the project area with a bin size of 2°. From Zelazny et al. (2010) and Zelazny (2011).

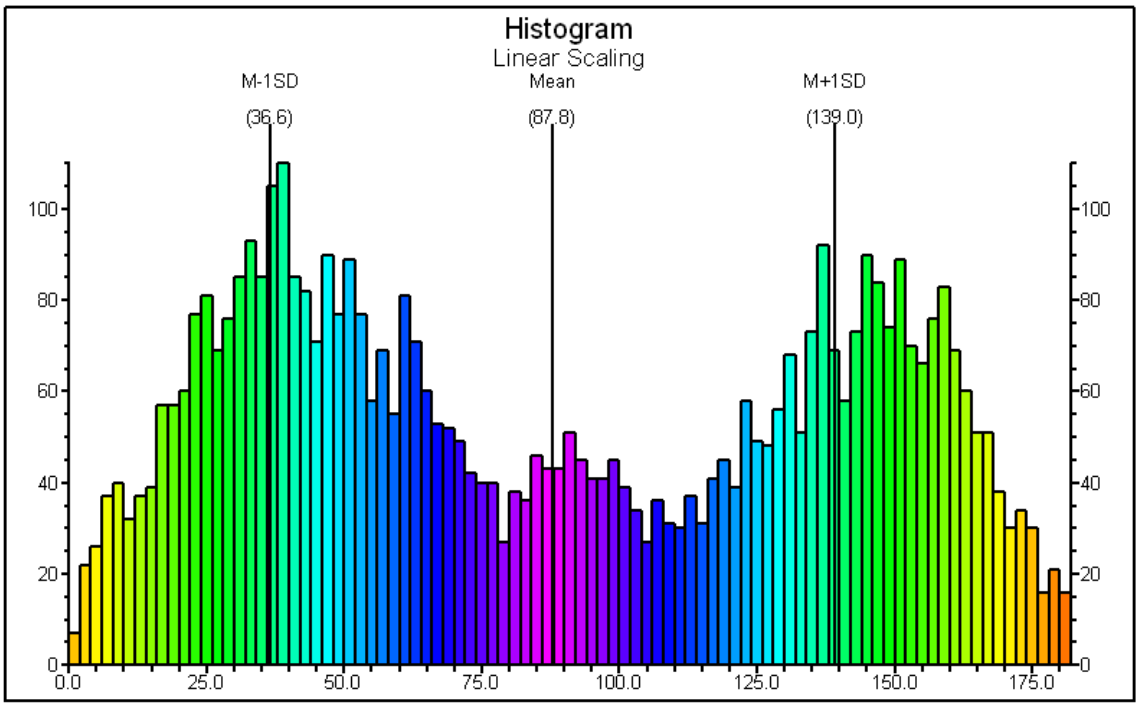

Figure 6.4,5&6-49. Histogram of DEM digitized lineaments for the Project Area with a bin size of 2°. From Zelazny et al. (2010) and Zelazny (2011).

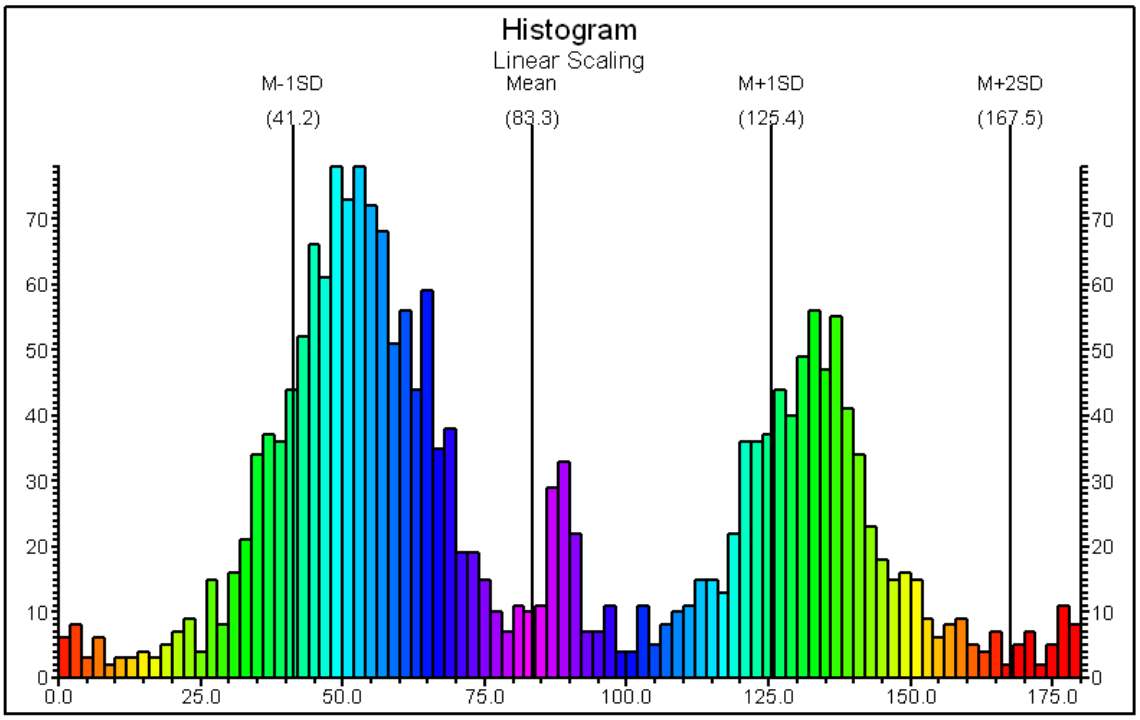

Figure 6.4,5&6-50. Histogram of ASTER digitized lineaments for the Cayuga Subset with bin size of 2°. From Zelazny et al. (2010) and Zelazny (2011).

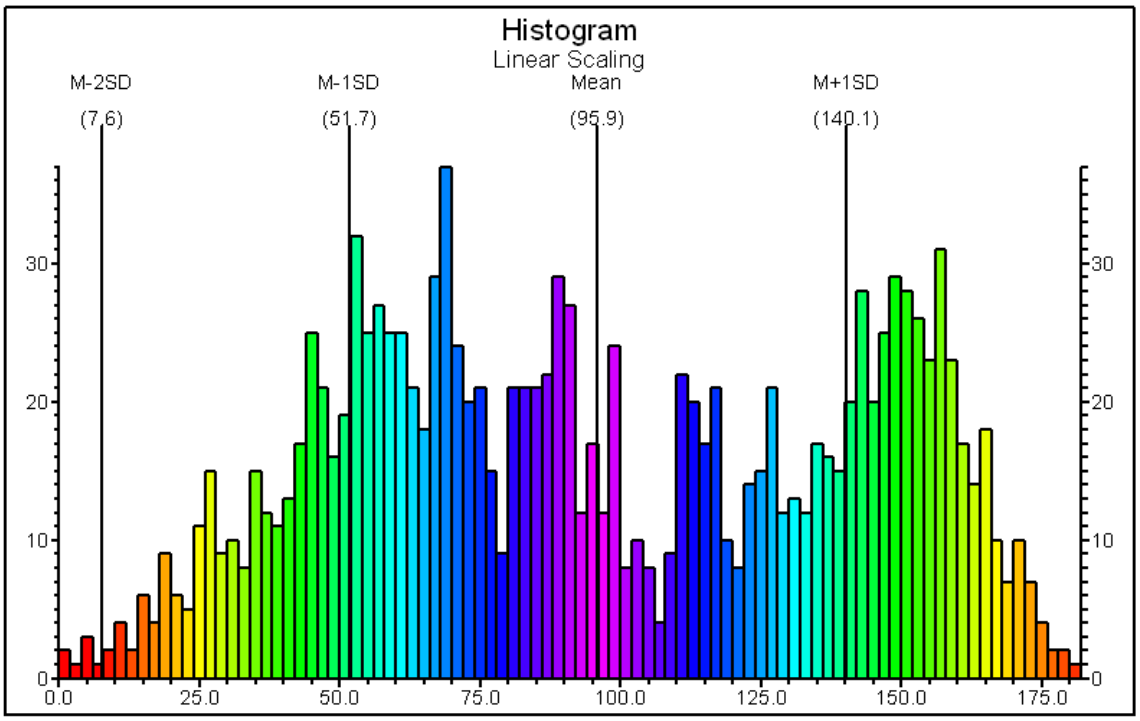

Figure 6.4,5&6-51. Histogram of DEM digitized lineaments for the Cayuga Subset with bin size of 2°. From Zelazny et al. (2010) and Zelazny (2011).

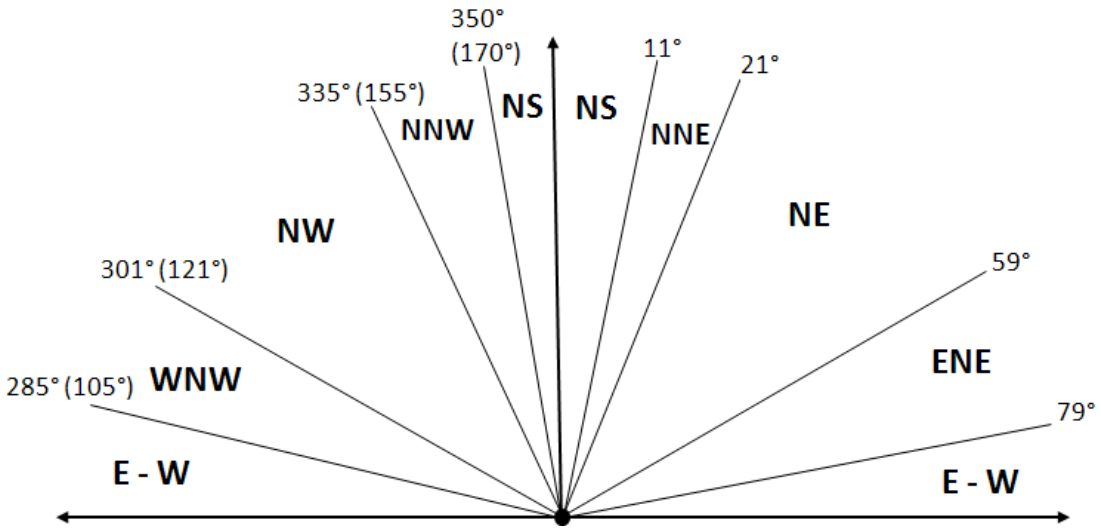

Figure 6.4,5&6-52. Azimuth distribution of orientation groups for all digitized lineament orientations. From Zelazny et al. (2010) and Zelazny (2011).

Additional Analyses: 2) Rose Diagrams (Subtasks 6.4 and 6.5). To determine possible changes in trends of the lineaments digitized from the ASTER images across the region, a detailed rose diagram analysis was performed. The result was 13 rose diagrams for the Cayuga subset (Figure 6.4,5&6-53b) and 55 rose diagrams for the entire project area (Figure 6.4,5&6-54), which were overlaid on a grey scale Landsat image mosaic (Figure 6.4,5&6-54b).

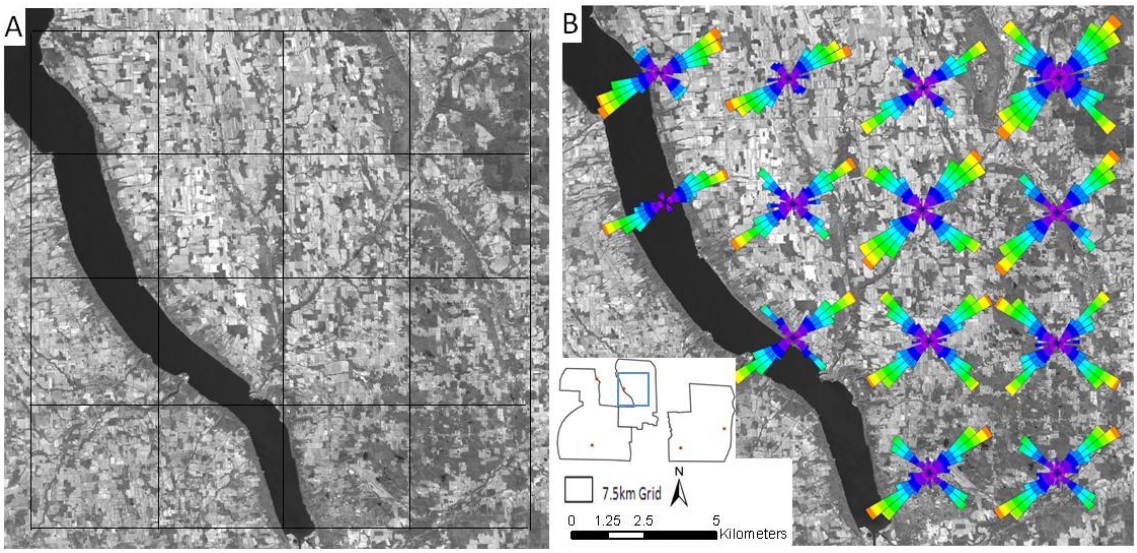

Figure 6.4,5&6-53. Detailed rose diagram analysis of ASTER lineaments, Phase III, Cayuga subset. Grid cell size is 7.5 km by 7.5 km. From Zelazny et al. (2010) and Zelazny (2011).

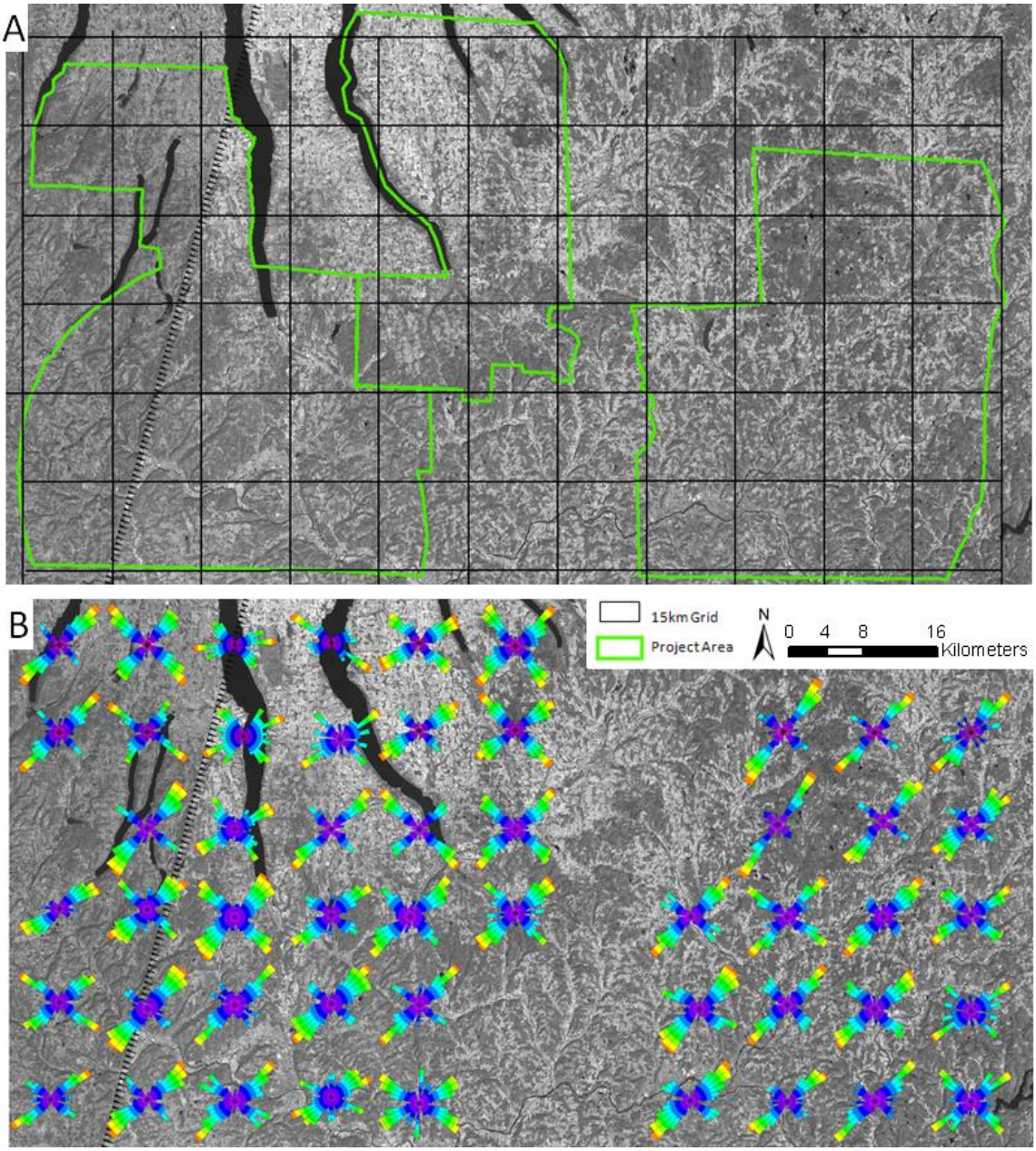

Figure 6.4,5&6-54. Detailed rose diagram analysis of ASTER lineaments, Phase II, for the entire project area. From Zelazny et al. (2010) and Zelazny (2011).

For the Cayuga subset with lineaments digitized at a scale of 1:25,000, the primary trend is NE (21° to 59°) and the secondary trend is NW (301° to 335°). Although there is not a dramatic difference in rose petal orientations across the subset, subtle variations do occur. The secondary trend of NW is almost as strong as the primary trend in the eastern part of the Cayuga subset, with one rose diagram having a stronger NW than NE trend. Weak EW trends are observed in the eastern part of the Cayuga subset and an ENE trend

occurs along the eastern shore of Seneca Lake. This ENE trend reflects the ENE-striking fractures exposed in the Geneseo black shale that outcrops in this region (e.g., Jacobi, 2007).

In the full project area where lineaments were digitized at a scale of 1:125,000, the primary trend is also approximately NE (21° - 59°) with some variations to NNE (11° - 21°) and ENE (59° - 79°). The secondary trend is approximately NW (301° - 335°) with some variations to NNW (335° - 350°) and WNW (285° - 301°). Only small changes in the rose diagrams across the project area are easily discerned in the primary trends. However, in the southeastern part of the western focus area seven rose diagrams display a third and much smaller trend of NS (350° - 360° and 0° - 11°). In this same area, the primary northeasterly trend is oriented more ENE than in regions to the north. Also, in the northeastern part of the western focus area, relatively strongly developed E-W trends are apparent. Such trends are consistent with the EW trends of Alleghanian salt-cored folds in the same area (e.g., Wedel, 1932; Jacobi, 2007). The primary trend of rose diagrams in the eastern focus area was uniform with little variation from NE (45°), but the secondary trend varied greatly with trends ranging from NW (300°) to NW (335°). A slight clockwise rotation of the prominent lineament orientations occurs from the western part of the project area to the eastern part.

Additional Analyses: 3) Lineament Density Maps (Subtasks 6.4, 6.5, and 6.6). Density maps were compiled from the all the lineaments extracted from ASTER imagery and from the shaded relief DEM for the entire project area (Figures 6.4,5&6-55 to 6.4,5&6-60) and the Cayuga power plant subset (Figures 6.4,5&6-61 to 6.4,5&6-64). Filtered density maps (or "density map of specific orientation") were also computed for lineaments within the specific orientation groups that are defined in Figure 6.4,5&6-52 (Figures Figure 6.4,5&6-65 to Figure 6.4,5&6-96).

Various lineament density trends were identified on both the ASTER and DEM density maps; these are along color changes of high (oranges and reds) or low (blues and greens) lineament densities. In the project area the ASTER lineament density trends identified includes NE, NS, NNW, ENE and NW and the DEM lineament density map revealed NE, NW, NNW, NS, and NNE lineament density trends (Table 6.4,5&6-8 and Figures 6.4,5&6-65 to 6.4,5&6-80). In the Cayuga Subset the ASTER lineament density trends identified includes NE and NS. The DEM lineament density map revealed NS, NW, NNW and NE lineament density trends (Table 6.4,5&6-8 and Figures 6.4,5&6-81 to 6.4,5&6-96). The filtered lineament density maps provided the most insight into the spatial distribution of the lineaments based on density trends and clustering of the lineaments.

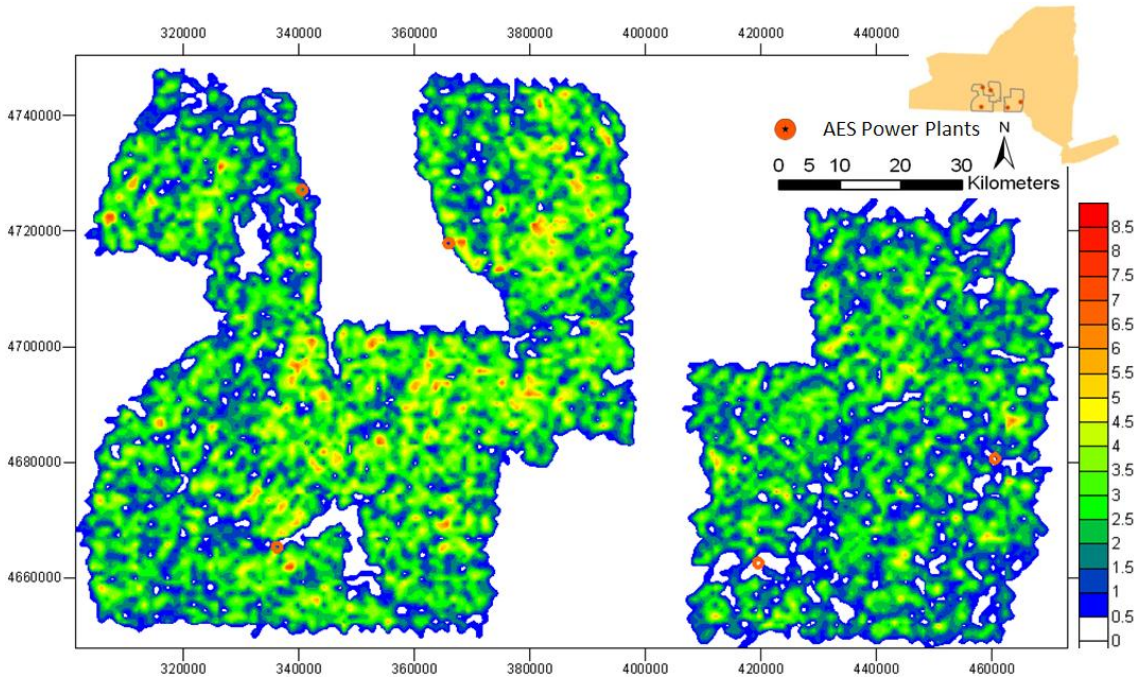

Figure 6.4,5&6-55. Lineament density map from all ASTER lineaments; colors show lineament density in counts per 0.333 mi^2 (0.862 km^2). Coordinates are given in meter in UTM (N18) projection system. From Zelazny (2011).

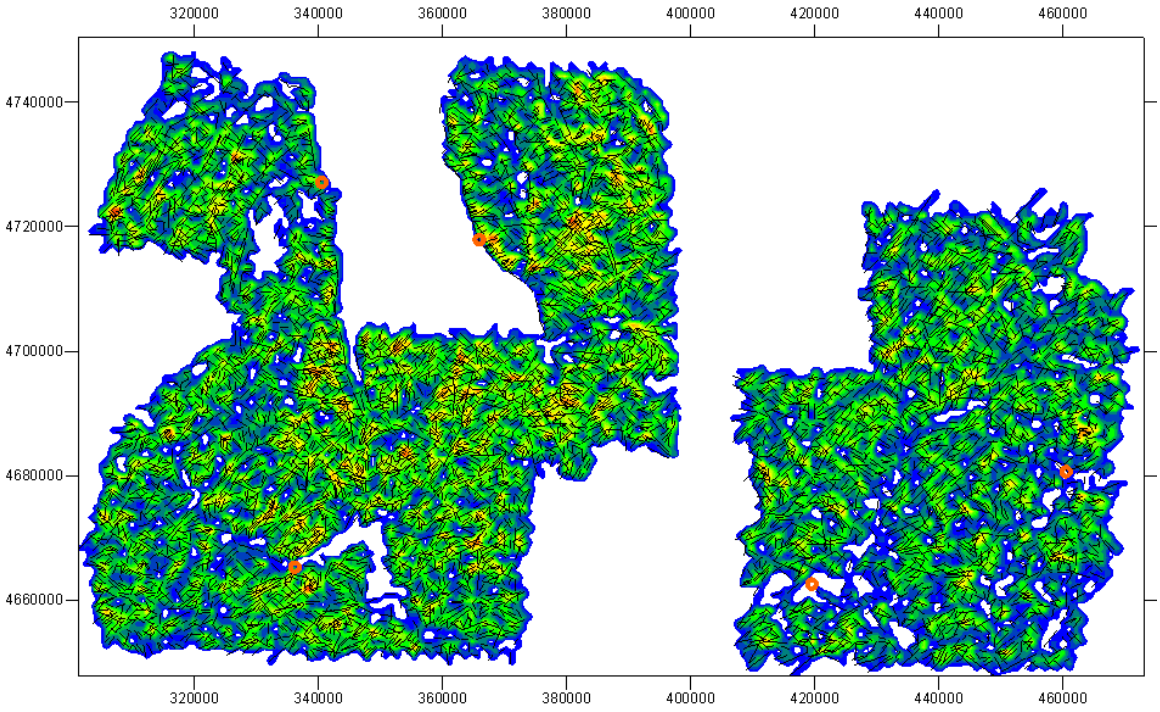

Figure 6.4,5&6-56. Density map for ASTER lineaments of all orientations in the project area, with lineaments shown. Colors as in Figure 6.4,5&6-57. From Zelazny (2011).

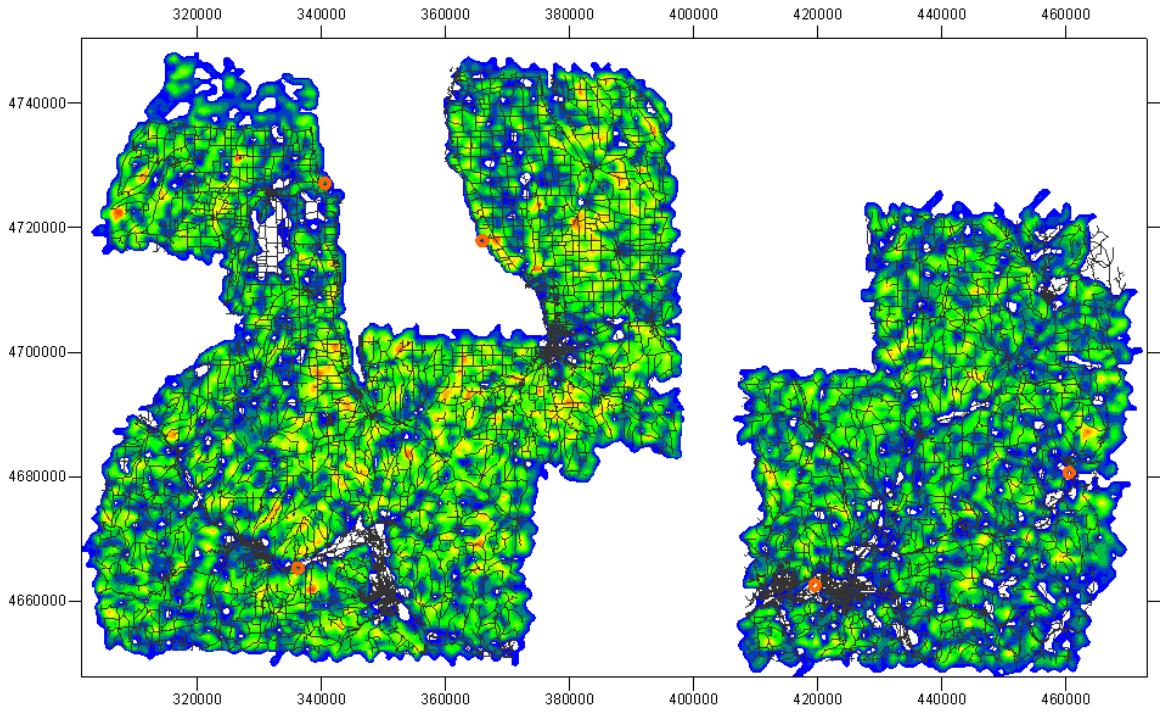

Figure 6.4,5&6-57. Density Map for ASTER lineaments of all orientations in the project area, with roads shown. Colors as in Figure 6.4,5&6-57. From Zelazny (2011).

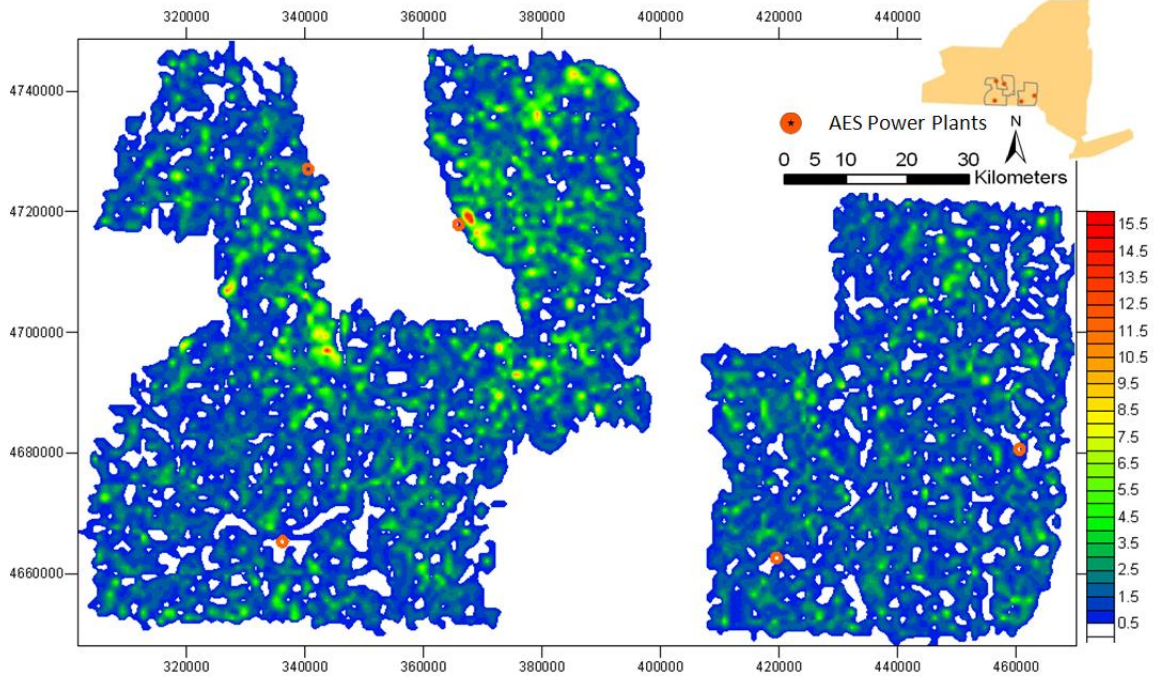

Figure: 6.4,5&6-58. Lineament density map from all DEM lineaments; colors show lineament density in counts per 0.333 mi^2 (0.862 km^2). Coordinates are given in meter in UTM (N18) projection system. From Zelazny (2011).

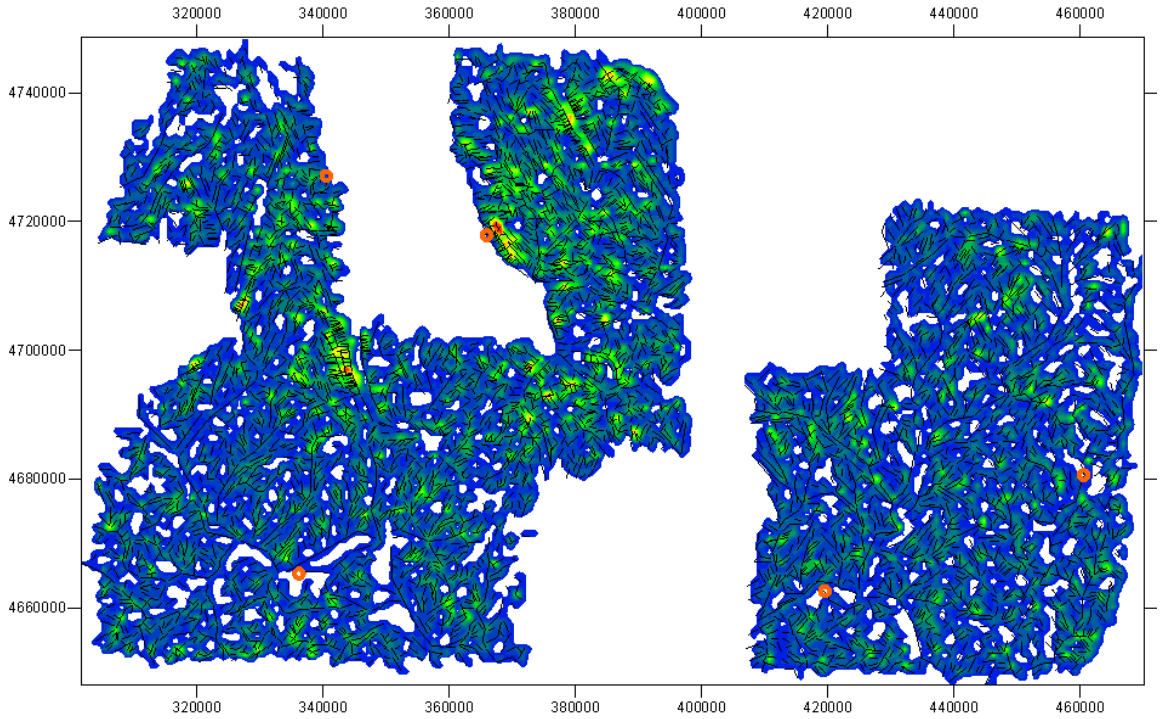

Figure 6.4,5&6-59. Density map for DEM lineaments of all orientations in the project area, shown with lineaments. Colors as in Figure 6.4,5&6-58. From Zelazny (2011).

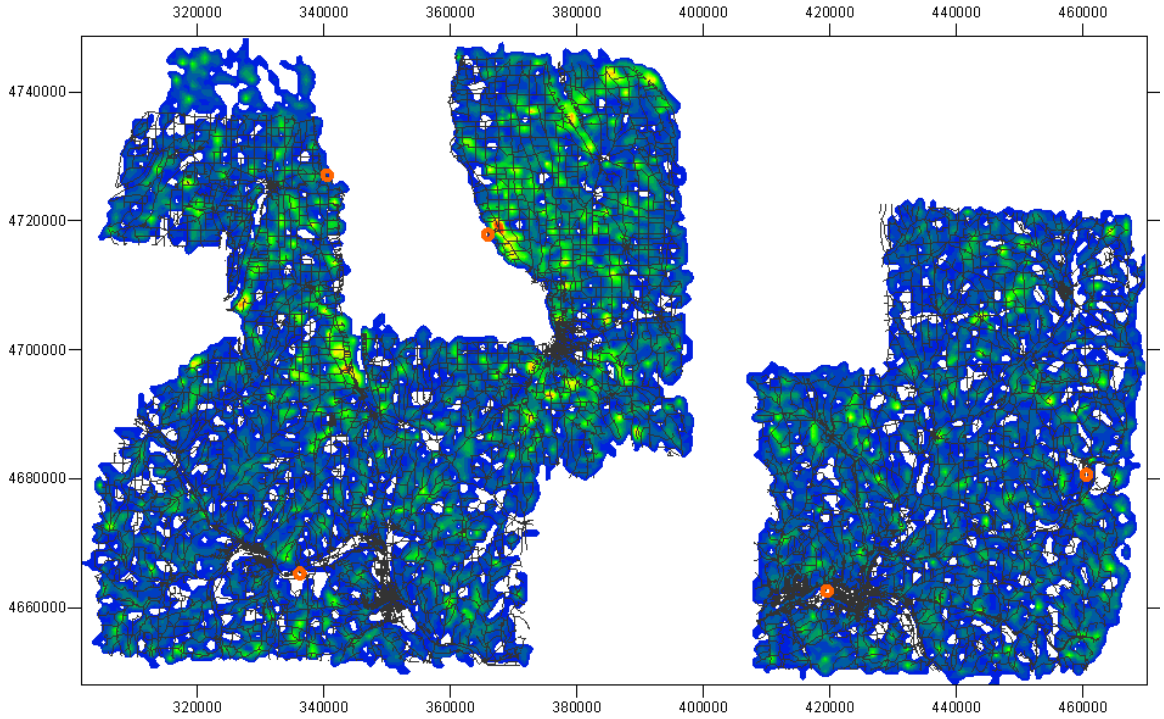

Figure 6.4,5&6-60. Density map for DEM lineaments of all orientations in the project area, shown with roads. Colors as in Figure 6.4,5&6-58. From Zelazny (2011).

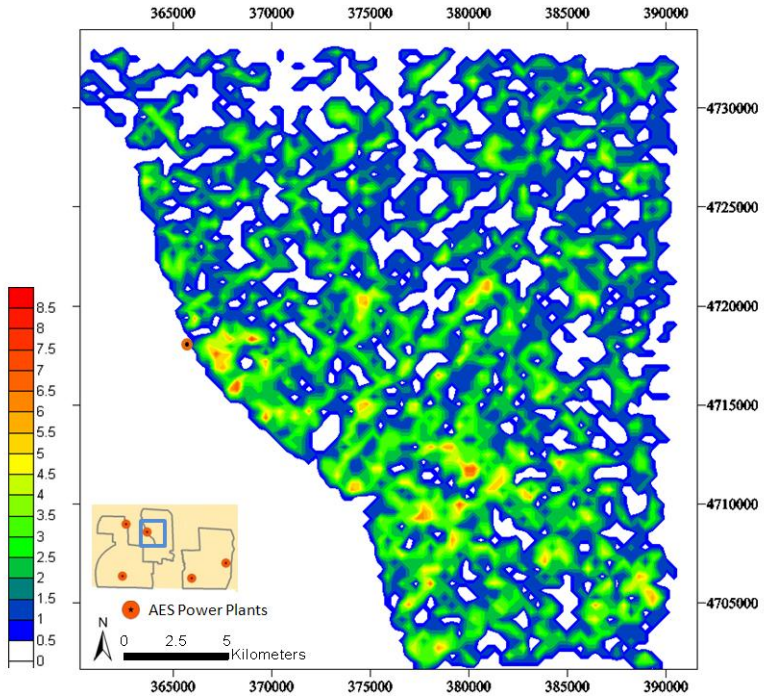

Figure 6.4,5&6-61. Lineament density map from all ASTER lineaments in the Phase III, Cayuga Subset. Colors show lineament density in counts per 0.05 mi^2 (.129 km^2). Coordinates are given in meters in UTM (N18) projection system. From Zelazny (2011).

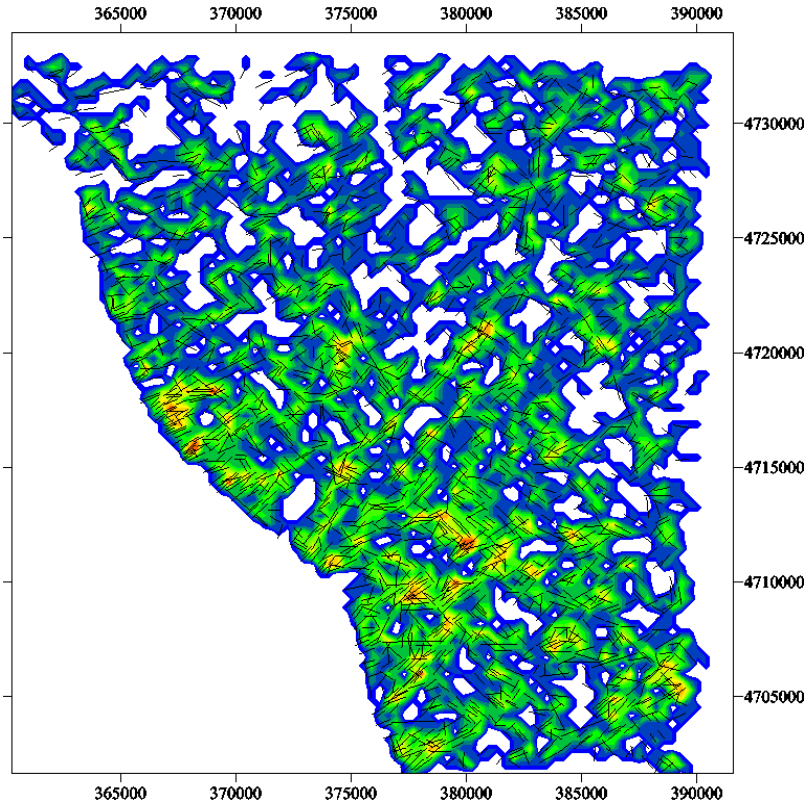

Figure 6.4,5&6-62. Density Map for ASTER lineaments of all orientation in the Cayuga subset, shown with lineaments. Colors and map location same as in Figure 6.4,5&6-61. From Zelazny (2011).

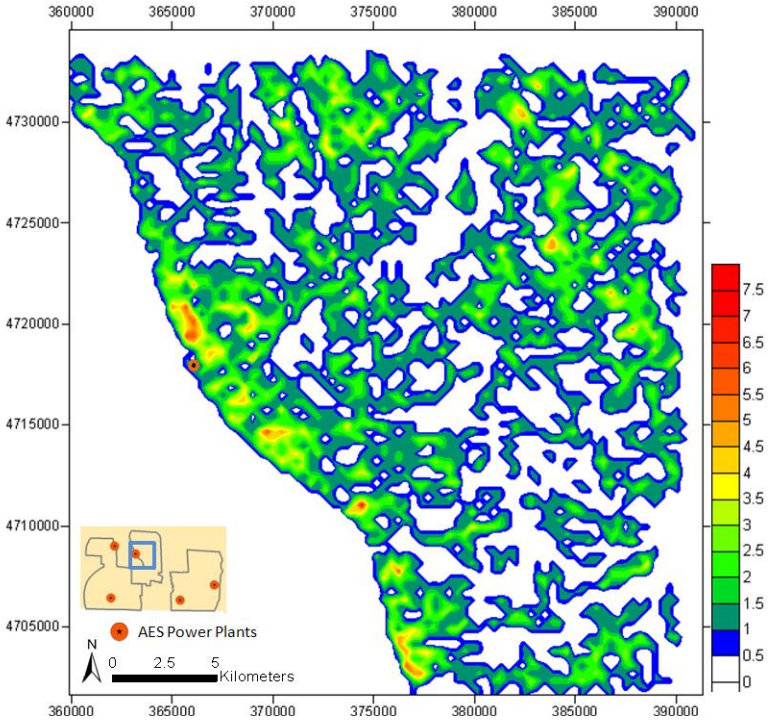

Figure 6.4,5&6-63. Lineament density map from all DEM lineaments in the Phase III, Cayuga Subset. Colors show lineament density in counts per 0.05 mi^2 (.129 km^2). Coordinates are given in meters in UTM (N18) projection system. From Zelazny (2011).

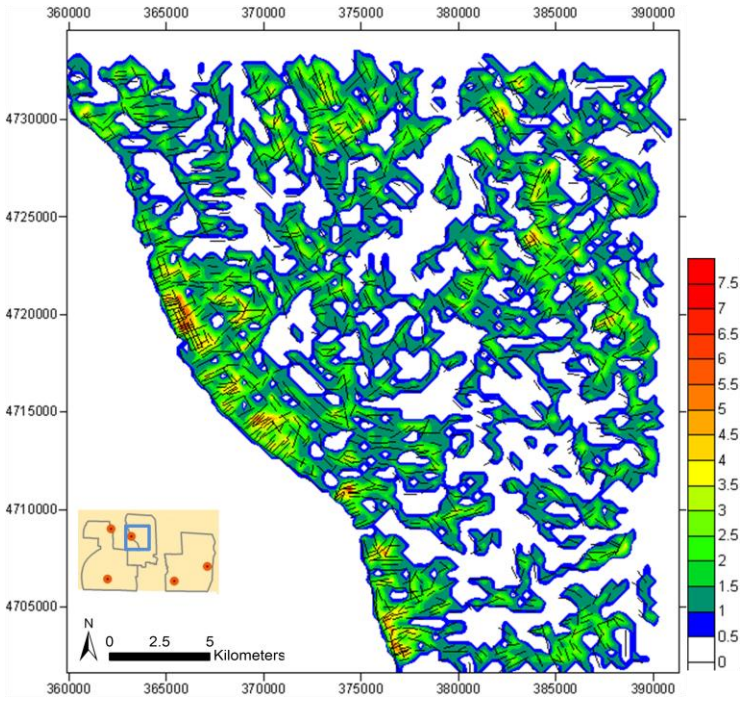

Figure 6.4,5&6-64. Density map for DEM lineaments of all orientations in the Cayuga subset, shown with lineaments. From Zelazny (2011).

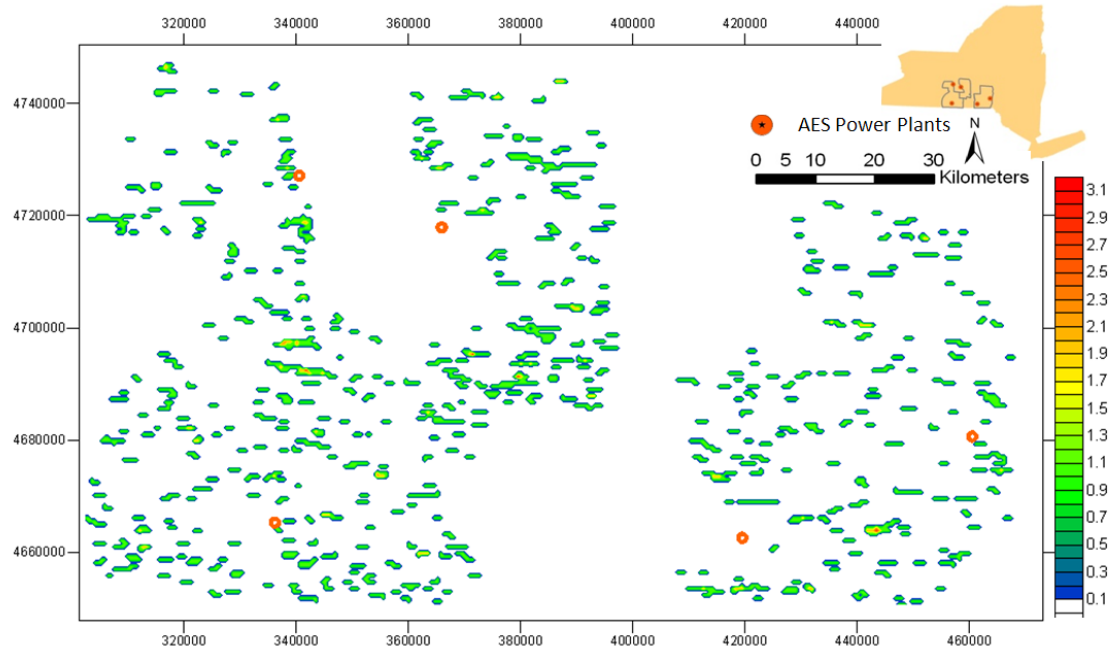

Figure 6.4,5&6-65. Lineament density map from EW-trending ASTER lineaments for the entire project area. Colors show lineament density in counts per 0.333 mi^2 (0.862 km^2). Coordinates are given in meters in UTM (N18) projection. From Zelazny (2011).

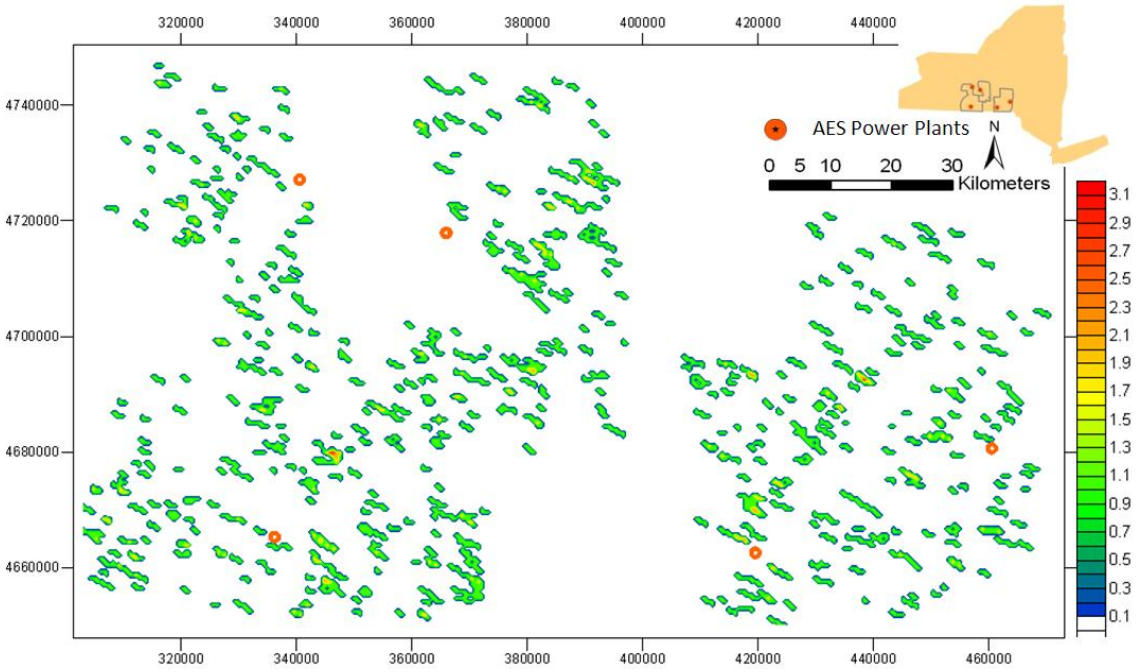

Figure 6.4,5&6-66. Lineament density map from WNW-trending ASTER lineaments for the entire project area. Colors show lineament density in counts per 0.333 mi^2 (0.862 km^2). Coordinates are given in meters in UTM (N18) projection. From Zelazny (2011).

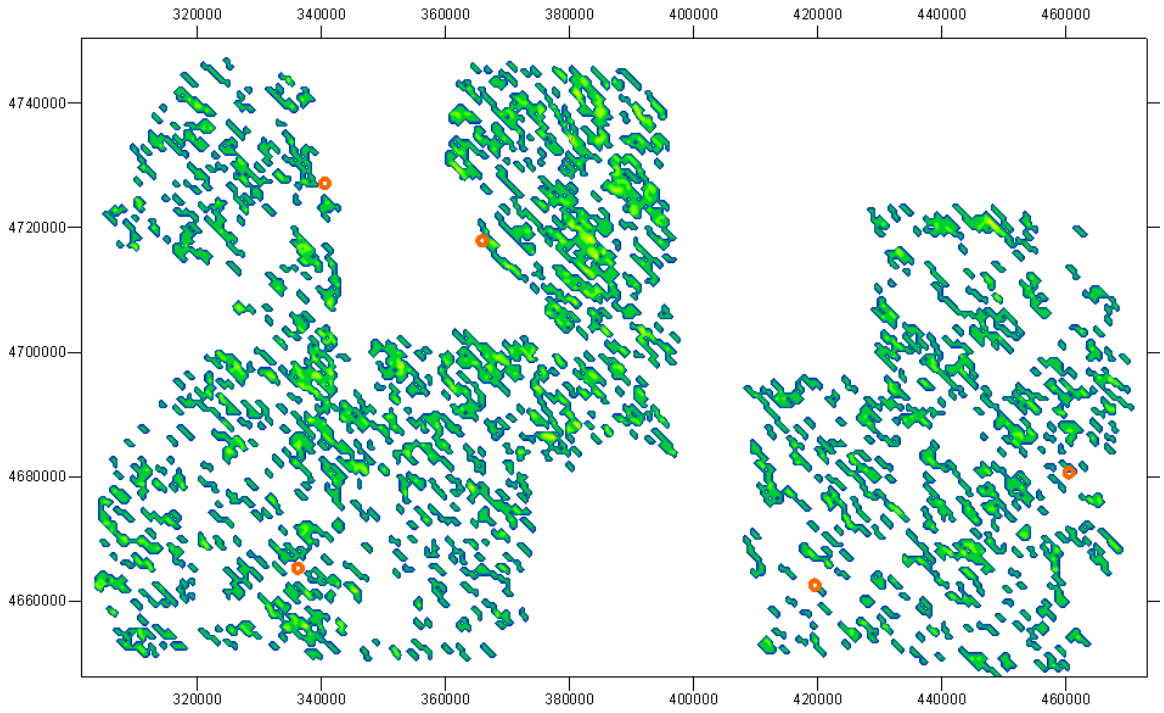

Figure 6.4,5&6-67. Lineament density map from NW-trending ASTER lineaments for the entire project area. Colors show lineament density in counts per 0.333 mi^2 (0.862 km^2). Coordinates are given in meters in UTM (N18) projection. From Zelazny (2011).

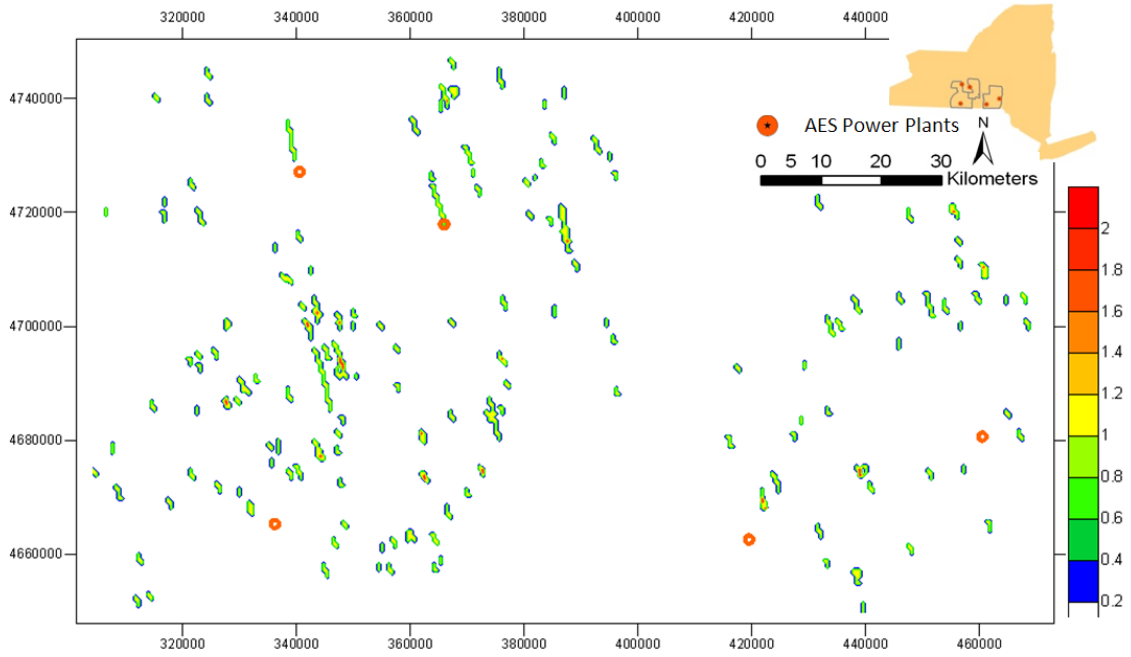

Figure 6.4,5&6-68. Lineament density map from NNW-trending ASTER lineaments for the entire project area. Colors show lineament density in counts per 0.333 mi^2 (0.862 km^2). Coordinates are given in meters in UTM (N18) projection. From Zelazny (2011).

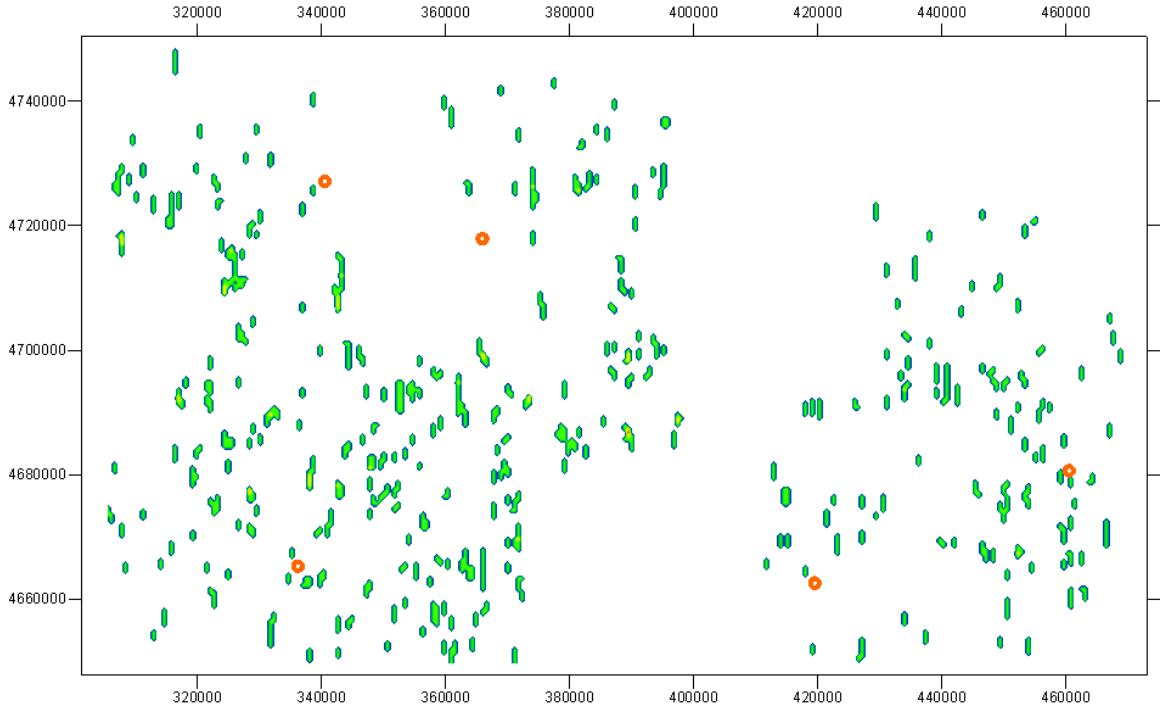

Figure 6.4,5&6-69. Lineament density map from N-trending ASTER lineaments for the entire project area. Colors show lineament density in counts per 0.333 mi^2 (0.862 km^2). Coordinates are given in meters in UTM (N18) projection. From Zelazny (2011).

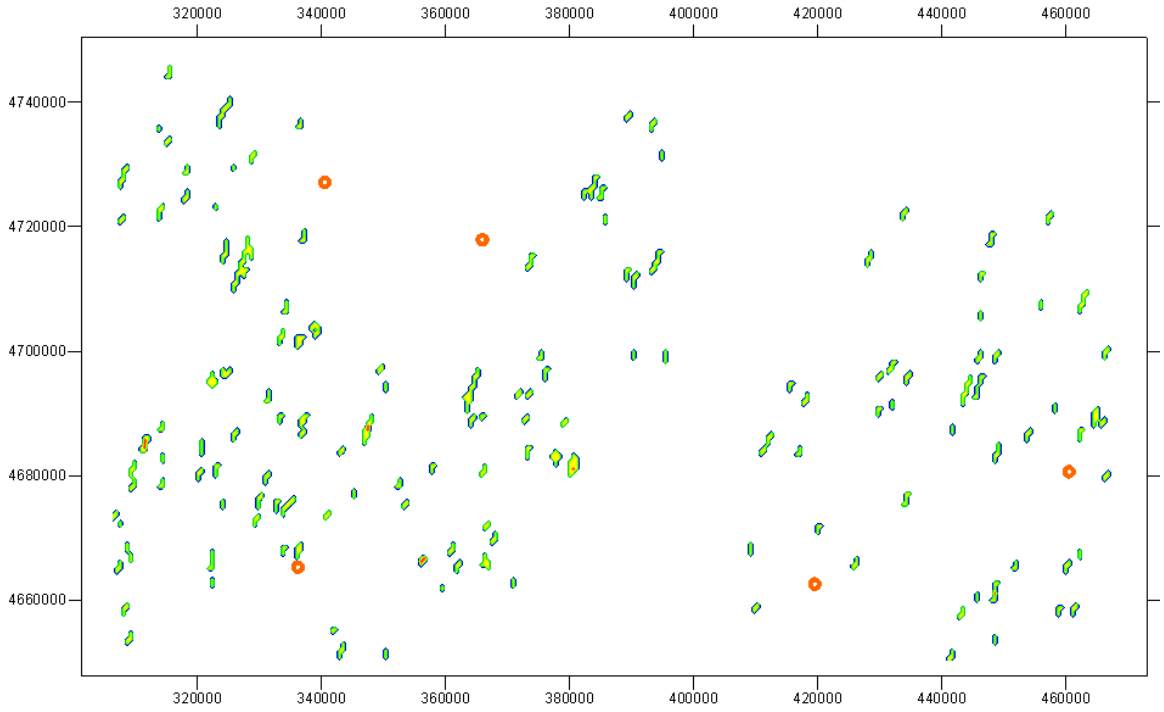

Figure 6.4,5&6-70. Lineament density map from NNE-trending ASTER lineaments for the entire project area. Colors show lineament density in counts per 0.333 mi^2 (0.862 km^2). Coordinates are given in meters in UTM (N18) projection. From Zelazny (2011).

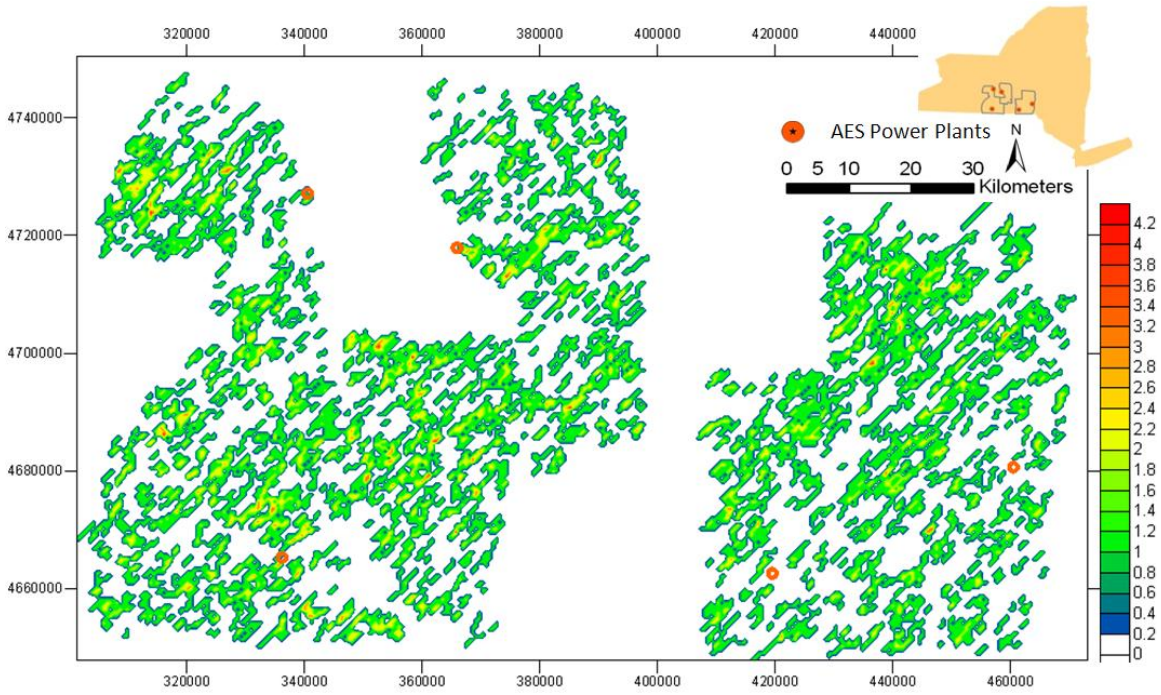

Figure 6.4,5&6-71. Lineament density map from NE-trending ASTER lineaments for the entire project area. Colors show lineament density in counts per 0.333 mi^2 (0.862 km^2). Coordinates are given in meters in UTM (N18) projection. From Zelazny (2011).

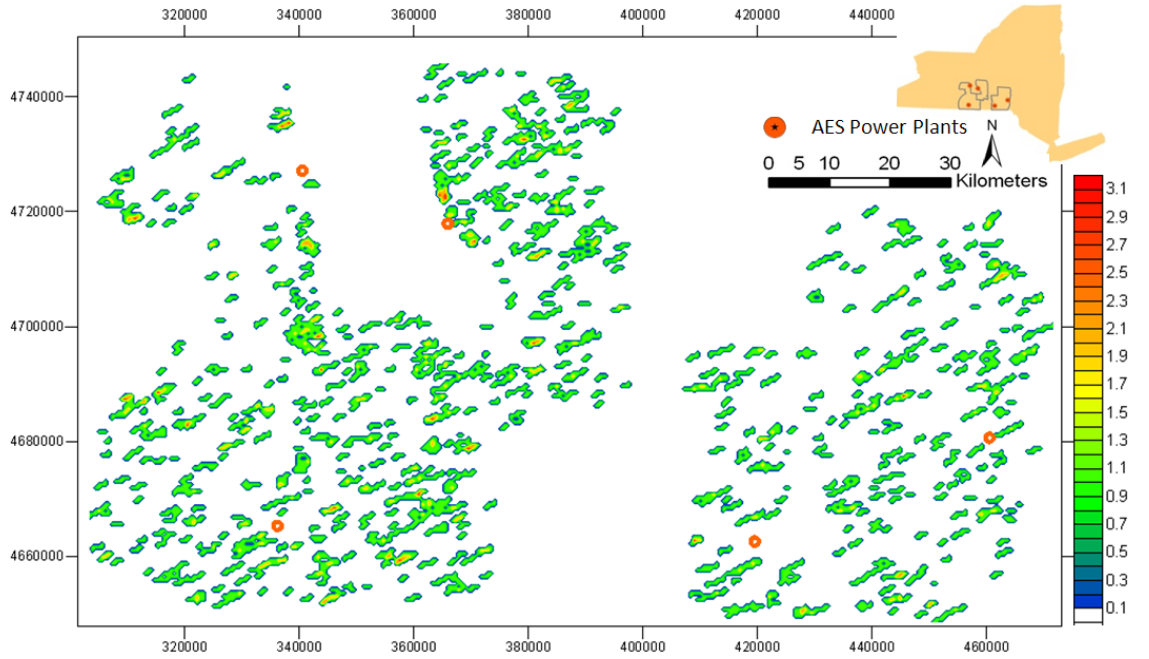

Figure 6.4,5&6-72. Lineament density map from ENE-trending ASTER lineaments for the entire project area. Colors show lineament density in counts per 0.333 mi^2 (0.862 km^2). Coordinates are given in meters in UTM (N18) projection. From Zelazny (2011).

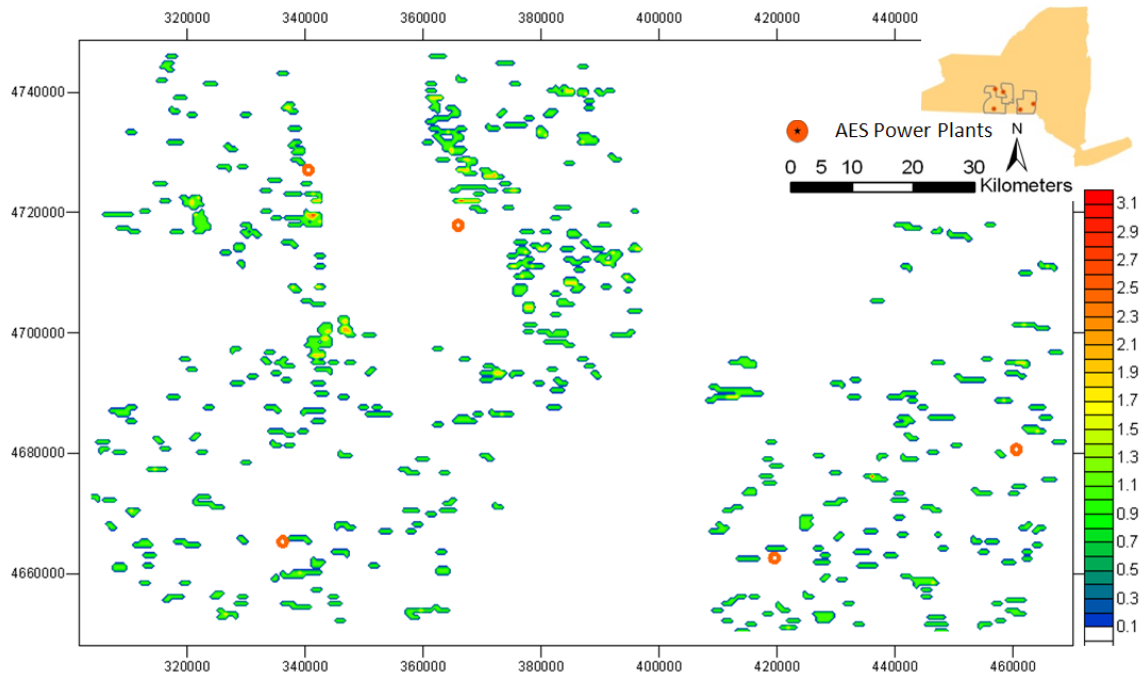

Figure 6.4,5&6-73. Lineament density map from EW-trending DEM lineaments for the entire project area. Colors show lineament density in counts per 0.333 mi^2 (0.862 km^2). Coordinates are given in meters in UTM (N18) projection. From Zelazny (2011).

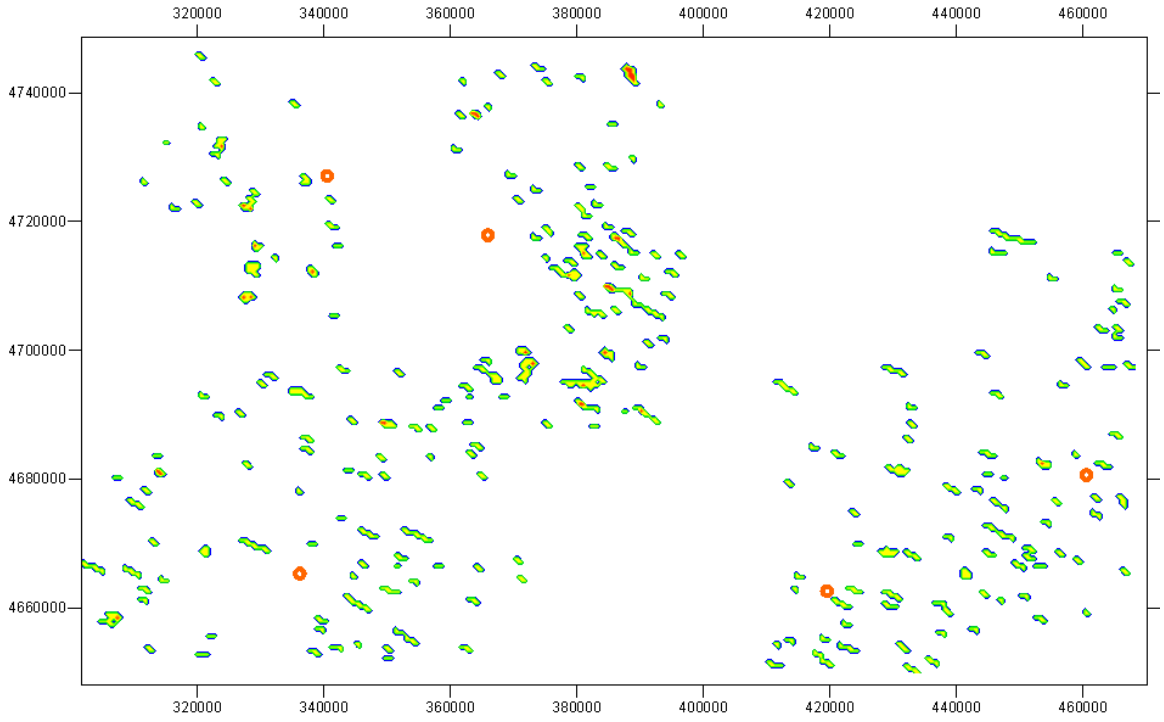

Figure 6.4,5&6-74. Lineament density map from WNW-trending DEM lineaments for the entire project area. Colors show lineament density in counts per 0.333 mi^2 (0.862 km^2). Coordinates are given in meters in UTM (N18) projection. From Zelazny (2011).

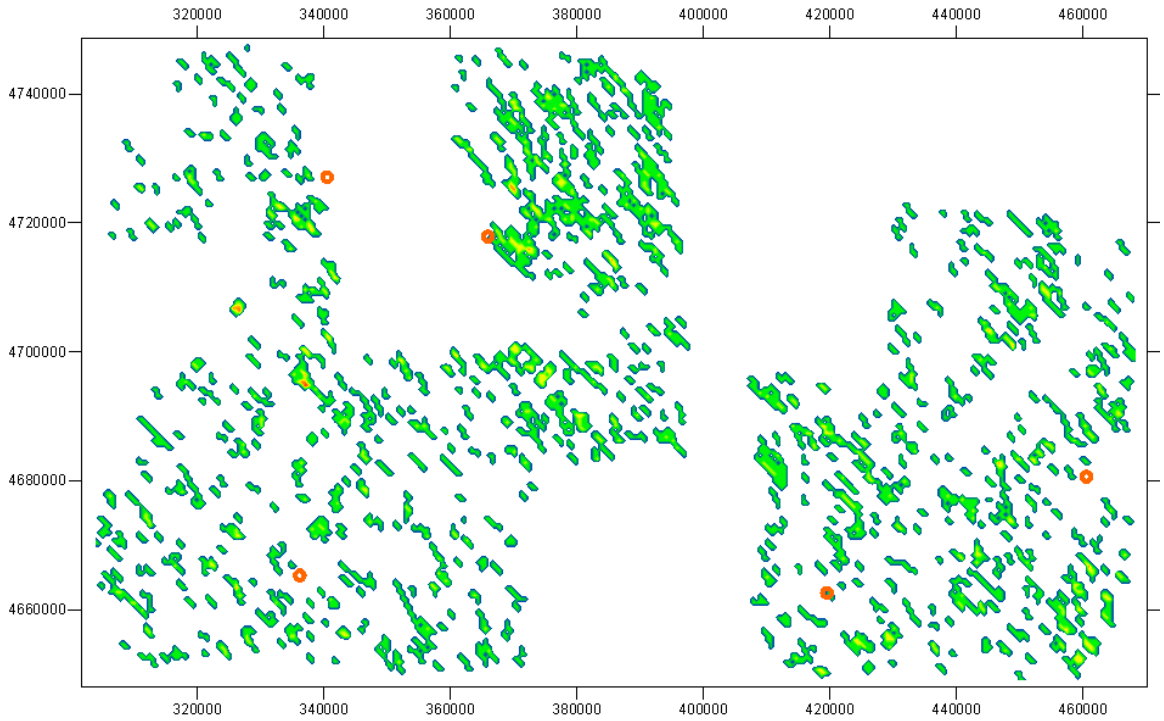

Figure 6.4,5&6-75. Lineament density map from NW-trending DEM lineaments for the entire project area. Colors show lineament density in counts per 0.333 mi^2 (0.862 km^2). Coordinates are given in meters in UTM (N18) projection. From Zelazny (2011).

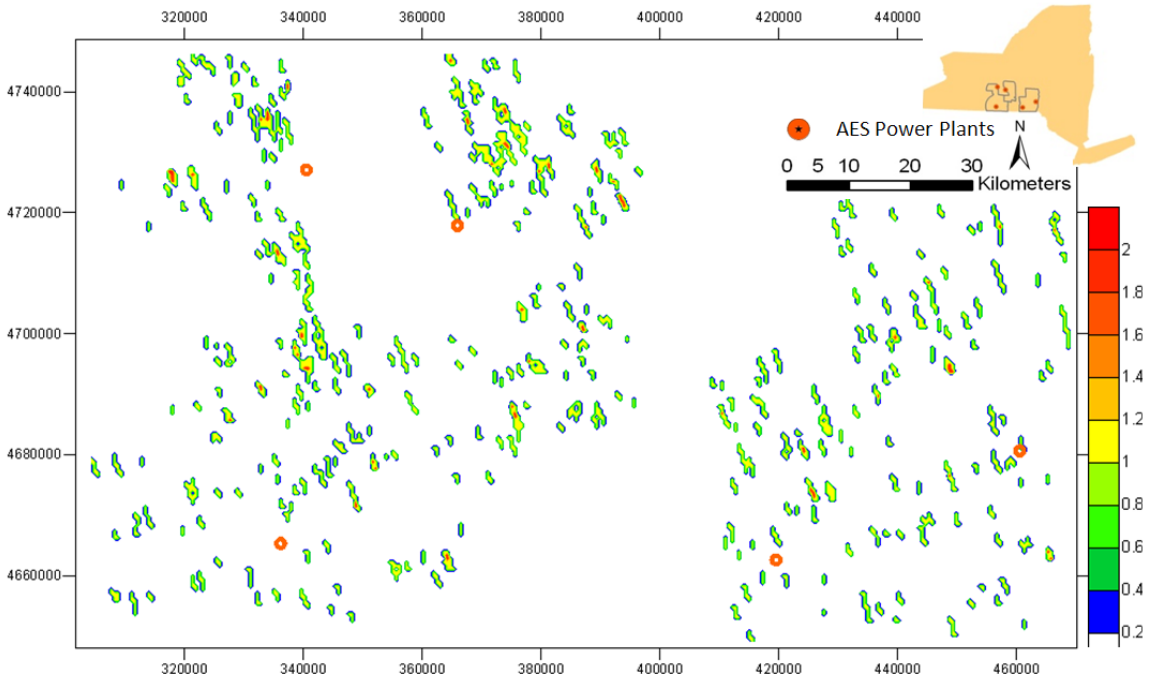

Figure 6.4,5&6-76. Lineament density map from NNW-trending DEM lineaments for the entire project area. Colors show lineament density in counts per 0.333 mi^2 (0.862 km^2). Coordinates are given in meters in UTM (N18) projection. From Zelazny (2011).

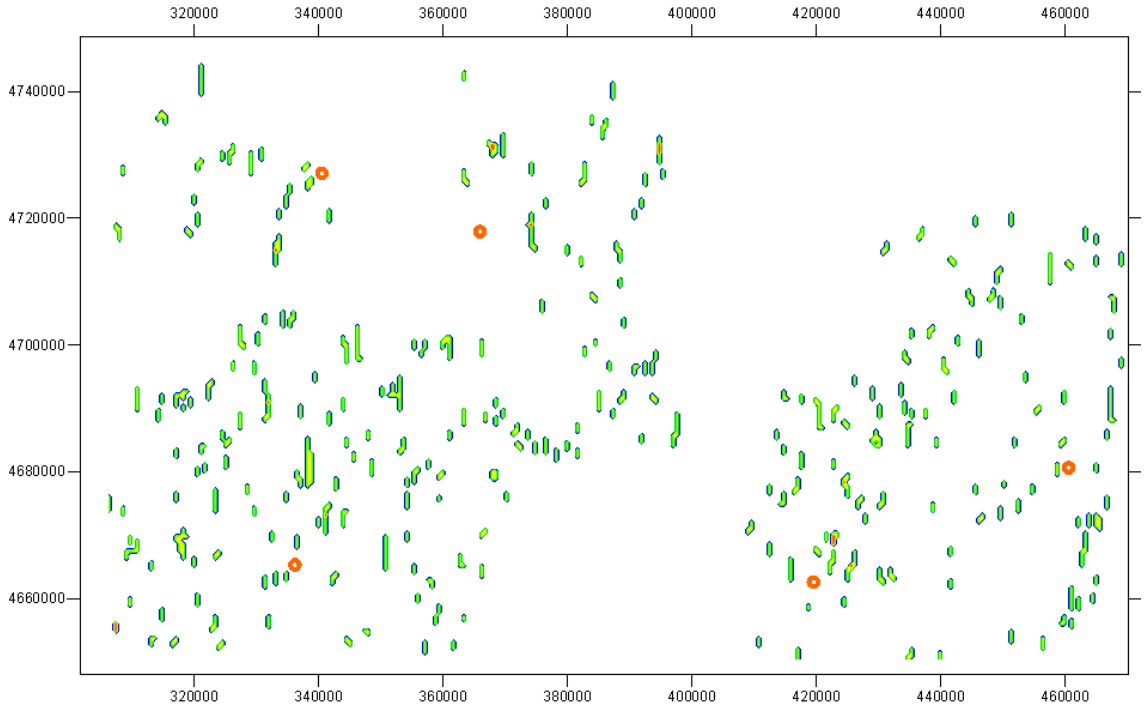

Figure 6.4,5&6-77. Lineament density map from N-trending DEM lineaments for the entire project area. Colors show lineament density in counts per 0.333 mi^2 (0.862 km^2). Coordinates are given in meters in UTM (N18) projection. From Zelazny (2011).

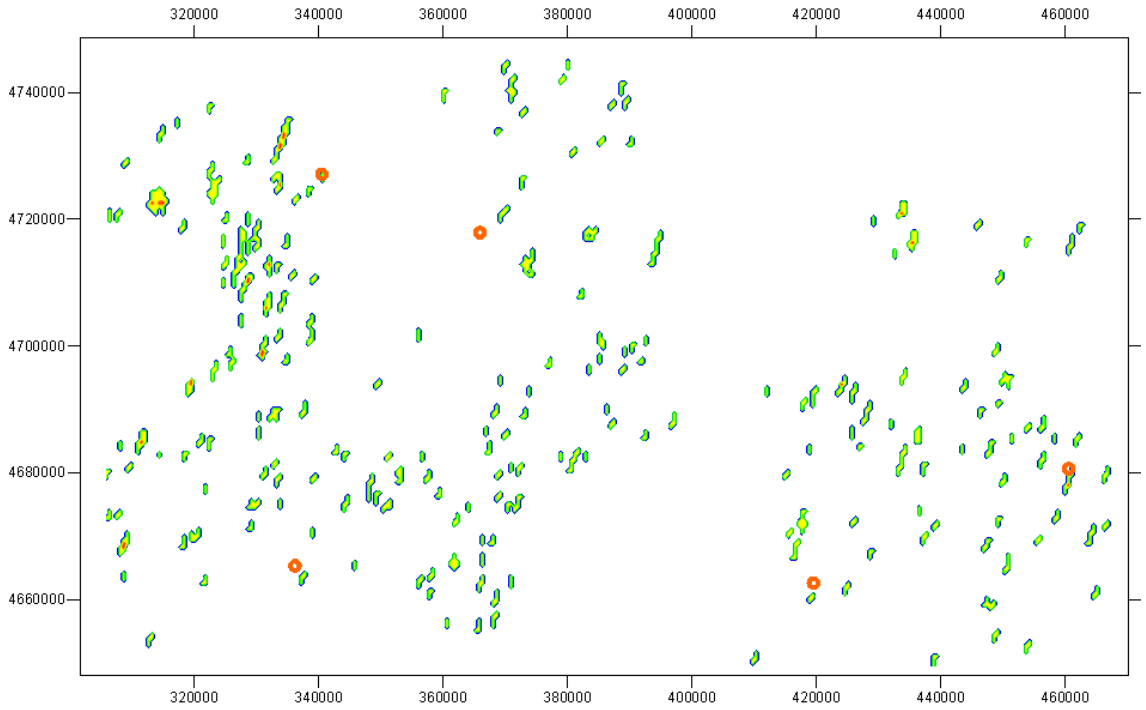

Figure 6.4,5&6-78. Lineament density map from NNE-trending DEM lineaments for the entire project area. Colors show lineament density in counts per 0.333 mi^2 (0.862 km^2). Coordinates are given in meters in UTM (N18) projection. From Zelazny (2011).

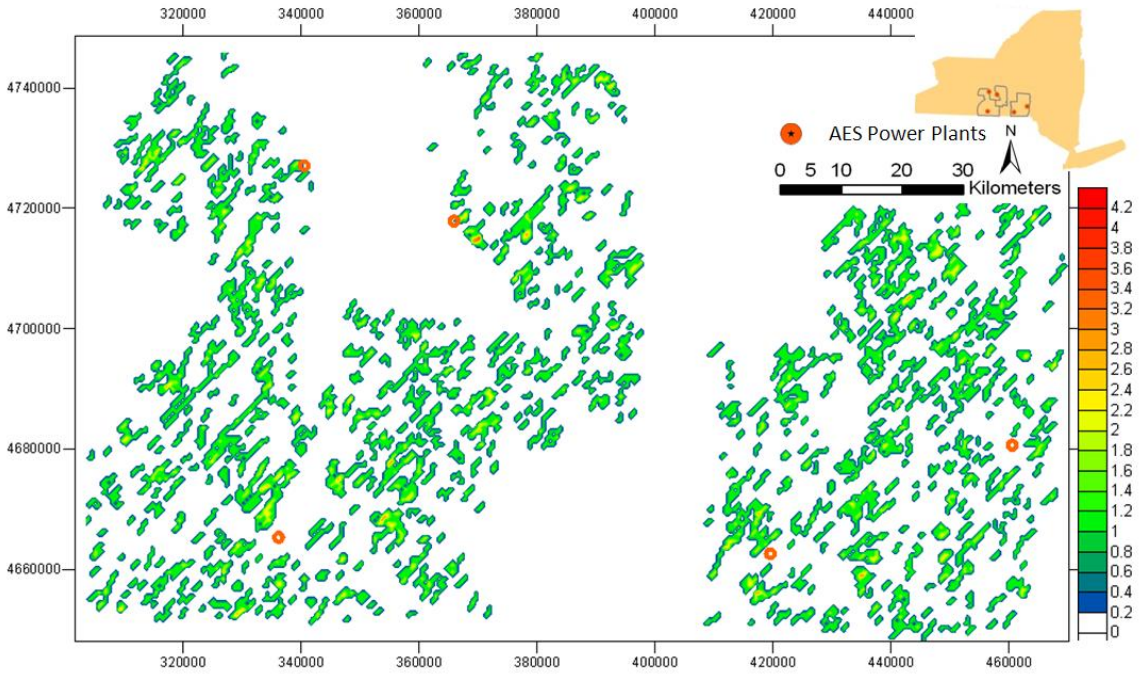

Figure 6.4,5&6-79. Lineament density map from NE-trending DEM lineaments for the entire project area. Colors show lineament density in counts per 0.333 mi^2 (0.862 km^2). Coordinates are given in meters in UTM (N18) projection. From Zelazny (2011).

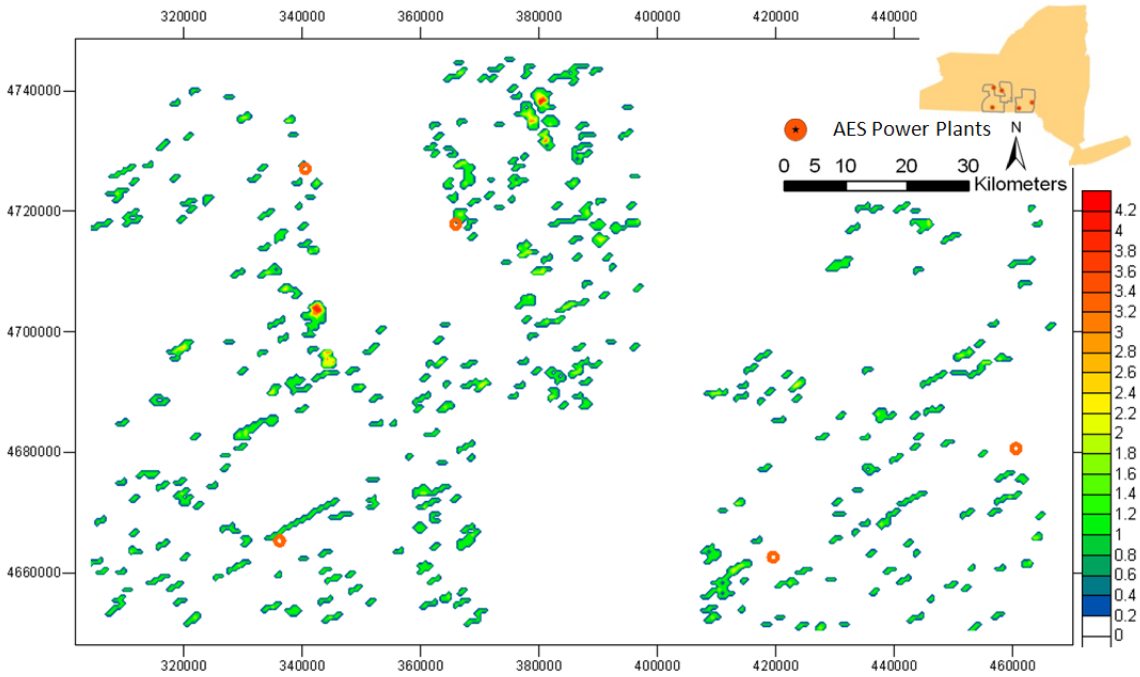

Figure 6.4,5&6-80. Lineament density map from ENE-trending DEM lineaments for the entire project area. Colors show lineament density in counts per 0.333 mi^2 (0.862 km^2). Coordinates are given in meters in UTM (N18) projection. From Zelazny (2011).

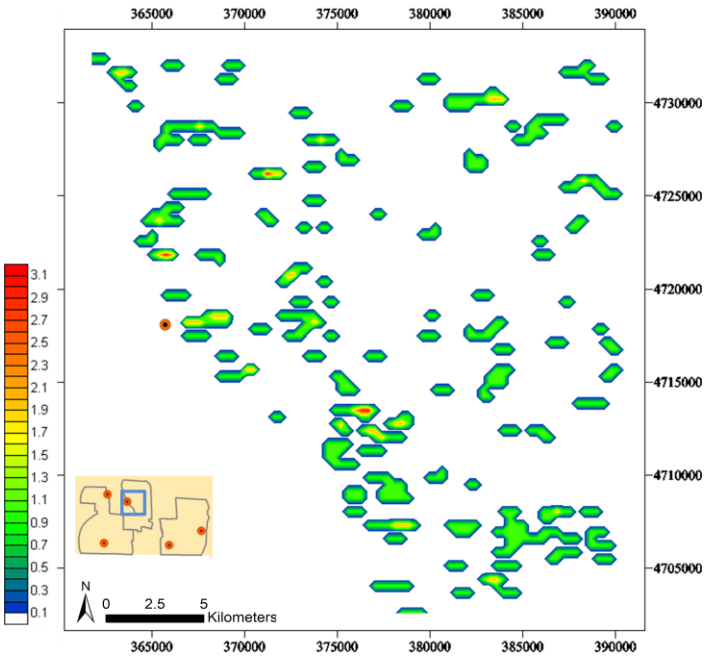

Figure 6.4,5&6-81. Density map for E-trending ASTER lineaments in the Cayuga Subset. Colors show lineament density in counts per 0.05 mi^2 (.129 km^2). Coordinates are given in meters in UTM (N18) projection. From Zelazny (2011).

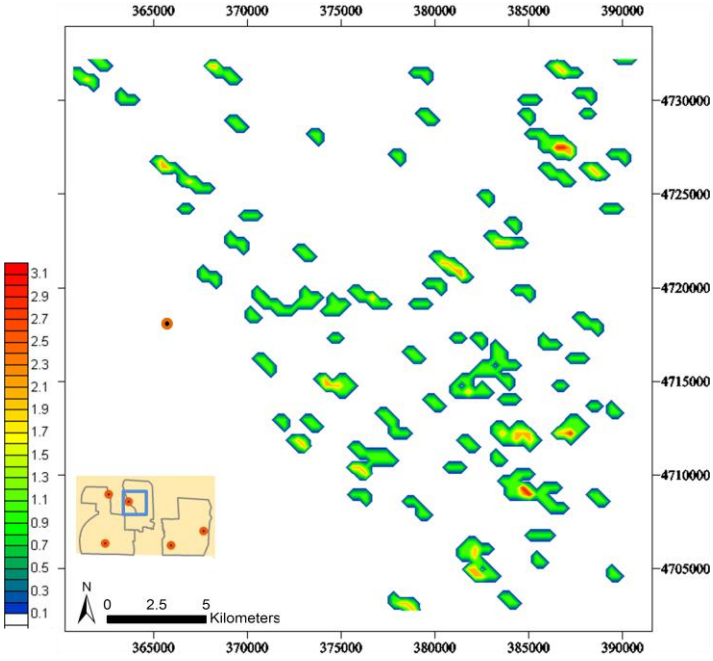

Figure 6.4,5&6-82. Density map for WNW-trending ASTER lineaments in the Cayuga Subset. Colors show lineament density in counts per 0.05 mi^2 (.129 km^2). Coordinates are given in meters in UTM (N18) projection. From Zelazny (2011).

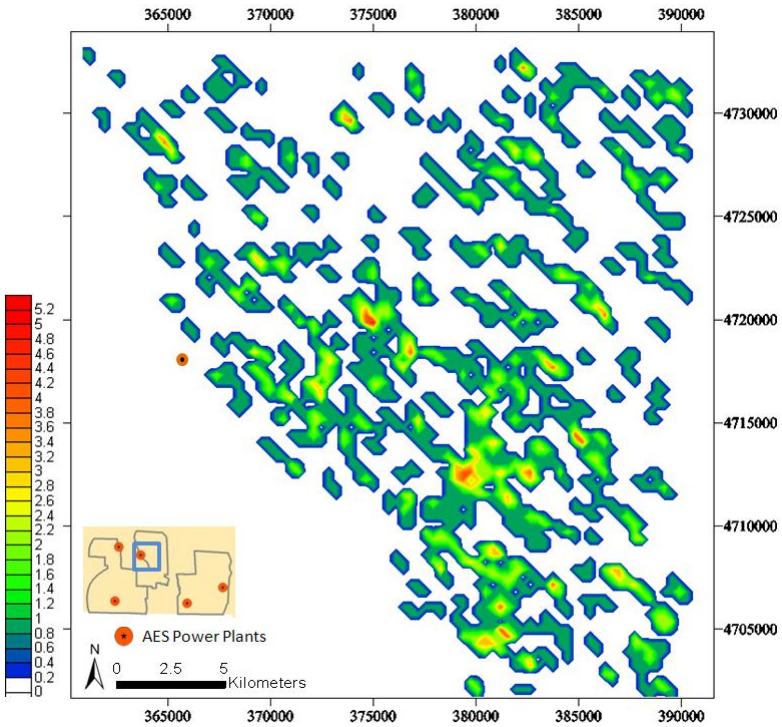

Figure 6.4,5&6-83. Density map for NW-trending ASTER lineaments in the Cayuga Subset. Colors show lineament density in counts per 0.05 mi^2 (.129 km^2). Coordinates are given in meters in UTM (N18) projection. From Zelazny (2011).

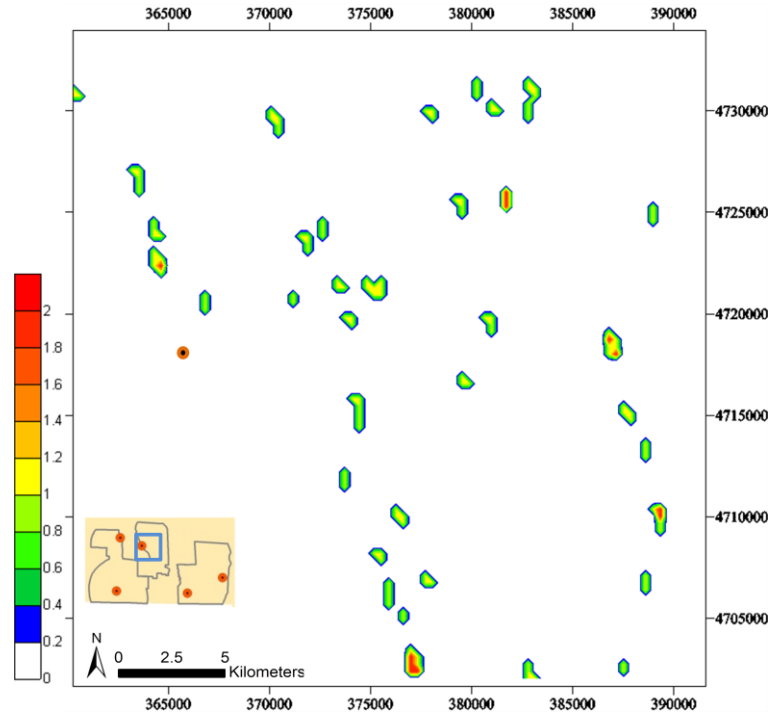

Figure 6.4,5&6-84. Density map for NNW-trending ASTER lineaments in the Cayuga Subset. Colors show lineament density in counts per 0.05 mi^2 (.129 km^2). Coordinates are given in meters in UTM (N18) projection. From Zelazny (2011).

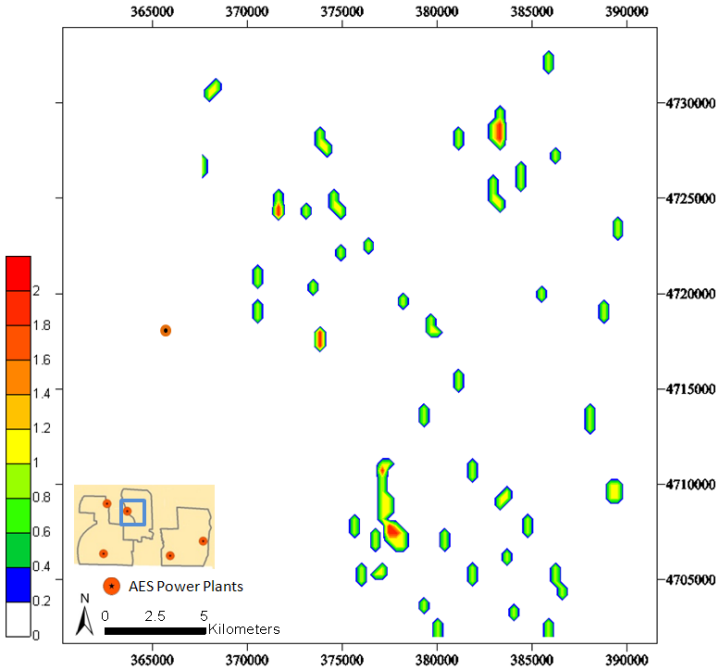

Figure 6.4,5&6-85. Density map for N-trending ASTER lineaments in the Cayuga Subset. Colors show lineament density in counts per 0.05 mi^2 (.129 km^2). Coordinates are given in meters in UTM (N18) projection. From Zelazny (2011).

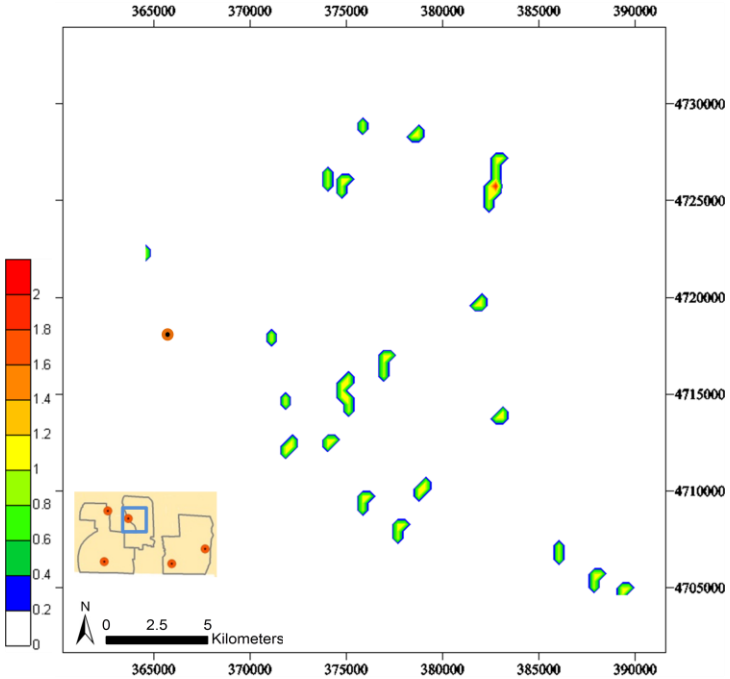

Figure 6.4,5&6-86. Density map for NNE-trending ASTER lineaments in the Cayuga Subset. Colors show lineament density in counts per 0.05 mi^2 (.129 km^2). Coordinates are given in meters in UTM (N18) projection. From Zelazny (2011).

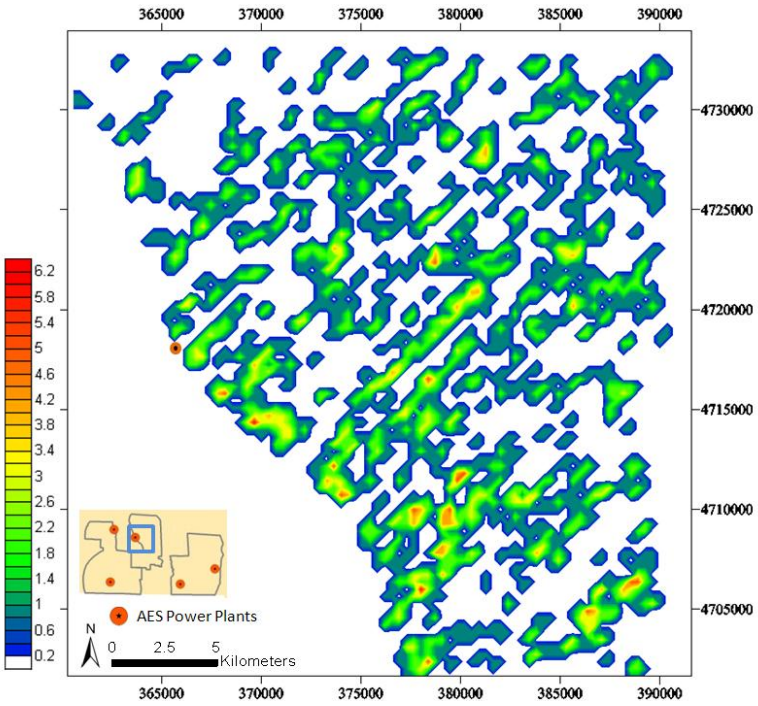

Figure 6.4,5&6-87. Density map for NE-trending ASTER lineaments in the Cayuga Subset. Colors show lineament density in counts per 0.05 mi^2 (.129 km^2). Coordinates are given in meters in UTM (N18) projection. From Zelazny (2011).

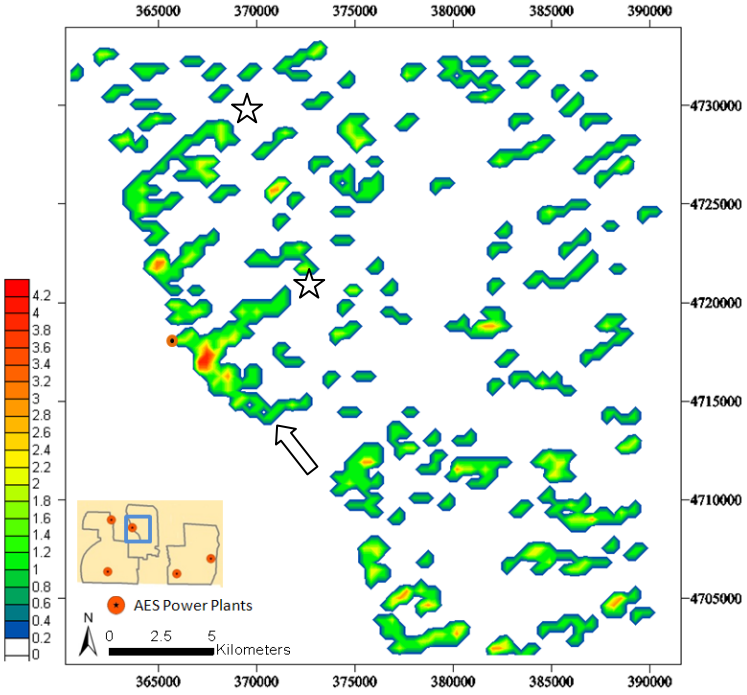

Figure 6.4,5&6-88. Density map for ENE-trending ASTER lineaments in the Cayuga Subset. Colors show lineament density in counts per 0.05 mi^2 (.129 km^2). Coordinates are given in meters in UTM (N18) projection. Features with arrow and stars discussed in text. After Zelazny (2011).

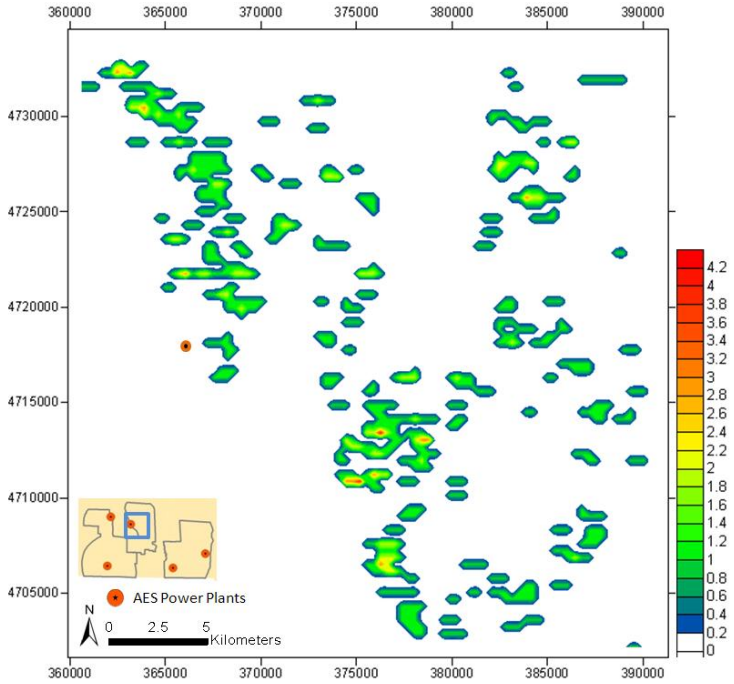

Figure 6.4,5&6-89. Density map for E-trending DEM lineaments in the Cayuga Subset. Colors show lineament density in counts per 0.05 mi^2 (.129 km^2). Coordinates are given in meters in UTM (N18) projection. From Zelazny (2011).

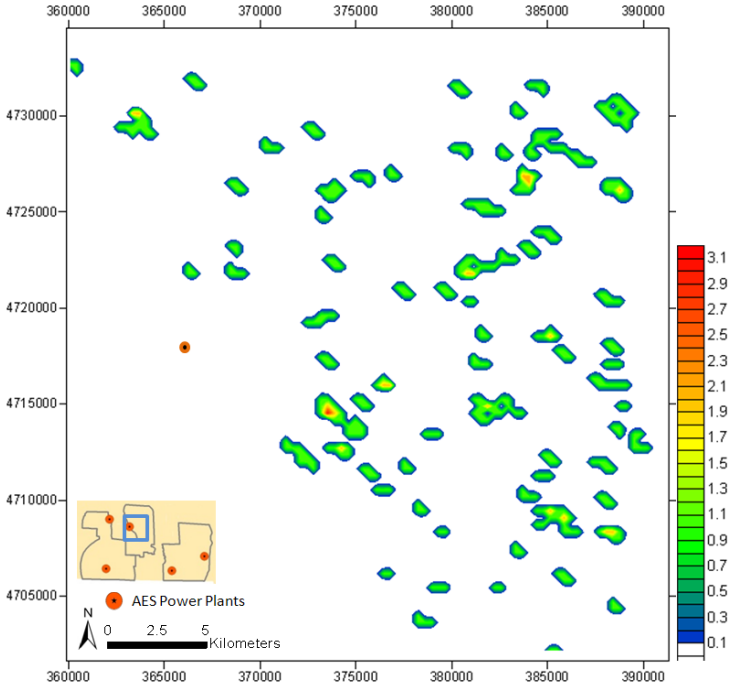

Figure 6.4,5&6-90. Density map for WNW-trending DEM lineaments in the Cayuga Subset. Colors show lineament density in counts per 0.05 mi^2 (.129 km^2). Coordinates are given in meters in UTM (N18) projection. From Zelazny (2011).

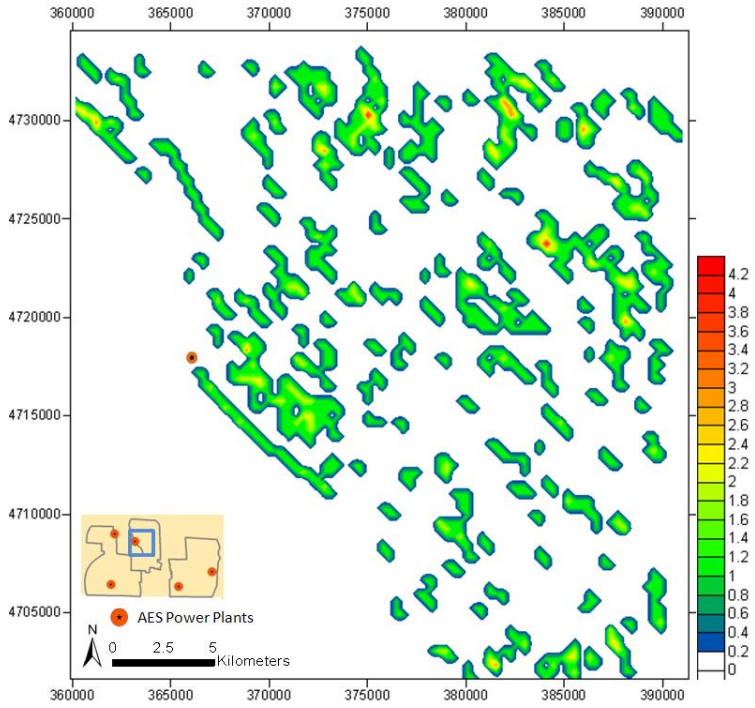

Figure 6.4,5&6-91. Density map for NW-trending DEM lineaments in the Cayuga Subset. Colors show lineament density in counts per 0.05 mi^2 (.129 km^2). Coordinates are given in meters in UTM (N18) projection. From Zelazny (2011).

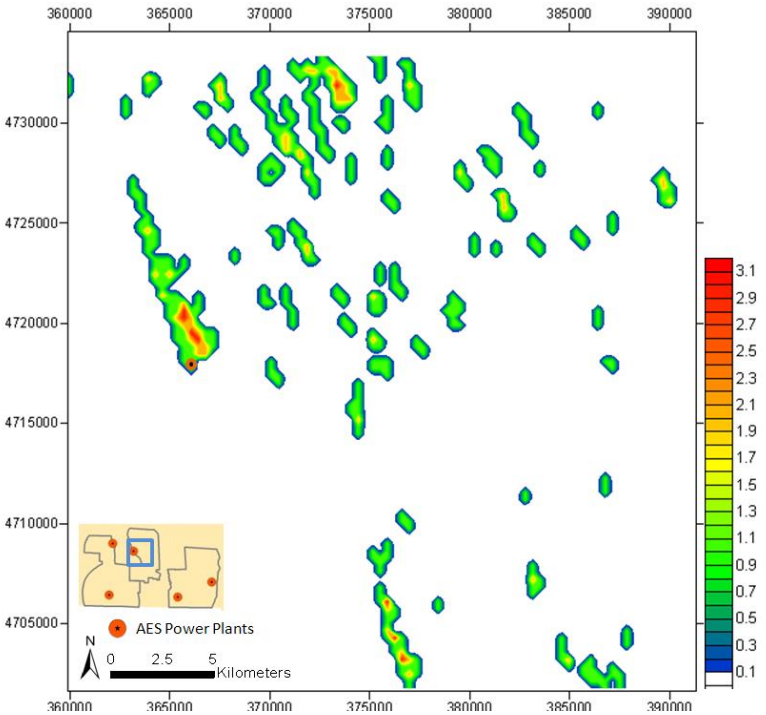

Figure 6.4,5&6-92. Density map for NNW-trending DEM lineaments in the Cayuga Subset. Colors show lineament density in counts per 0.05 mi^2 (.129 km^2). Coordinates are given in meters in UTM (N18) projection. From Zelazny (2011).

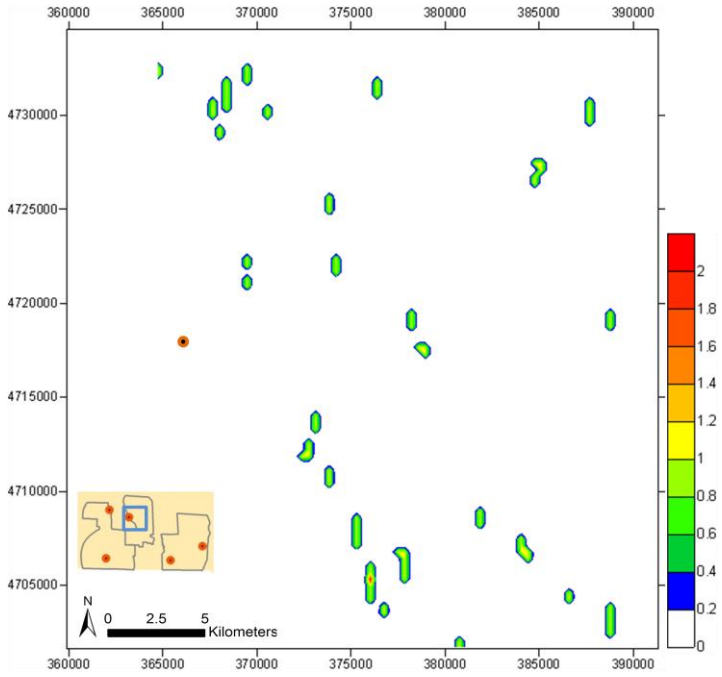

Figure 6.4,5&6-93. Density map for N-trending DEM lineaments in the Cayuga Subset. Colors show lineament density in counts per 0.05 mi^2 (.129 km^2). Coordinates are given in meters in UTM (N18) projection. From Zelazny (2011).

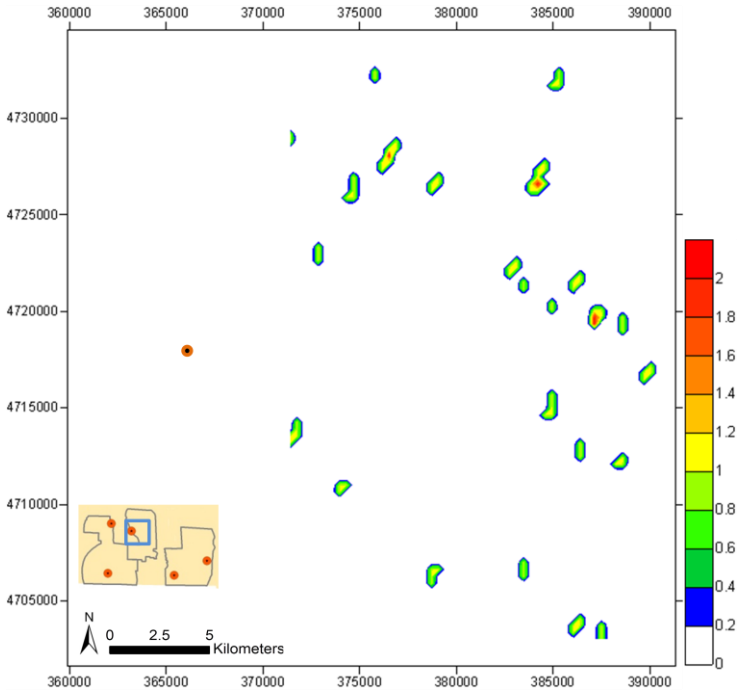

Figure 6.4,5&6-94. Density map for NNE-trending DEM lineaments in the Cayuga Subset. Colors show lineament density in counts per 0.05 mi^2 (.129 km^2). Coordinates are given in meters in UTM (N18) projection. From Zelazny (2011).

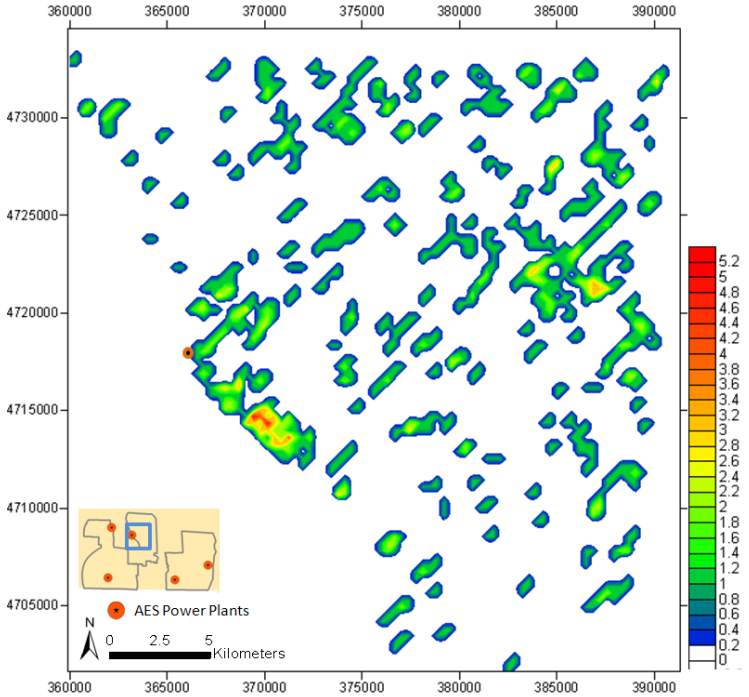

Figure 6.4,5&6-95. Density map for NE-trending DEM lineaments in the Cayuga Subset. Colors show lineament density in counts per 0.05 mi^2 (.129 km^2). Coordinates are given in meters in UTM (N18) projection. From Zelazny (2011).

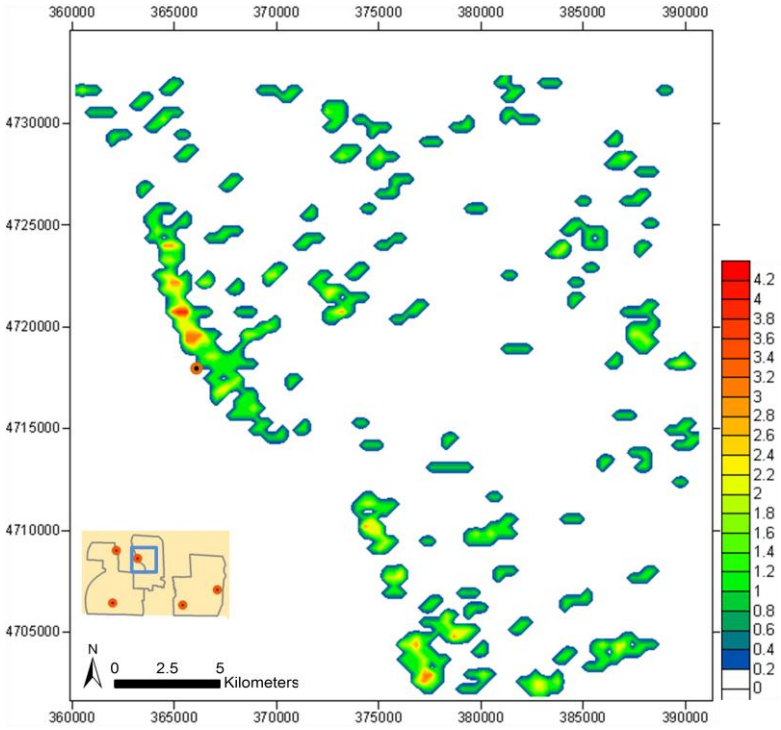

Figure 6.2-96. Density map for ENE-trending DEM lineaments in the Cayuga Subset. Colors show lineament density in counts per 0.05 mi^2 (.129 km^2). Coordinates are given in meters in UTM (N18) projection. From Zelazny (2011).

Lineament Density Map (Filtered)		Lineament Orientation Groups							
		EW	WNW	NW	NNW	NS	NNE	NE	ENE
		(79° – 105°)	(285° – 301°)	(301° - 335°)	(335° – 350°)	(350° – 11°)	(11° -21°)	(21° – 59°)	(59° – 79°)
	ASTER Project Area								
	All Orientations		X		X	X	X	X	X
	EW	X						X	
	WNW							X	
	NNW				X	X			
	NE			X		X		X	
	ENE			X	X	X		X	X
	DEM Project Area								
	All Orientations			X			X	X	
	EW	X							
	NNW				X	X		X	
	NE				X		X	X	
	ENE			X		X			X
	ASTER Cayuga Subset								
	All Orientations		X			X	X	X	X
	NW			X		X		X	
	NS					X			
	NE					X		X	
	ENE							X	
	DEM Cayuga Subset								
	All Orientations			X	X	X		X	
	EW					X	X		
	WNW			X			X	X	
	NW			X	X	X			
	NNW				X	X			
	NE			X				X	

Table 6.4,5&6-8: ASTER and DEM lineament trends for the project area and the Cayuga subset; red X's denote sub-parallel trends and black X's denote sub-perpendicular trends. From Zelazny (2011).

For the project area, the highest density of lineament orientations on ASTER filtered density orientation maps are NE, NW, N, and NNW, in descending order of count number. For lineaments in the project area on DEM filtered density orientation maps, the most abundant orientations are also NE and NW in descending order of count number. The high density of NE-trending lineaments is consistent with the primary trend in the rose diagrams, but this trend was a surprise since the detailed outcrop fracture studies in the Finger Lakes region (e.g., Engelder and Geiser, 1980; Jacobi, 2007) definitely have revealed ENE- and EW-striking fracture abundances (Set II and III of Engelder and Geiser, 1980; see for example Figure 6.4,5&6-6), but not abundant NE-striking fractures. This lack of NE-striking fractures could be partly a matter of definition, since the orientations included in the ENE-striking fracture set of Jacobi (2007) slightly overlaps the NE-trending orientations used in this study. Never-the-less, the long NE-trending strings of linked density highs of NE-trending lineaments evident in Figure 6.4,5&6-73 are clearly not ENE trends, and do not simply reflect the ENE-striking fractures and faults found in Jacobi (2007) or the Set II fractures measured by Engelder and Geiser (1980, Figure 6.4,5&6-6). These NE-trending strings of linked density highs of NE-trending lineaments are clearly not related to Set II and Set III (J1) fractures in the eastern focus area where there are relatively few fractures striking NE (see Figures 6.4,5&6-8 and 6.4,5&6-9); rather, in the eastern focus area Set II (fold parallel) fractures strike WNW and Set I (cross-strike)

fractures strike NNE (compare Figure 6.4,5&6-6 to Figure 6.4,5&6-71). The NE-trending strings of linked density highs of NE-trending lineaments may be related to fault systems in some areas (see more discussion in following section). For example, the Auburn Fault System (Jacobi, 2002) strikes approximately NE in the northwestern part of the central focus area, a major fault was proposed by Fakundiny (2002) based on EarthSat (1997) lineaments that extends NE from the southern up of Cayuga Lake, and NE-striking faults were proposed by Jacobi (2007a) based on aeromagnetics (Figure 6.4,5&6-16) in the central focus area.

In the central part of the western focus area, strings of linked density highs (of NE-trending lineaments) trend both NE and NNE. These trends, especially the NNE trend, are approximately coincident with aeromagnetic and EarthSat (1997) lineaments that Jacobi (2007) proposed supported the presence of NNE-striking faults in the region; such faults had been previously proposed by Isachsen and McKendree (1977, see Figure 6.4,5&6-13) and Murphy (1981, see Figure 6.4,5&6-14).

The abundant high densities of NW-trending lineaments are also consistent with the trends shown in the rose diagrams. In the western and central focus areas, the NW density trends are somewhat close to the orientations of some of the Set I fractures (compare Figure 6.4,5&6-6 to Figure 6.4,5&6-67), but as with the NE trends, this angular relationship fails totally in the eastern focus area where the NW density lineament trend is prominent, but the NW fracture trend there is nearly non-existent (Figure 6.4,5&6-8 and 6.4,5&6-9); in the eastern focus area Set I and II have rotated clockwise (about a vertical axis) compared to the same fracture sets in the western and central focus areas (see Figures 6.4,5&6-6 and 6.4,5&6-5).

Other lineament density trends do reflect known fracture and fault systems. For example, high densities in E-trending ASTER and DEM lineament in the central focus area and in the east central region of the western focus area (Figures 6.4,5&6-65 and 6.4,5&6-73) reflect E-striking fractures associated with faults related to the salt-cored Alleghanian folds (Wedel, 1932; Jacobi, 2007). Such a relationship is especially prominent near the southern tips of Seneca and Cayuga lakes. N-trending lineament density strings (Figure 6.4,5&6-69) may be related to N-striking faults, such as in the central focus area and the eastern part of the western focus area, where N-striking faults have been proposed (Bradley et al., 1941; Jacoby, 1966; Murphy, 1981; Jacobi 2002, 2007).

The dominant density trends in filtered density maps of both ASTER and DEM images for the Cayuga subset are NW and NE (Figures 6.4,5&6-83, 6.4,5&6-87, 6.4,5&6-91 and 6.4,5&6-95), like those found for the entire project area. And like the problems with the NE density (especially) for the entire project area, the same problems occur in this detailed area for NW and NE-trending lineaments. In this area detailed fracture studies found primarily ENE- and E-striking fractures, not NE-striking (e.g., Jacobi, 2007). The high density clusters of E-tending lineaments in the center of the area (southeast of the power plant) in both ASTER and DEM data (Figures 6.4,5&6-81 and 6.4,5&6-89) are consistent with the E-trending Fir Tree

Anticline which occurs approximately in the same area, where tightly-spaced E-striking fractures were observed (Jacobi, 2007). ENE-trending strings of linked high density nodes of ENE-trending lineaments in ASTER (and less pronounced in DEM) data (stars in Figure 6.4,5&6-88) are near ENE-striking faults proposed on the basis of coincident high frequency of ENE-striking fractures, aeromagnetic anomalies trending ENE, ENE-trending EarthSat (1997) lineaments, faults observed in seismic refection profiles, and soil gas anomalies (Jacobi, 2007) . The NNW strings of linked high density NNW-trending lineaments in the DEM data (Figure 6.4,5&6-92) are consistent with the Set I fractures and possible faults in the area (Figure 6.4,5&6-6; Engelder and Geiser, 1980; Jacobi, 2007). Similarly, the N-trending linked density highs of N-trending lineaments (Figure 6.4,5&6-85) correspond to probable N-striking faults in the region ((Bradley et al., 1941; Jacoby, 1966; Murphy, 1981; Jacobi 2002, 2007).

In addition to identifying strings and clusters of linked lineament high density nodes that trend collinearly, other strings and clusters of linked lineament high density nodes trends (sub) perpendicular to the filtered density lineament orientations. As shown above, and in detail in the following section, the strings that trend collinearly with the orientation of the lineaments probably indicate faults. However, what can be inferred from the strings/clusters that trend (sub) perpendicular to the lineament orientation? A good example of this pattern is shown in Figure 6.4,5&6-88, where a prominent NNW-trending cluster of high density nodes of ENE-trending lineaments occurs along the northwestern margin of the study area (arrow in Figure 6.4,5&6-88). This zone of high density is related to the outcrop belt of the Devonian Geneseo black shale, which is dominated by ENE-striking fractures (Jacobi, 2007). Some of the other sub parallel clusters also indicate a similar relationship. Table 6.4,5&6-8 summarizes the collinear and sub-perpendicular relationships. In summary, strings and clusters of linked lineament high density nodes that trend collinearly probably indicate faults, and strings and clusters of linked lineament high density nodes that trend sub-perpendicular to the lineament orientation at least in some cases are a function of outcrop patterns with units that carry specific fractures.

Geologic Interpretation (Subtask 6.6)

Fabric Analysis. A correspondence between the lineaments and the geologic dataset was tested and established using the method described in the methodology section. A buffer was constructed around each structural feature. A lineament was selected if it was at least partially within the buffer and the orientation of the lineament was within 20° of the trend of the buffered structure. The selected lineaments and the corresponding structural geological features are summarized in the fabric compilation tables (Tables 6.4,5&6-9 to 6.4,5&6-12).

Fractures	EW		WNW		NW		NNW		NS		NNE		ENE	
	# of Fractures	Length (km)	# of Fractures	Length (km)	# of Fractures	Length (km)	# of Fractures	Length (km)	# of Fractures	Length (km)	# of Fractures	Length (km)	# of Fractures	Length (km)
Engelder & Geiser (1979) Set I					11	Data Point	25	Data Point	10	Data Point	2	Data Point		
Engelder & Geiser (1979) Set II	8	Data Point	3	Data Point					1	Data Point			10	Data Point
ASTER Lineaments	**Count**	**Length (km)**	**Count**	**Length (km)**	**Count**	**Length (km)**	**Count**	**Length (km)**	**Count**	**Length (km)**	**Count**	**Length (km)**	**Count**	**Length (km)**
ALL	**127**	**212**	**215**	**412**	**253**	**473**	**100**	**180**	77	134	138	238	255	462
Engelder & Geiser (1979) Set I					23	33	36	61	16	29	2	3		
Engelder & Geiser (1979) Set II	13	21	5	8					1	2			27	40

Table 6.4,5&6-9. Fabric compilation of fracture orientations (Engelder and Geiser, 1979, 1980) compared to ASTER lineaments within the buffer around the fracture and within 20° of the fracture trend. Number of lineaments and fractures (count) and total length (km) are shown.

Fracture	EW		WNW		NW		NNW		NS		NNE		NE		ENE	
	Count	Length (km)	Count	Length (km)	Count	Length (km)	Count	Length (km)	Count	Length (km)	Count	Length (km)	Count	Length (km)	Count	Length (km)
McGurie (2007) (ALL)	11	22	42	93	54	119	16	32	18	31	66	149	47	136	37	71
McGurie (2007) (<2)	1	2	16	40	13	33	2	3	6	9	37	83	1	1.5	5	8
McGurie (2007) (2>4)	0	0	11	26	5	12	1	1	4	13	26	73	1	5	3	7
McGurie (2007) (>4)	0	0	10	26	6	14	4	11	5	13	8	25	0	0	3	5
Terech (2006) (ALL)	6	12	20	54	4	11			3	4	9	27			12	29
Terech (2006) (<2)	1	1	16	45	2	4			0	0	6	20			1	1
Terech (2006) (2>4)	0	0	18	51	2	7			1	1	9	27			1	2
Terech (2006) (>4)	0	0	16	48	1	2			0	0	7	18			0	0
Total	19	37	149	383	87	202	23	47	37	71	168	422	49	142.5	62	123

Table 6.4,5&6-10. Fabric compilation of fracture orientations from Terech (2006) and McGuire (2007) compared to ASTER lineaments within a 1 km buffer around the fracture and within 20° of the fracture trend. Number of lineaments and fractures (count) and total length (km) are shown.

Fault Data	EW		WNW		NW		NNW		NS		NNE		NE		ENE	
	# of faults	Length (km)	# of faults	Length (km)	# of faults	Length (km)	# of faults	Length (km)	# of faults	Length (km)	# of faults	Length (km)	# of faults	Length (km)	# of faults	Length (km)
Isachsen and McKendree (1977)	2	10							1	12					2	85
Murphy (1981)	3	45					1	11	5	146	2	35			2	80
Bradley et al. (1941)	2	10														
Jacobi (2007)			1	7	3	40	4	74	1	9	6	197	3	65	10	136
ASTER Lineaments	**Count**	**Length (km)**	**Count**	**Length (km)**	**Count**	**Length (km)**	**Count**	**Length (km)**	**Count**	**Length (km)**	**Count**	**Length (km)**	**Count**	**Length (km)**	**Count**	**Length (km)**
ALL	**118**	**203**	**203**	**390**	**275**	**535**	**104**	**189**	**87**	**154**	**133**	**245**	**390**	**792**	**270**	**474**
Isachsen and McKendree (1977)	3	1							2	1					15	24
Murphy (1981)	9	15					1	2	16	32	4	9			27	41
Bradley et al. (1941)	3	3														
Jacobi (2007)			1	2	16	30	6	13	2	2	30	56	27	65	53	92

Table 6.4,5&6-11. Fabric compilation of faults mapped by Bradley et al. (1941), Murphy (1981), Isachsen et al. (1977), and Jacobi (2007) compared to ASTER lineaments within 1 km buffer around the fault and within 20° of the fault trends. Number of lineaments and faults (count) and total length (km) are shown. Modified from Zelazny (2011).

Fault Zones	EW		NW		NE		ENE	
	# of Zones	Length (km)	# of Zones	Length (km)	# of Zones	Length (km)	# of Zones	Length (km)
Bradley et al. (1941)			1	8			4	53
Jacobi (2002)	1	99			3	185	9	776
ASTER Lineaments	**Count**	**Length (km)**	**Count**	**Length (km)**	**Count**	**Length (km)**	**Count**	**Length (km)**
ALL	**188**	**333**	**504**	**939**	**710**	**1449**	**307**	**553**
Bradley et al. (1941)			2	3			16	26
Jacobi (2002)	15	25			168	400	204	378

Table 6.4,5&6-12. Fabric compilation of faults zones mapped by Bradley et al. (1941) and Jacobi (2002) compared to ASTER lineaments within 1 km buffer around the fault zone and within 20° of fault zone trend. Number of lineaments and fault zones (total count) total length (km) are shown.

Fractures. ASTER lineaments that intersect the buffers of Engelder and Geiser's (1980) set I and Set II fractures in the project area are shown in Figure 6.4,5&6-97, and those lineaments that are within 20^0 of the fracture trend are shown in Figure 6.4,5&6-98 for the entire project area. Figures 6.4,5&6-99 to 6.4,5&6-101 reveal the lineaments coincident with Engelder and Geiser's (1980) set I and Set II fractures in the eastern focus, central focus, and western focus areas. The fabric compilation tables (Tables 6.4,5&6-8 to 6.4,5&6-12) show the number and total length of fracture data and ASTER lineaments within determined orientations of EW (259° – 281°), WNW (281° – 304°), NW (304° – 326°), NNW (326° – 348°), NS (348° – 11°), NNE (11° – 34°), and ENE (56° – 79°).

The rose diagrams for the entire project area in Figure 6.4,5&6-98 establish that lineaments with trends (sub) collinear with the strike of Engelder and Geiser's (1980) set I and Set II fractures do occur in the buffers of the measured fracture orientations. The rose diagram for the lineaments is strikingly similar to the rose diagram of the fractures both in the entire project area figure (Figure 6.4,5&6-98) and the detailed

focus area figures (Figures 6.4,5&6-99 to 6.4,5&6-101). However, what needs to be pointed out is that Set II does not strike consistently NE across the entire project area, unlike the dominant lineaments that consistently trend NE (Figure 6.4,5&6-79). Rather, the orientations of Set I and II arc across the project area. For example, in the eastern focus area, Set II fractures strike WNW and the Set I fractures strike NNE and north (Figure 6.4,5&6-99), and lineaments do trend in those orientations in the fracture localities (compare rose diagrams in Figure 6.4,5&6-99). However, in the eastern focus area in Engelder and Geiser's (1980) data none of the set I and Set II fractures strikes NE and NW (unlike the dominant lineaments in Figure 6.4,5&6-99). In the central focus area, Set II fractures strike EW, J1 (Set III) strikes ENE and Set I strikes NNW, and lineaments match these trends as well, but again the dominant lineament trend in the central focus area is NE in Figures 6.4,5&6-71 and 6.4,5&6-79—a trend not represented in the set I and set II fracture strikes in this focus area (Figure 6.4,5&6-100). In the western focus area the Set II fractures have rotated from the strike orientations in central and eastern focus areas to a primarily ENE strike, and Set I fractures strike NW/NNW and N. Lineaments at the fracture site buffers have similar trends (Figure 6.4,5&6-101), but even in this focus area where the Set II fractures have arced across the region into an ENE strike, that strike is not consistent with the dominant NE strike found in the lineaments across the entire focus area; the primary mode of lineament orientations is about 45^{o} to 55^{o} (Figure 6.4,5&6-48), and the fracture strike is between 60^{o} and 80^{o} this focus area. (Note that a secondary mode on the primary NE mode in Figure 6.4,5&6-48 does match the fracture strike orientations). Set I fractures strike approximately collinearly with one of the dominant lineament trends in the entire project area (NW in Figure 6.4,5&6-75).

Other fracture datasets used in the fabric compilation table (Table 6.4,5&6-10) were from Terech (2006), McGuire (2007) and Jacobi (2007). These datasets contained point data in the eastern focus area that represent the field sites at which fracture frequencies were recorded. ASTER lineaments that intersect the circular 1 km radius buffer of the fracture site and that trend within 20^{0} to the fracture orientation were selected for the fabric compilation table (Table 6.4,5&6-10). Table 6.4,5&6-10 reveals similar trends between NNE- and WNW- striking fractures and similarly-oriented ASTER digitized lineaments. These similarities are consistent with the similar relationship discussed above for Engelder and Geiser's (1980) set I and Set II fractures in the eastern focus area.

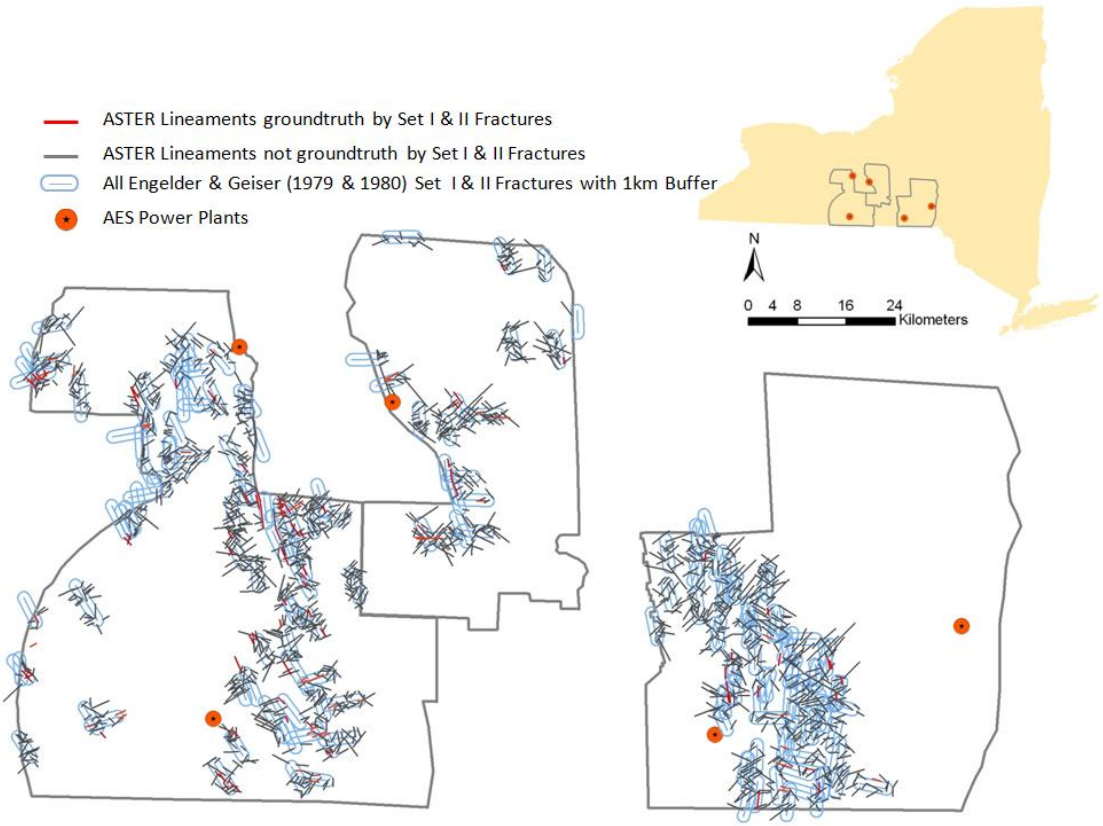

Figure 6.4,5&6-97. Map of project area with all ASTER lineaments that intersect the 1km buffer of Engelder & Geiser's (1979 & 1980) sets I & II fractures. From Zelazny (2011).

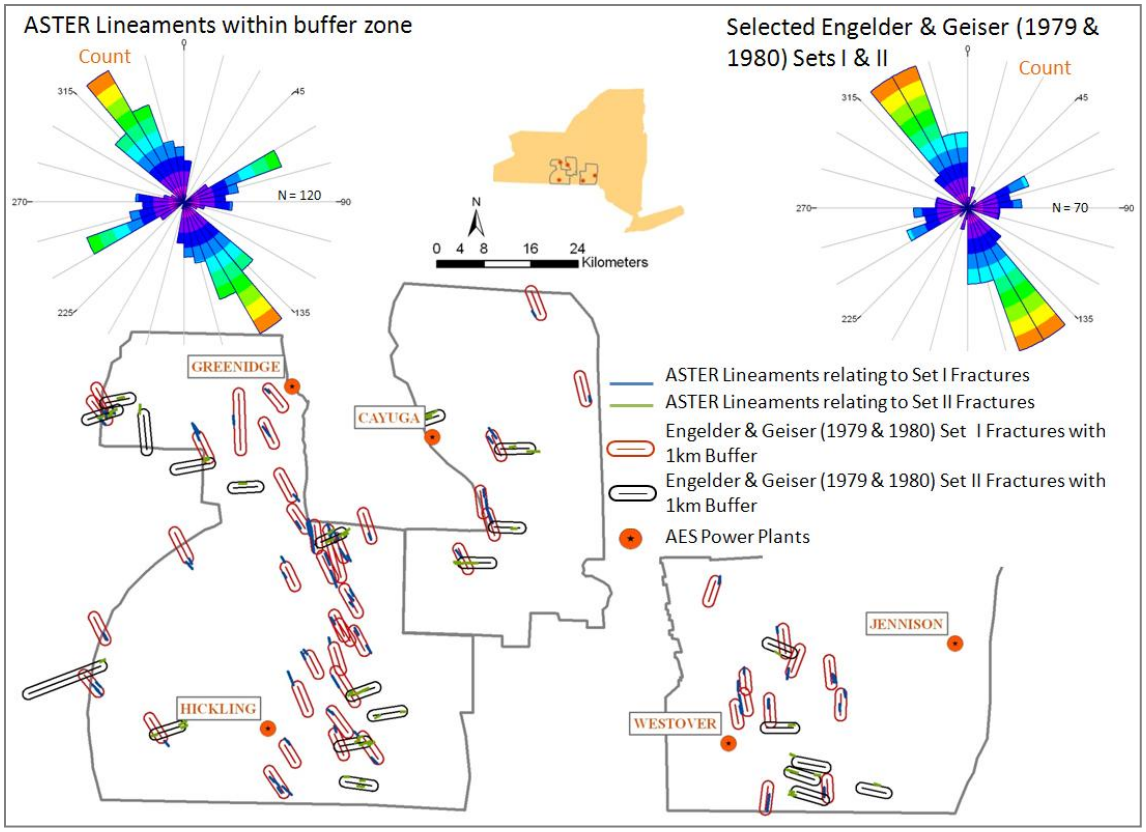

Figure 6.4,5&6-98. Engelder & Geiser's (1979 & 1980) Set I & II fractures with 1km buffer and ASTER lineaments that intersect the buffers and are oriented within 20^0 of the fracture orientation. Rose diagrams show orientations of the selected lineaments and the fractures, based on count. From Zelazny (2011).

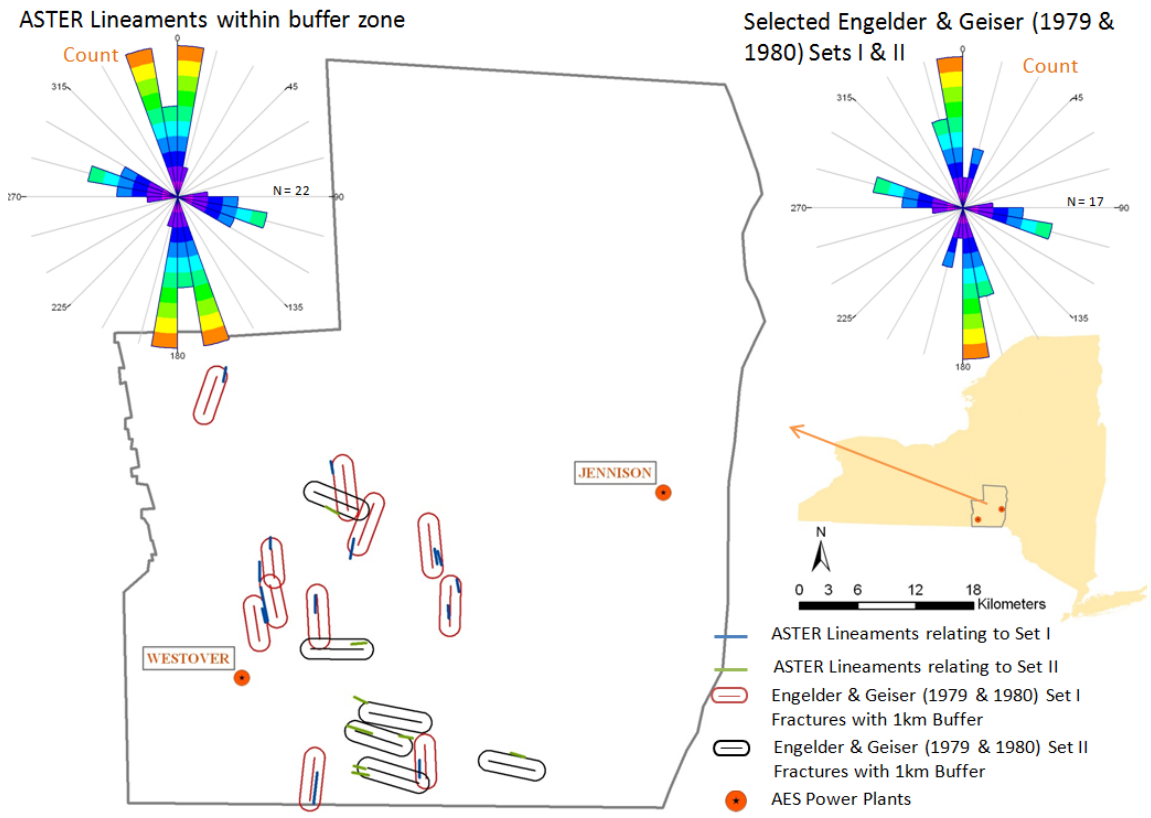

Figure 6.4,5&6-99. Engelder & Geiser's (1979 & 1980) Set I & II fractures with 1km buffer and ASTER lineaments that intersect the 1 km buffers and are oriented within 20^0 of the fracture orientation in the eastern focus area. Rose diagrams show orientations of the selected lineaments and the fractures, based on count. From Zelazny et al. (2010) and Zelazny (2011).

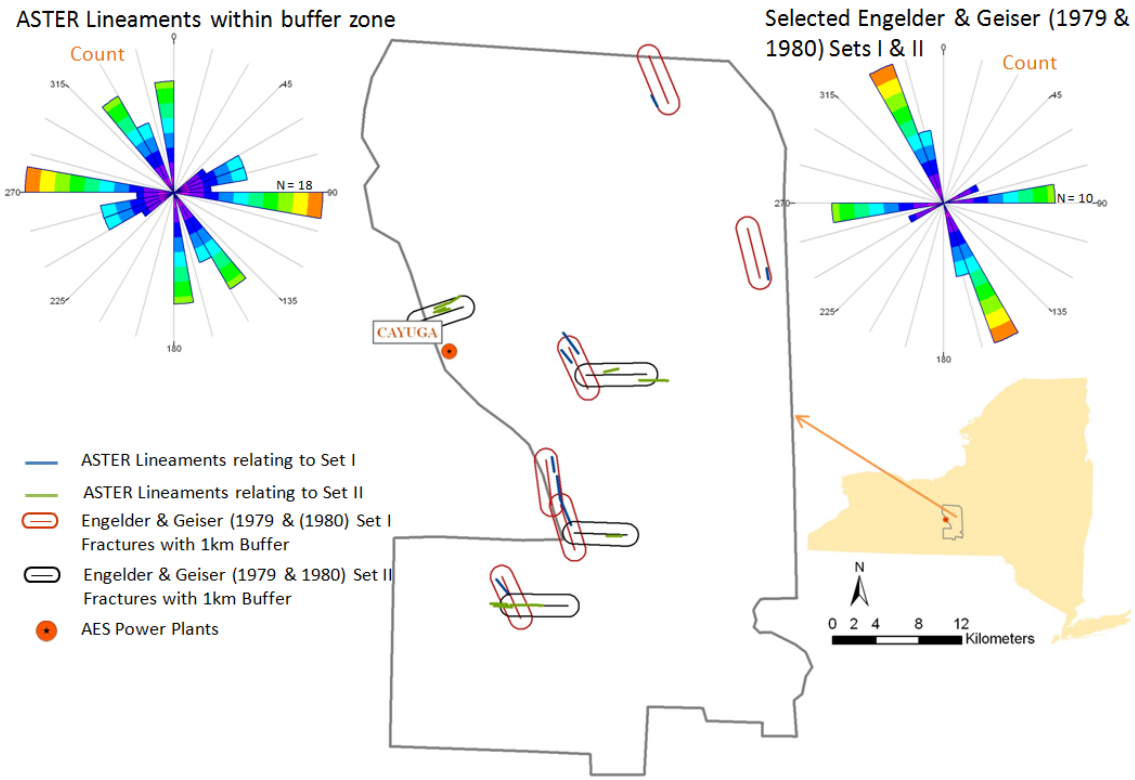

Figure 6.4,5&6-100. Engelder & Geiser's (1979 & 1980) Set I & II fractures with 1km buffer and ASTER lineaments that intersect the 1 km buffers and are oriented within 20^0 of the fracture orientation in the central focus area. Rose diagrams show orientations of the selected lineaments and the fractures, based on count. From Zelazny et al. (2010) and Zelazny (2011).

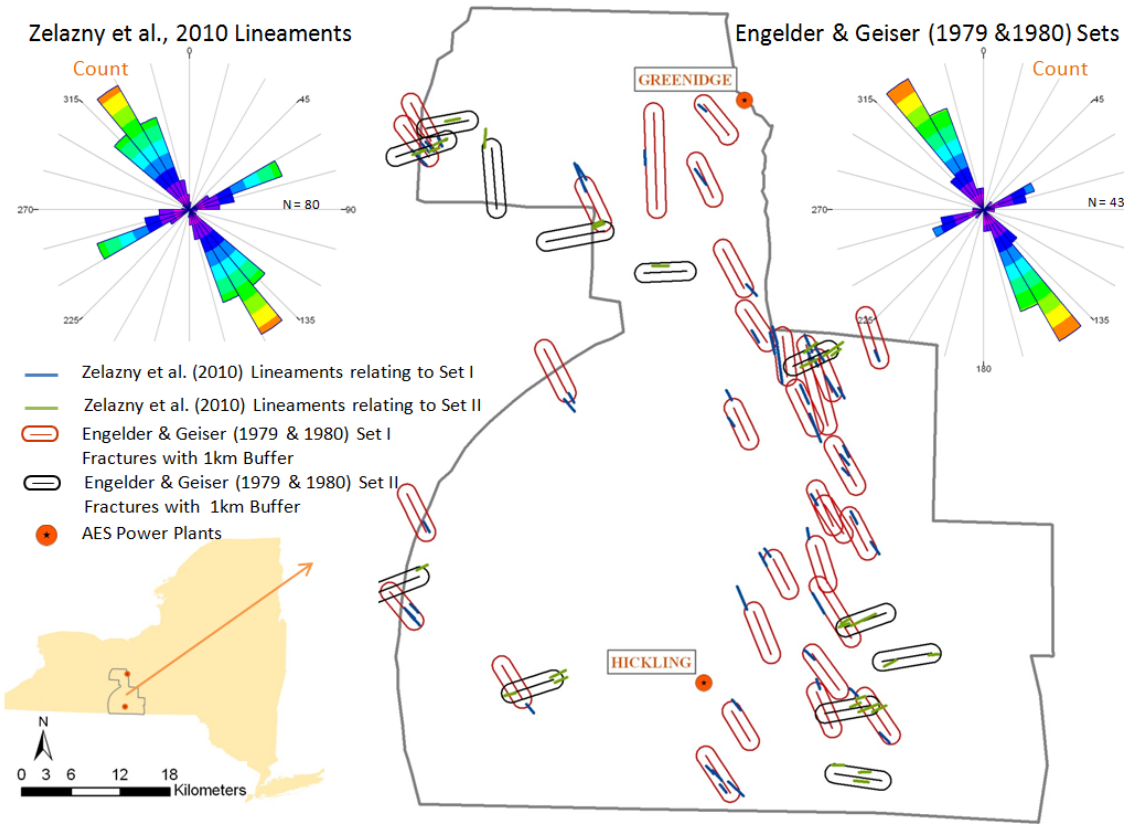

Figure 6.4,5&6-101. Engelder & Geiser's (1979 & 1980) Set I & II fractures with 1 km buffer and ASTER lineaments that intersect the 1 km buffers and are oriented within 20^0 of the fracture orientation in the western focus area. Rose diagrams show orientations of the selected lineaments and the fractures, based on count. From Zelazny et al. (2010) and Zelazny (2011).

Faults. The lineaments digitized from ASTER imagery were compared to fault data from Bradley et al. (1941), Murphy (1981), Isachsen and McKendree (1977), and Jacobi (2007). The selected ASTER lineaments that intersected the buffered faults are displayed in maps and rose diagrams for the entire project area, as well as the focus areas (western, central, and eastern) in Figures 6.4,5&6-102 to 6.4,5&6-106. The fabric compilation table (Table 6.4,5&6-11) shows the number and total length of selected fault data and ASTER lineaments, and as such summarizes the relationship between ASTER lineaments and fault data from Bradley et al. (1941), Murphy (1981), Isachsen and McKendree (1977), and Jacobi (2007a, b). The defined orientations in the table include EW (259° – 281°), WNW (281° – 304°), NW (304° – 326°), NNW (326° – 348°), NS (348° – 11°), NNE (11° – 34°), NE (34° – 56°), and ENE (56° – 79°).

The fabric compilation table for the entire project area identified the NNE, NE, and ENE orientations as fault trends that have associated liniments, and EW, and NNW that have a lesser number of faults and a lesser correlation. The positive relationship between ENE-striking faults and ASTER lineaments is a result primarily of Murphy's (1981) and Isachsen and McKendree's (1977) multiple, long ENE-striking fault systems in southwestern part of the western focus area (Figure 6.4,5&6-103 and 6.4,5&6-104), other ENE-striking shorter faults in the western focus area proposed by Murphy (1981), and ENE-striking faults in the eastern focus area proposed by Jacobi (2007b, Figure 6.4,5&6-103 and 6.4,5&6-106). The NE-striking proposed faults that coincide with lineaments were proposed by Jacobi (2007a, b) in all three focus area (Figure 6.4,5&6-103), but are most prominent in the central focus area. NNE-striking faults with lineaments occur in the western and eastern focus areas, primarily Jacobi's (2007a) faults in the western focus area and Jacobi's (2007b) faults in the eastern focus area. Northerly- and easterly-striking faults (Isachsen and McKendree, 1977 and Murphy, 1981) and related lineaments are found in the central and northern parts of the western focus area (Figures 6.4,5&6-103 and 6.4,5&6-104). Inspection of the figures (Figures 6.4,5&6-102 to 6.4,5&6-106), as well as Table 6.4,5&6-11 show that much of the length of Murphy's (1981) northerly striking faults in the central and western focus areas have almost no related ASTER lineaments. Further, inspection of Figure 6.4,5&6-102 shows that most of the proposed faults in the figure have few coincident lineaments; rather, lineaments with trends other than the fault strike intersect the buffers. Notable exceptions include the ENE-striking faults in the southern part of the western focus area and eastern focus area, NE-striking proposed faults in the eastern focus area, and northerly striking faults in the western focus area. The conclusion is, however, that it is very difficult to recognize many of the proposed faults in the present lineament data.

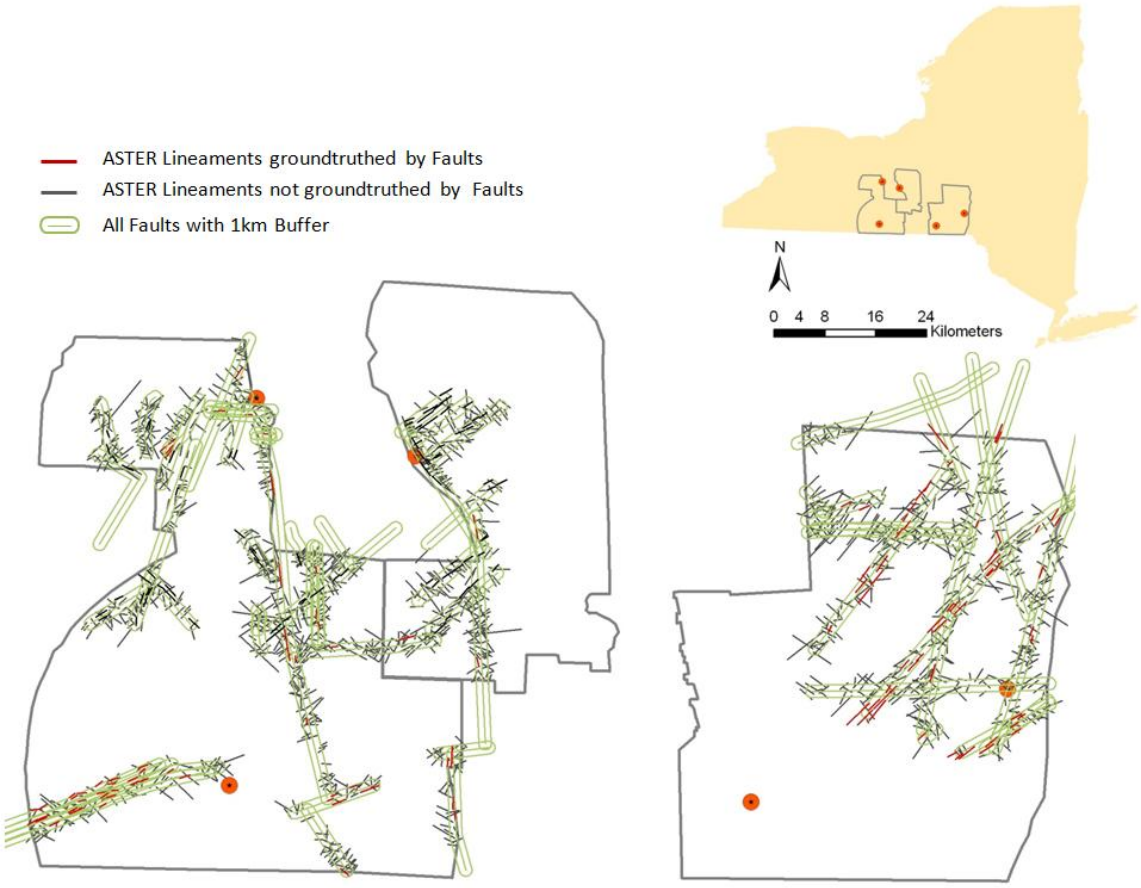

Figure 6.4,5&6-102. Map of project area with all ASTER lineaments that intersect the 1 km buffer around fault systems in the entire project area from Bradley et al. (1941), Murphy (1981), Isachsen et al. (1977), and Jacobi (2007). Lineament digitization scale was 1:125,000. Figure from Zelazny (2011).

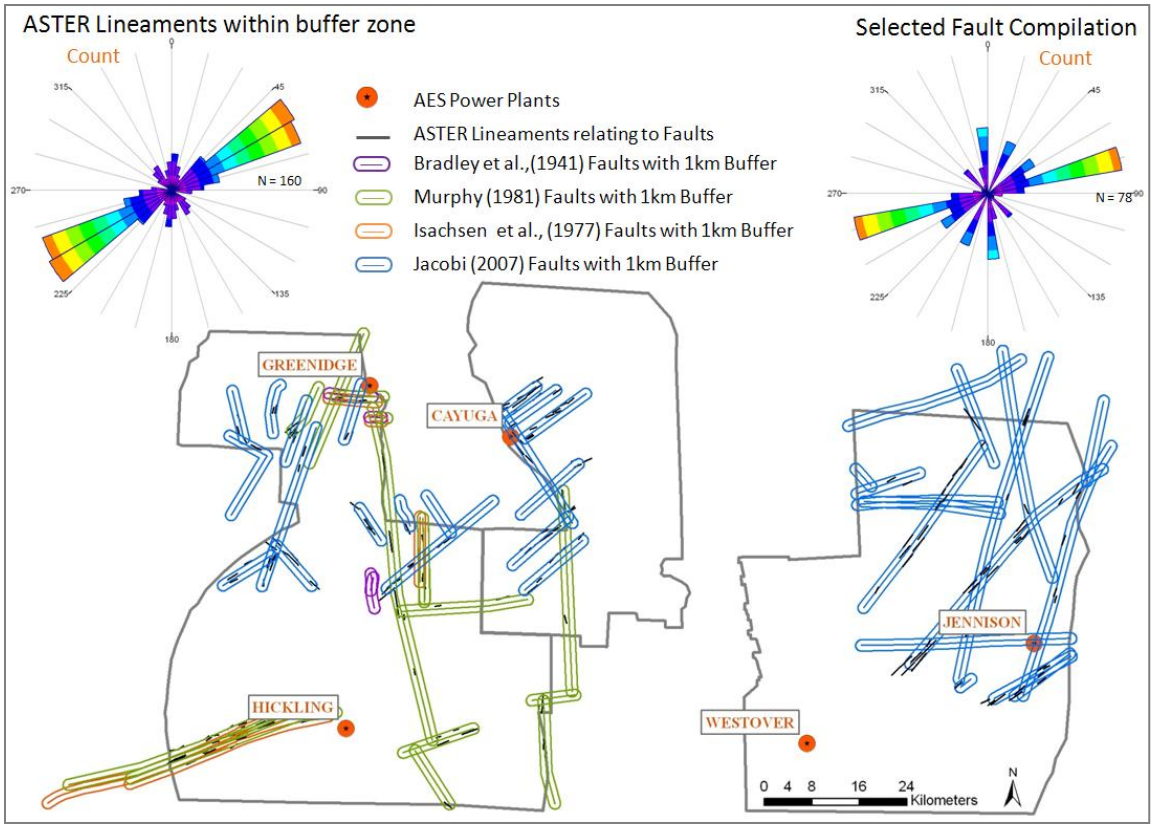

Figure 6.4,5&6-103. Selected faults from Bradley et al. (1941), Murphy (1981), Isachsen et al. (1977), and Jacobi (2007) in the entire project area with 1 km buffer and ASTER lineaments that intersect the buffer and are oriented with 20^0 of the fault strike. Rose diagrams of selected lineaments and faults are based on count. From Zelazny (2011).

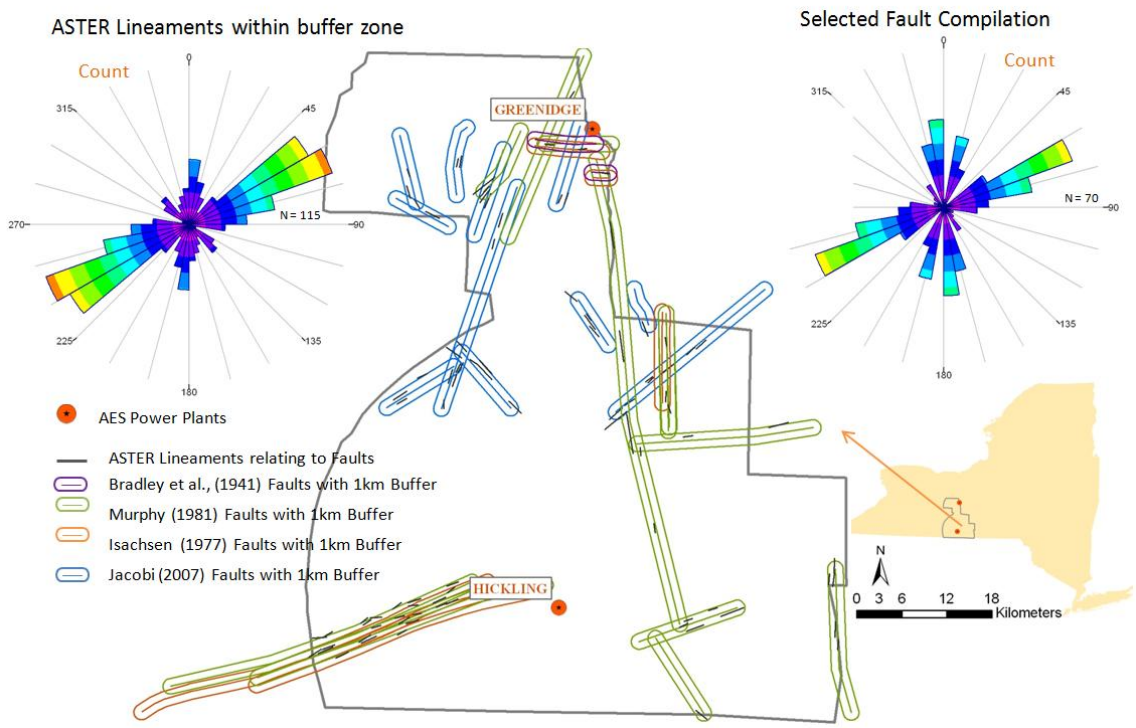

Figure 6.4,5&6-104. Selected faults from Bradley et al. (1941), Murphy (1981), Isachsen et al. (1977), and Jacobi (2007) in the western focus area with 1 km buffer and ASTER lineaments that intersect the buffer and are oriented with 20^0 of the fault strike. Rose diagrams of selected lineaments and faults are based on count. From Zelazny (2011).

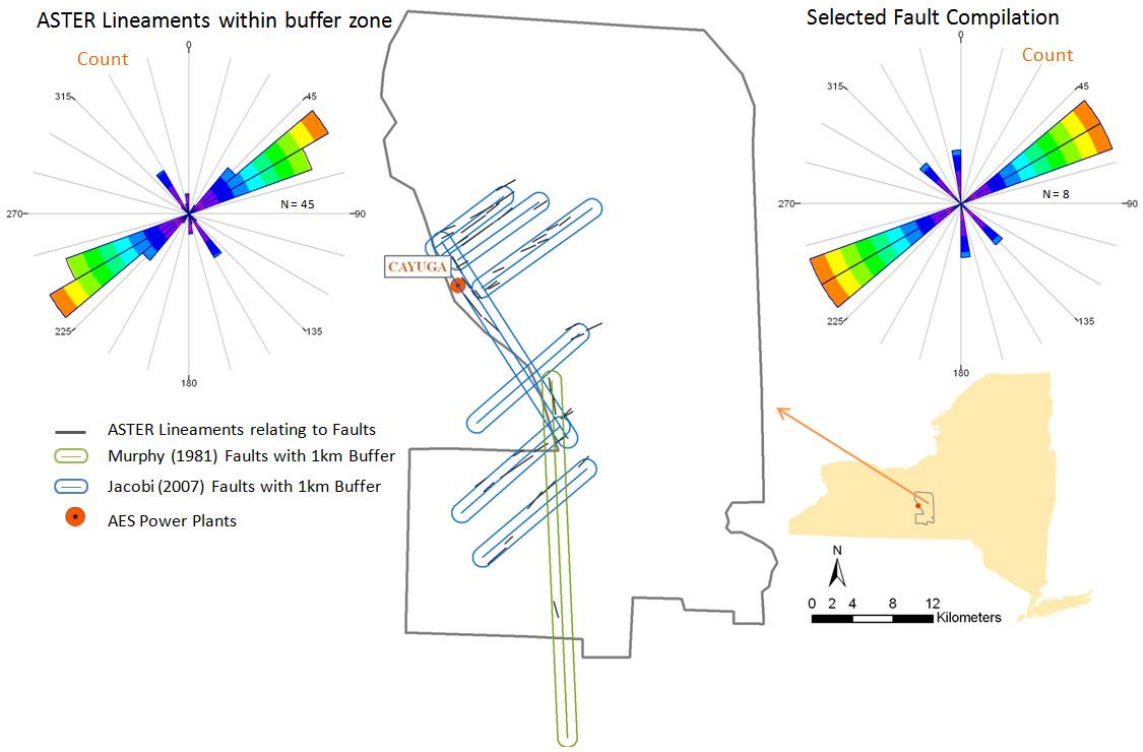

Figure 6.4,5&6-105. Selected faults from Bradley et al. (1941), Murphy (1981), Isachsen et al. (1977), and Jacobi (2007) in the central focus area with 1 km buffer and ASTER lineaments that intersect the buffer and are oriented with 20^0 of the fault strike. Rose diagrams of selected lineaments and faults are based on count. From Zelazny (2011).

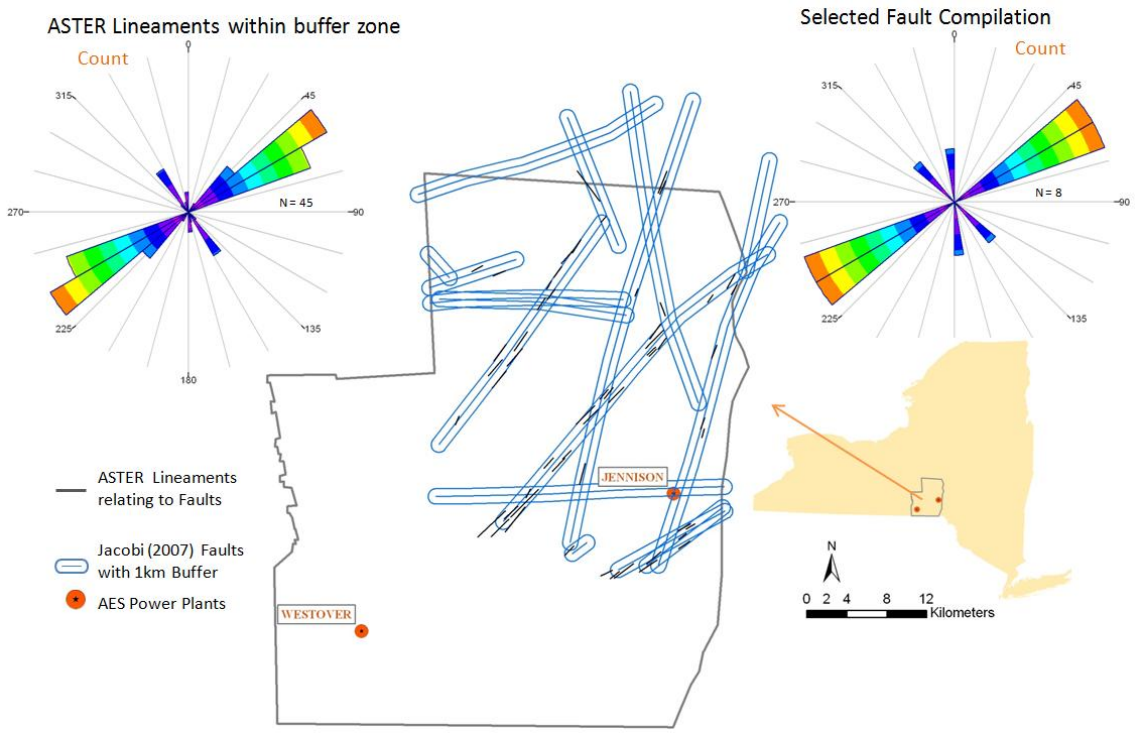

Figure 6.4,5&6-106. Selected faults from Bradley et al. (1941), Murphy (1981), Isachsen et al. (1977), and Jacobi (2007) in the eastern focus area with 1 km buffer and ASTER lineaments that intersect the buffer and are oriented with 20^0 of the fault strike. Rose diagrams of selected lineaments and faults are based on count. From Zelazny (2011).

Fault Zones. The ASTER digitized lineaments were also compared to the fault zones proposed by Bradley et al. (1941) and Jacobi (2002). Maps and rose diagrams illustrate orientations for the fault zones and coincident ASTER lineaments for the entire project area and a detailed area in the western focus area (Figures 6.4,5&6-107 to 6.4,5&6-109). The fabric compilation Table 6.4,5&6-12 shows the number and total length of known fault zones and related ASTER lineaments within determined orientations of EW (259° – 281°), NW (304° – 326°), NE (34° – 56°), and ENE (56° – 79°). ASTER lineaments match ENE- and NE-striking fault zones from Bradley et al. (1941) and Jacobi (2002) in the maps and the fabric compilation table. However, it is clear in the rose diagrams and Figure 6.4,5&6-107 that there s a significant amount of "noise" in the lineament data compared to the fault zones, even in the fairly well-defined ENE-striking fault set.

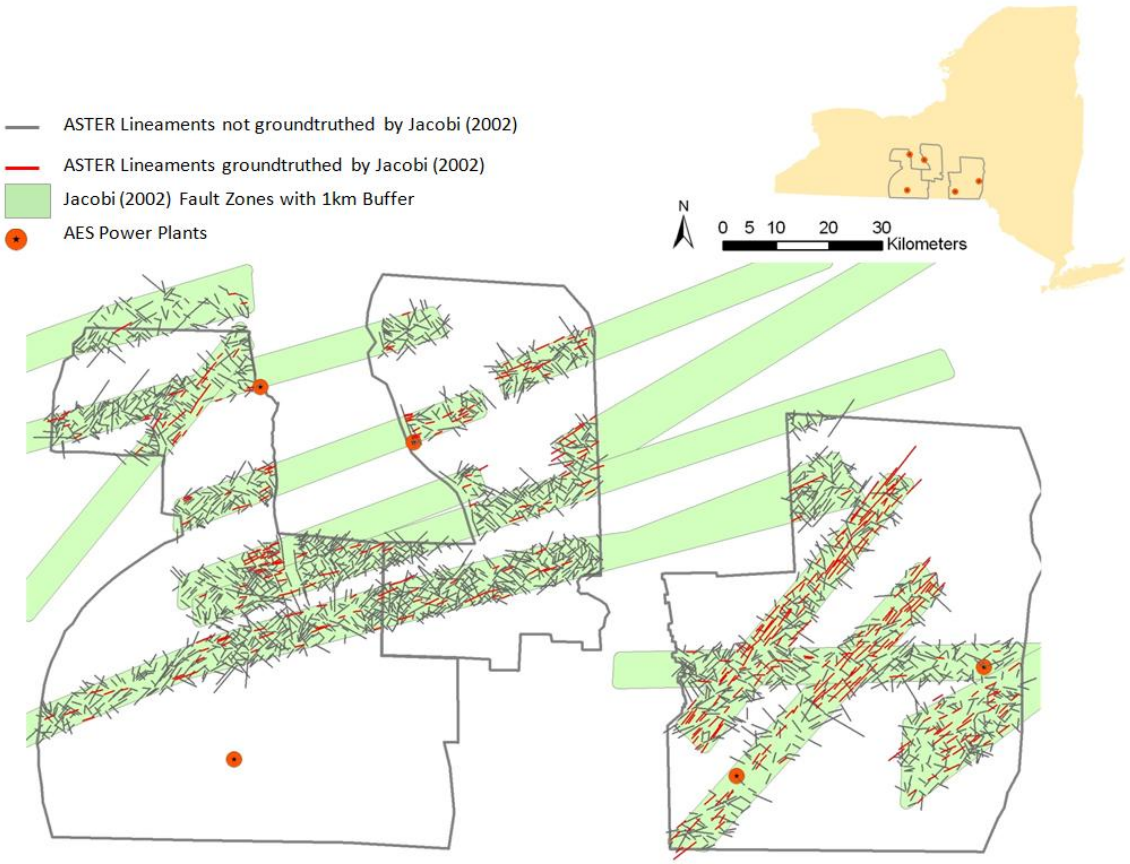

Figure 6.4,5&6-107. Map of project area with all ASTER lineaments within the 1 km buffer of Jacobi (2002) fault zones. After Zelazny (2011).

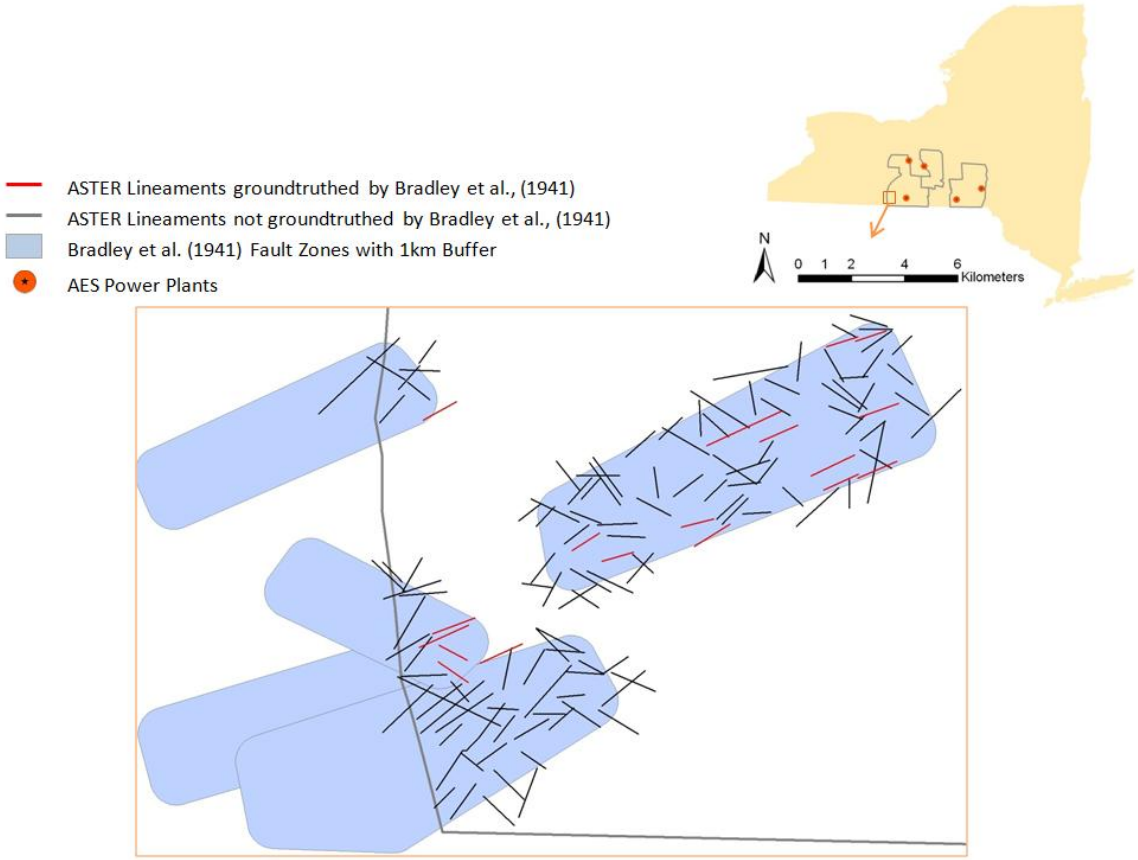

Figure 6.4,5&6-108. Detailed map of the southwestern region of the western focus area displaying Bradley et al. (1941) fault systems and all ASTER lineaments that intersect 1 km buffers around the of fault zones. After Zelazny (2011).

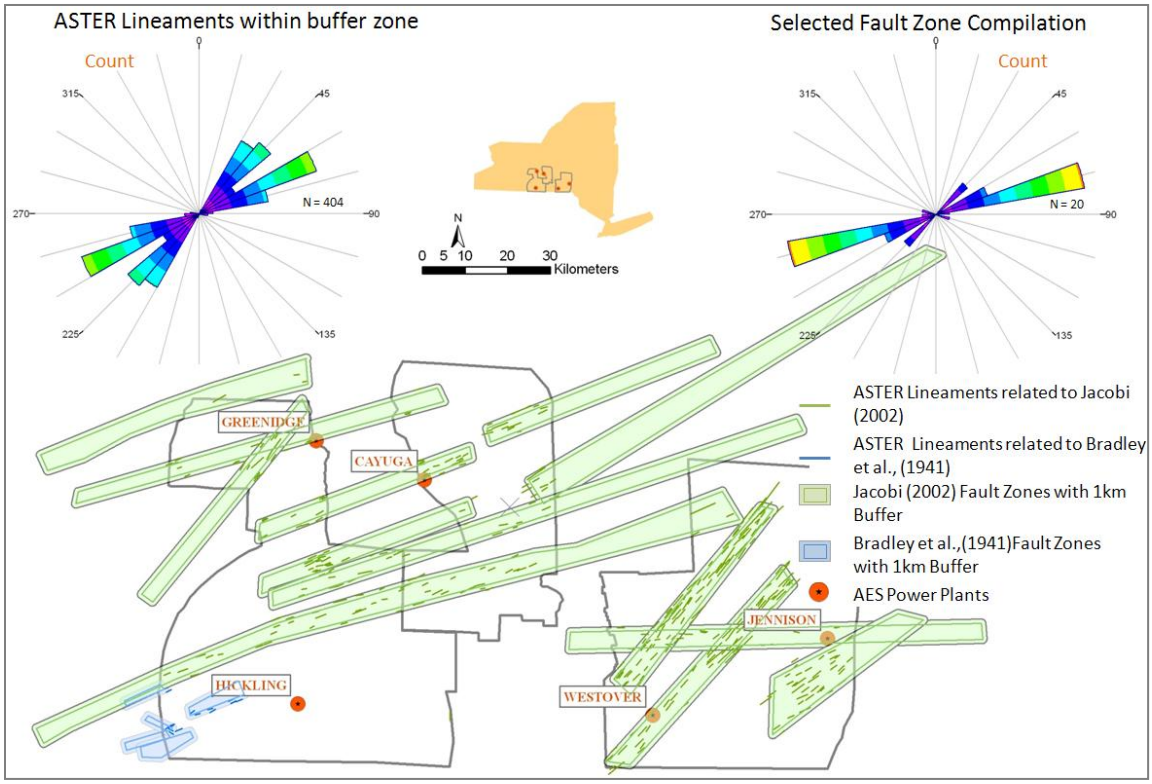

Figure 6.4,5&6-109. Map of the project area with selected Bradley et al., (1941) and Jacobi (2002) fault zones (all with 1 km buffer) and selected ASTER lineaments that intersect the buffers and are oriented with 20^0 of the fault zone trend. From Zelazny et al. (2010) and Zelazny (2011).

Stratigraphic Analysis. The stratigraphic units exposed in the project area (the Devonian Hamilton, Tully, Genesee, Sonyea and West Falls groups) recorded at least one major orogenic event – the Alleghanian Orogeny. Tectonic stresses associated with this orogeny and more recent events varied across the Appalachian Basin (e.g., Engelder and Geiser, 1980). In addition, unique lithologies can have a different response to stress, compared to typical units in the section. The burial conditions that include pressure and temperature, as well as fluid migration, can vary over time, across the basin, and of course, upsection. Thus, whether the stratigraphic units display the same structural features upsection and across the project area should be tested. This analysis examines the local stratigraphy to identify minor lineament orientation variations using rose diagrams for the following three stratigraphic units based on the geologic map of Isachsen et al. (1991): (1) Hamilton Group (2) Tully, Genesee and Sonyea groups (considered as a single group) and (3) West Falls Group exposed in the project area.

The digitized lineaments were divided into the three stratigraphic units. Rose diagrams of lineament orientations were constructed for each of the three stratigraphic layers: (1) the Hamilton Group with a total

of 336 lineaments, (2) the Tully Ls, Genesee and Sonyea groups had a total of 4,217 lineaments and (3) the West Falls Group had a total of 3,267 lineaments (Figure 6.4,5&6-110 and Table 6.4,5&6-13)

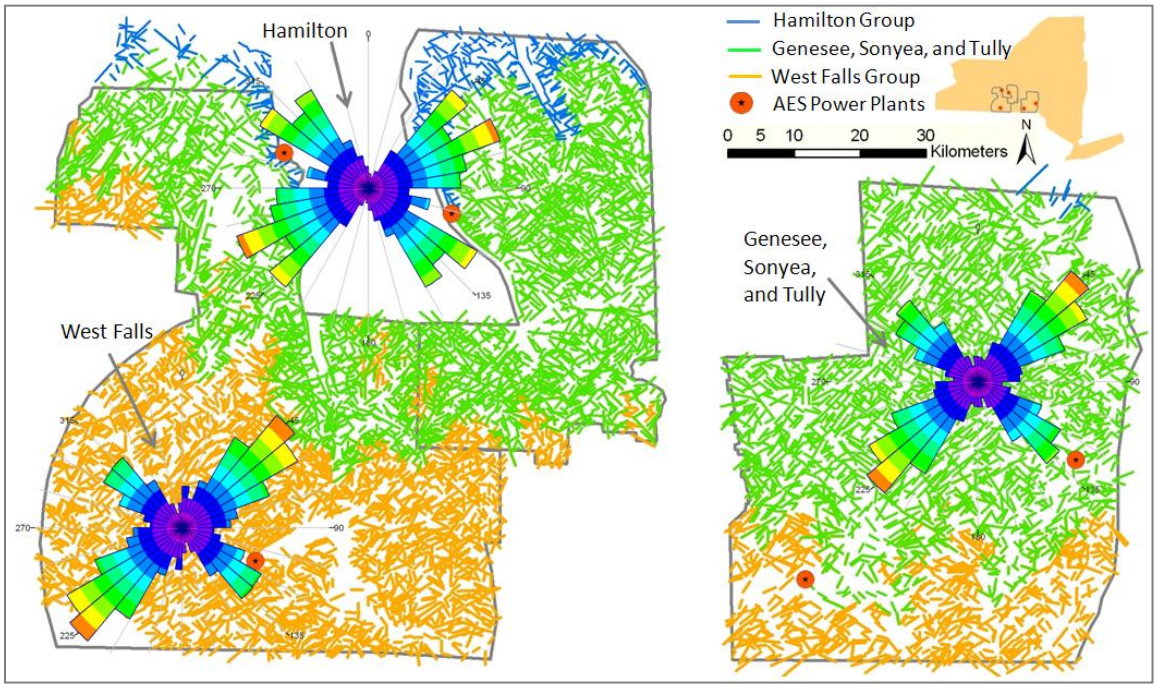

Figure 6.4,5&6-110. ASTER lineaments within different geologic units (Hamilton, Tully, Genesee, Sonyea and West Falls) with different colors corresponding to the different units: Hamilton Group (blue), Tully, Genesee and Sonyea groups (green) and West Fall Group (orange). Rose diagrams of lineament orientations are also shown. From Zelazny (2011).

	Primary Trend	Secondary Trend
Project Area		
Hamilton Group	ENE (65°)	NW (305°)
Genesee, Sonyea and Tully	NE (45°)	NW (315°)
West Falls Group	NE (45°)	NW (310°)

Table 6.4,5&6-13. Primary and secondary trends of ASTER digitized lineaments for the each of the geological groups in the stratigraphic analysis.

The stratigraphically and structurally lowest group in the project area, the Hamilton Group, has a much smaller footprint in the project area compared to the other two. The Hamilton Group has a primary mode at 63° (ENE) with a secondary mode of 45° (NE) and a third at 305° (NW). The Genesee, Sonyea and Tully rose diagram and West Falls rose diagram have a primary mode at 45° (NE) and the secondary mode at

310° (NW). The West Falls group also has a mode at 5° (N), unlike the other two groups; this northerly trend is a result of the large area of West Falls outcrop in the western focus area where northerly trending faults and associated valleys occur. The 63° (ENE) trend in the Hamilton data could reflect Set III (J1) fractures in the Marcellus. The remainder of the modes in all three groups (NE and NW) is consistent with the similarities the Hamilton, Tully, Genesee, Sonyea and West Falls groups share in lithology and tectonic history. A detailed division of the units into formation rank might reveal more significant differences in associated lineaments, since the black shales carry different patterns of fractures from the overlying gray shales and interbedded silts/sands.

Comparison to Previous Work (Subtask 6.6)

Lineaments from the present project were compared to previous lineament studies (e.g., Isachsen and McKendree, 1997; EarthSat, 1997; Cruz et al., 2005; and Cruz, 2005) that were conducted in the same region. The orientation modes of the various previous and current lineament studies are compiled in Table 6.4,5&6-14 and displayed as maps and rose diagrams for the entire project area and the three focus areas (Figures 6.4,5&6-111 to 6.4,5&6-120). A map with the EarthSat (1997), Isachsen and McKendree (1977) and the

	Primary Trend	Secondary Trend
Project Area		
ASTER Lineaments	NE (45°)	NW (310°)
EathSat (1997)	ENE (75°)	NS (350°)
Isachsen and McKendree (1977)	NNW (345°)	NE (35°)
Western Focus Area		
ASTER Lineaments	NE (45°)	NW (305°)
EathSat (1997)	ENE (75°)	NNE (15°)
Isachsen and McKendree (1977)	NE (35°)	NS (350°)
Central Focus Area		
ASTER Lineaments	NE (50°)	NW (315°)
EathSat (1997)	ENE (75°)	NS (355°)
Isachsen and McKendree (1977)	NE (35°)	NNW (345°)
Eastern Focus Area		
ASTER Lineaments	NE (45°)	NW (305°)
EathSat (1997)	NE (45°)	NNW (345°)
Isachsen and McKendree (1977)	NS (355°)	NE (45°)

Table 6.4,5&6-14. Primary and secondary trends of lineaments in both project area and focus areas from the present project's ASTER images, EarthSat (1997) and Isachsen and McKendree (1977).

present project's ASTER lineaments aided in the understanding of the variations in length, orientations and locations of lineaments identified in the project area (Figure 6.4,5&6-111). The EarthSat (1997) and Isachsen and McKendree (1977) datasets were available for the entire project area, which resulted in a meaningful comparison with the present lineament study. In order to compare the lineaments digitized by Cruz et al. (2005), which covered a small region around Seneca Lake, a subset of the ASTER digitized lineaments was generated (Figure 6.4,5&6-120). It was difficult to gather a relationship between Cruz et al. (2005) and the ASTER digitized lineaments because of the limited region of overlap in the datasets.

A significant difference between the present project's ASTER digitized lineaments and the lineaments from other studies, regardless of orientation, is the consistently shorter length of ASTER lineaments. This can be explained by variations in the digitizing scales, however this information is unknown or unpublished for both EarthSat (1997) and Isachsen and McKendree (1977) lineaments.

Lineament trends from EarthSat (1997), Isachsen and McKendree (1977) and ASTER (this study) are the most similar in the eastern focus area (Figures 6.4,5&6-115 and 6.4,5&6-119). The primary trend of both ASTER and EarthSat (1997) are identical at NE (45°) (Figure 6.4,5&6-115), and are identical to a secondary NE (45°) trend in Isachsen and McKendree's (1977) data (Figure 6.4,5&6-119). The primary orientation mode for Isachsen and McKendree in the eastern focus area is NS (355°; Figure 6.4,5&6-119), which is similar to the secondary NNW (345°) trend in the EarthSat (1997) lineaments (Figure 6.4,5&6-115), but this northerly trend does not appear in the ASTER lineaments of this project.

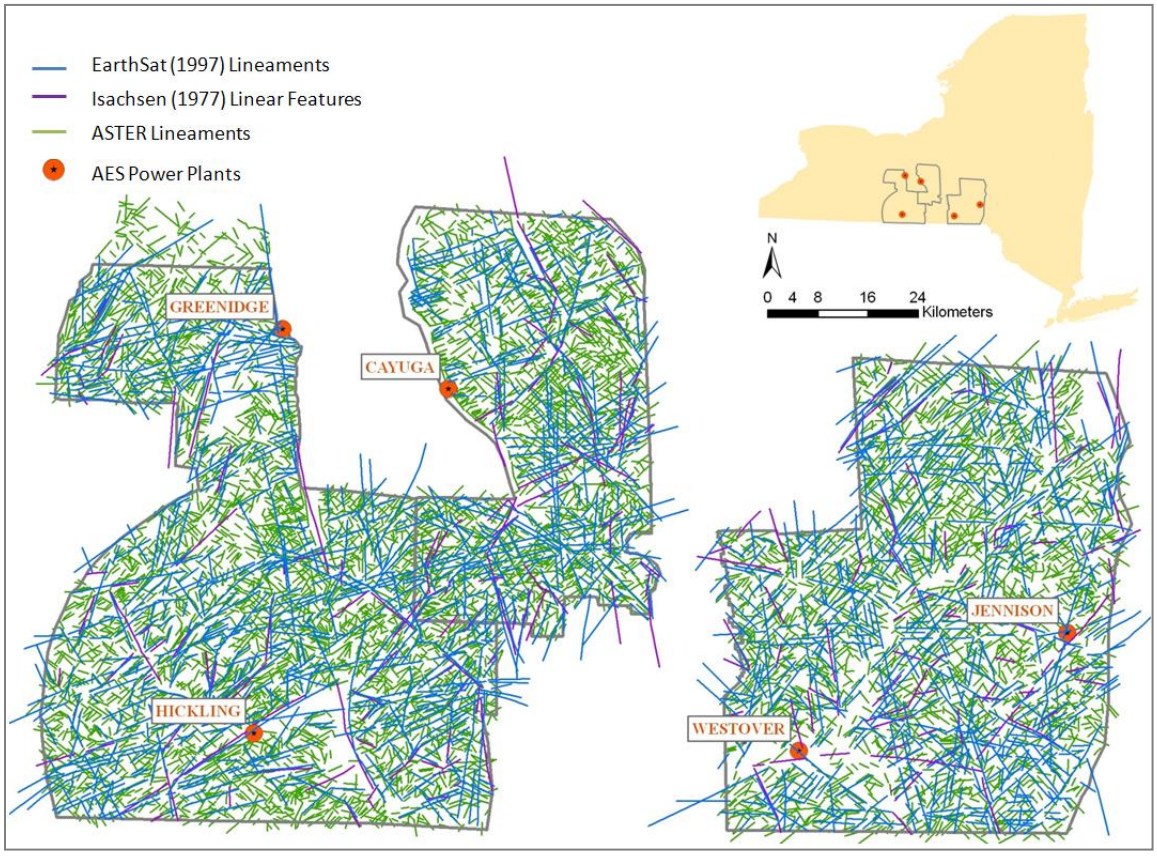

Figure 6.4,5&6-111. EarthSat (1997) lineaments, Isachsen and McKendree (1977) linear features and ASTER lineaments from this project. From Zelazny (2011).

The central focus area does not show strong similarities among the datasets of EarthSat (1997), Isachsen and McKendree (1977) and ASTER (this study, Figures 6.4,5&6-114 and 6.4,5&6-118). The primary trend of EarthSat (1997) is ENE, whereas the ASTER lineaments from the present study do not exhibit a strong ENE trend (as discussed above with respect to fractures). Furthermore, the secondary EarthSat (1997) orientation mode is north, also not observed in the ASTER rose diagram (Figure 6.4,5&6-115). However, some of the EarthSat (1997) northerly trending lineaments are coincident with ASTER north-trending lineaments, or areas where there is an absence of ASTER lineaments (Figure 6.4,5&6-114). Thus, the problem here is partly that 1) the NE- and NW-trending ASTER lineament are so numerous that they overwhelm the signal from the more rarely observed N-trending ASTER lineaments, and 2) the approaches to picking lineaments varied somewhat between operators at EarthSat (1997) and this report. A tertiary NW mode in the EarthSat (1997) data (Figure 6.4,5&6-114) does match the NW mode in the ASTER data.

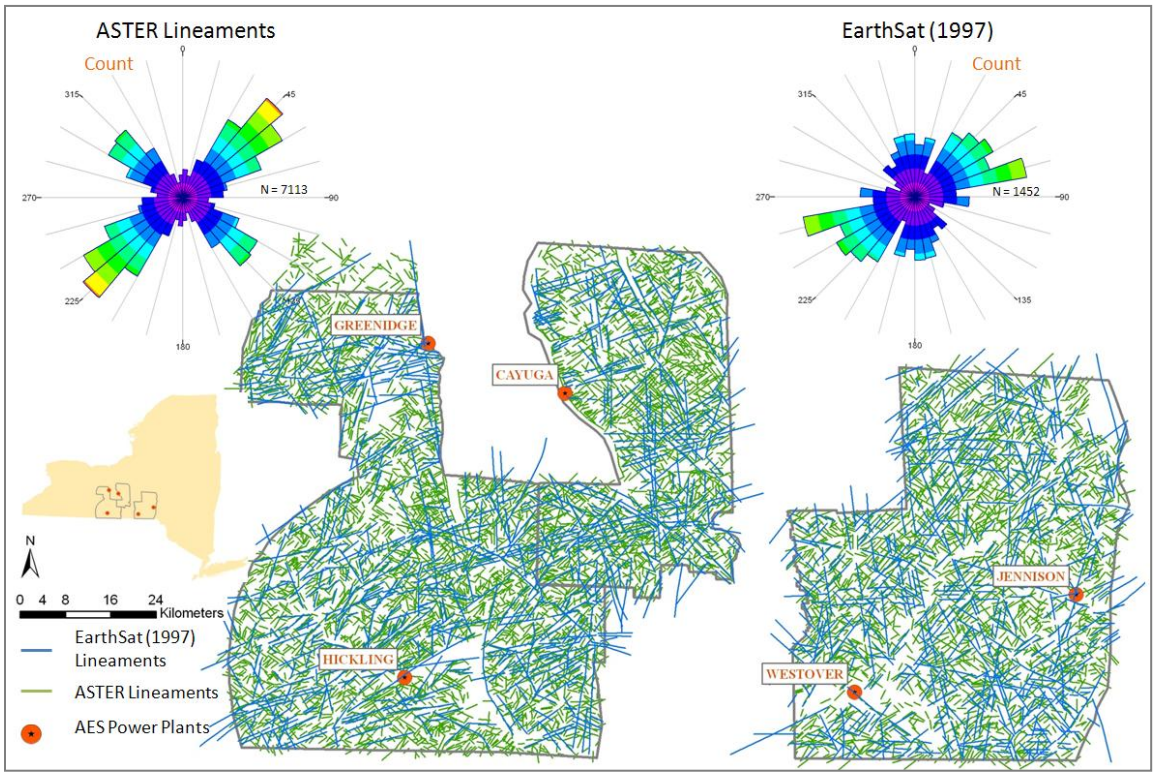

Figure 6.4,5&6-112. EarthSat (1997) and ASTER lineaments from this project for the entire project area; rose diagrams are based on count. From Zelazny (2011).

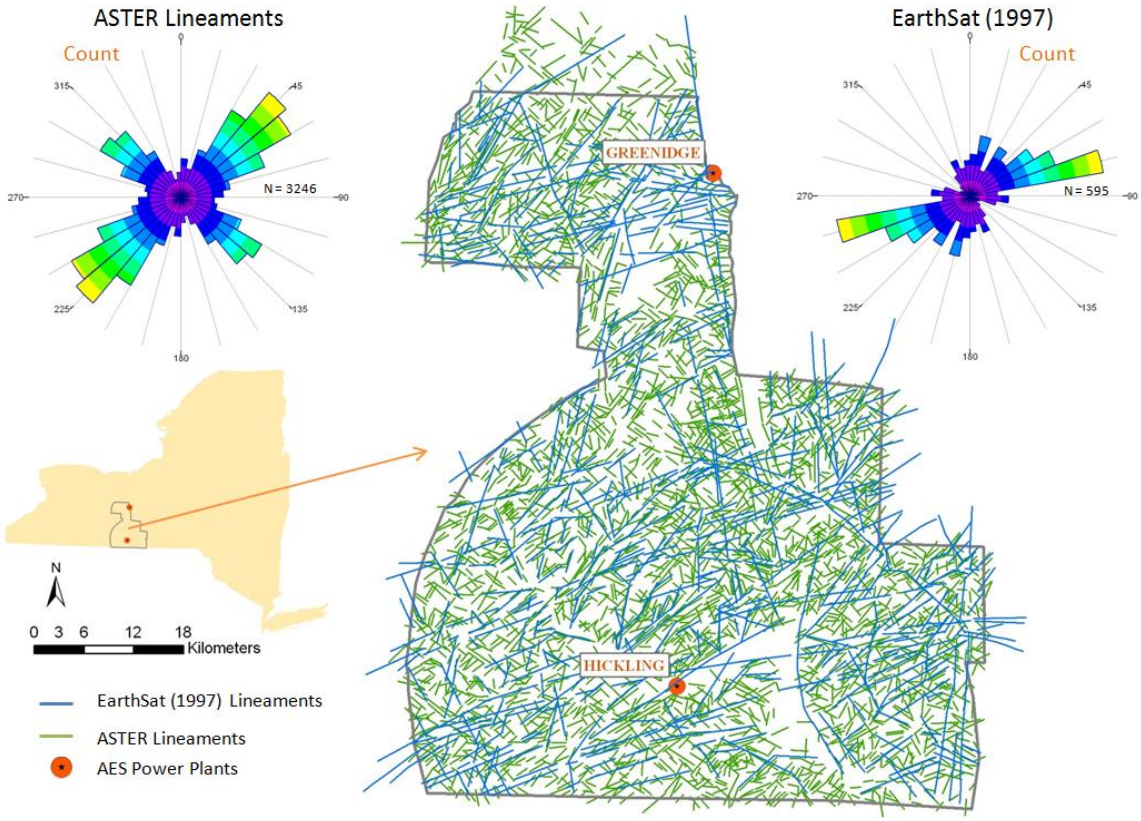

Figure 6.4,5&6-113. EarthSat (1997) and ASTER lineaments from this project for the western focus area; rose diagrams are based on count. From Zelazny (2011).

In the central focus area the Isachsen and McKendree (1977) and ASTER lineaments appear to share no significant trends, as portrayed in the rose diagrams (Figure 6.4,5&6-118). The primary mode of (nearly) NNE in the Isachsen and McKendree (1977) data does not significantly overlap the NE trend in the ASTER data, and the NNW Isachsen and McKendree (1977) mode is clearly not related to the NW ASTER trend in the rose diagrams (Figure 6.4,5&6-118). However, like the lineaments in the eastern focus area, inspection of Figure 6.4,5&6-118 reveals that several of Isachsen and McKendree's (1977) NNW and ENE lineaments are coincident with shorter ASTER lineaments. Apparently, the large number of NE and NW ASTER lineaments again overwhelms the much more modest number of NNW and NNE-trending lineaments in the rose diagrams.

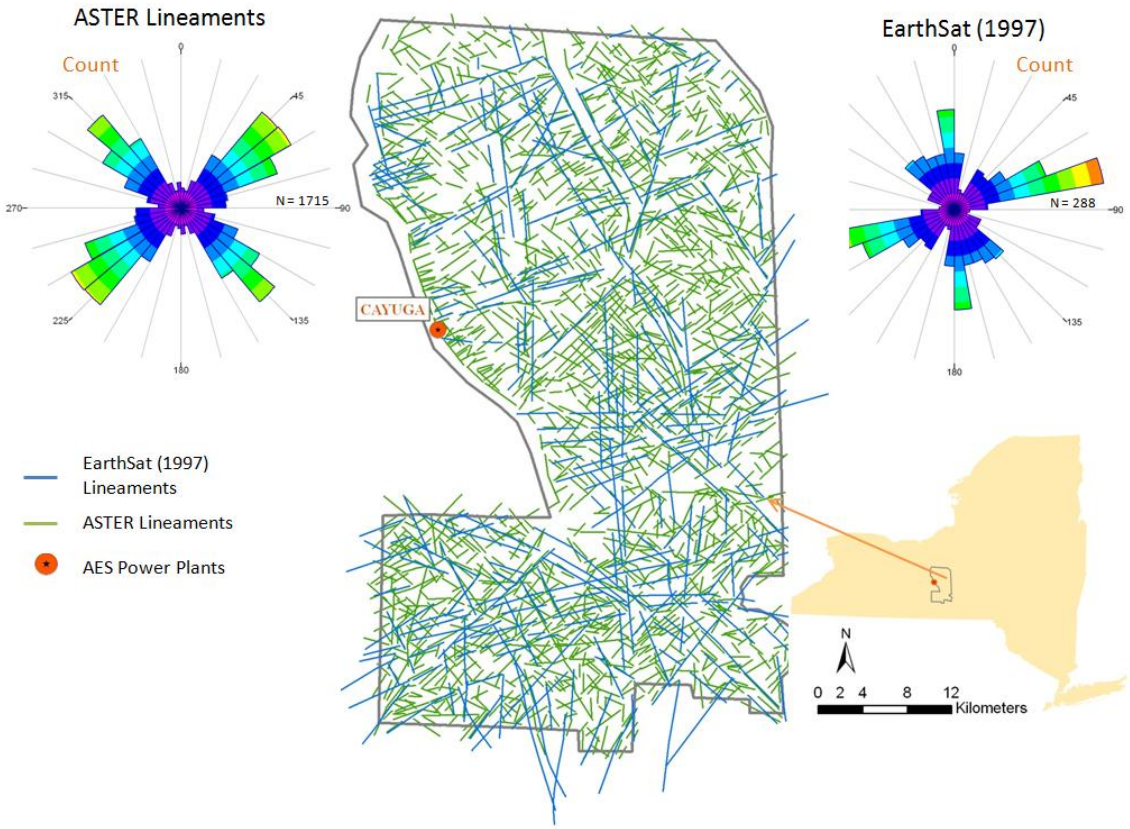

Figure 6.4,5&6-114. EarthSat (1997) and ASTER lineaments from this project for the central focus area; rose diagrams are based on count. From Zelazny (2011).

The western focus area shows only some similarities between the lineament trends determined by the different lineament datasets of EarthSat (1997), Isachsen and McKendree (1977) and ASTER (this study, Figures 6.4,5&6-113 and 6.4,5&6-117). The EarthSat (1997) lineaments have an ENE primary mode, whereas the ASTER data has a NE mode (Figure 6.4,5&6-113). The secondary ASTER mode of NNE is also not a mode in the ASTER data. Never the less, specific ENE-, NNE-, and NNW/N-trending EarthSat (1997) have coincident, but shorter ASTER lineaments (Figure 6.4,5&6-113). The primary orientation mode of Isachsen and McKendree's (1977) lineaments is close to that of the ASTER NE primary mode (Figure 6.4,5&6-117). However, the N Isachsen and McKendree (1977) mode is not observed in the ASTER rose diagram, and the strong secondary NW ASTER mode is nearly non-existent in the Isachsen and McKendree's (1977) data. However, like the other areas, examination of specific Isachsen and McKendree's (1977) lineaments in the western focus area (Figure 6.4,5&6-117) show coincident, but shorter ASTER lineaments.

The small area and small number of lineaments in the Cruz et al. (2005) and Cruz (2005) lineaments make any comparison between the ASTER lineaments and the Cruz (2005) lineaments suspect (Figure 6.4,5&6-120). However some of Cruz (2005) lineaments are coincident with ASTER lineaments (Figure 6.4,5&6-120).

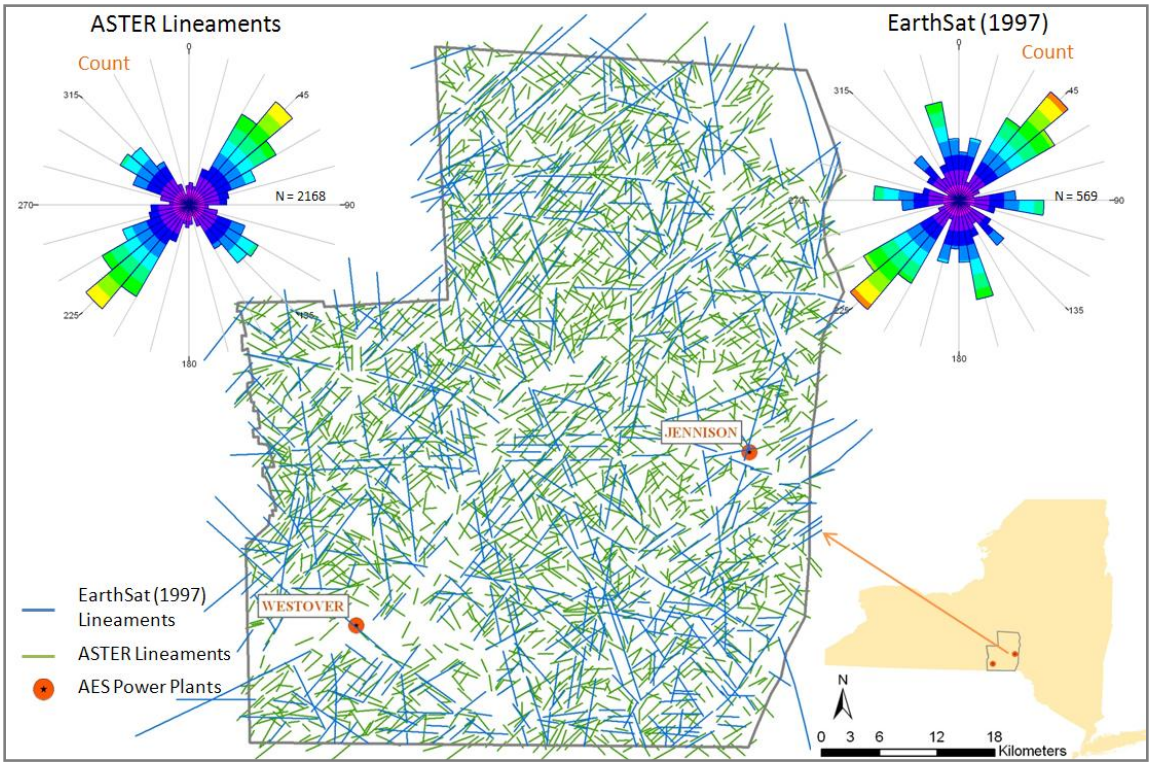

Figure 6.4,5&6-115. EarthSat (1997) and ASTER lineaments from this project for the eastern focus area; rose diagrams are based on count. From Zelazny (2011).

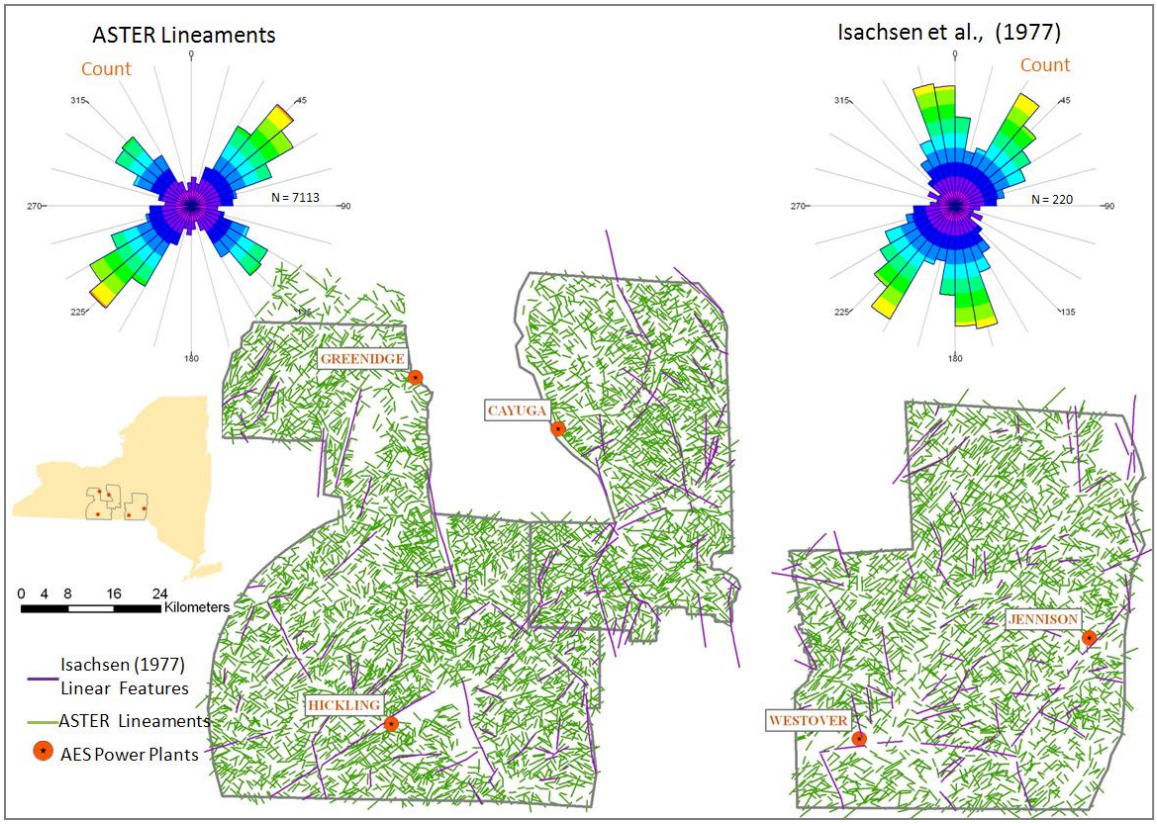

Figure 6.4,5&6-116. Isachsen and McKendree (1977) linear features and ASTER lineaments from this project for the entire project area; rose diagrams are based on count. From Zelazny (2011).

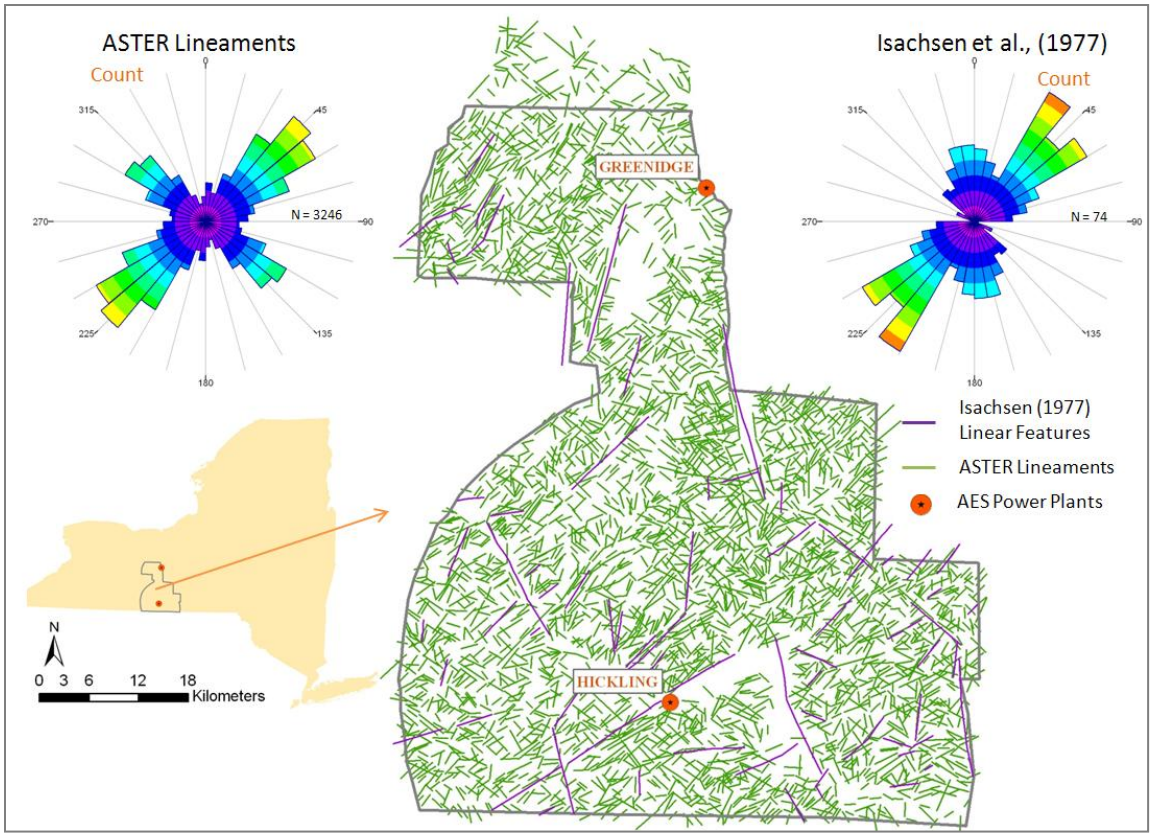

Figure 6.4,5&6-117. Isachsen and McKendree (1977) linear features and ASTER lineaments from this project for the western focus area; rose diagrams are based on count. From Zelazny (2011).

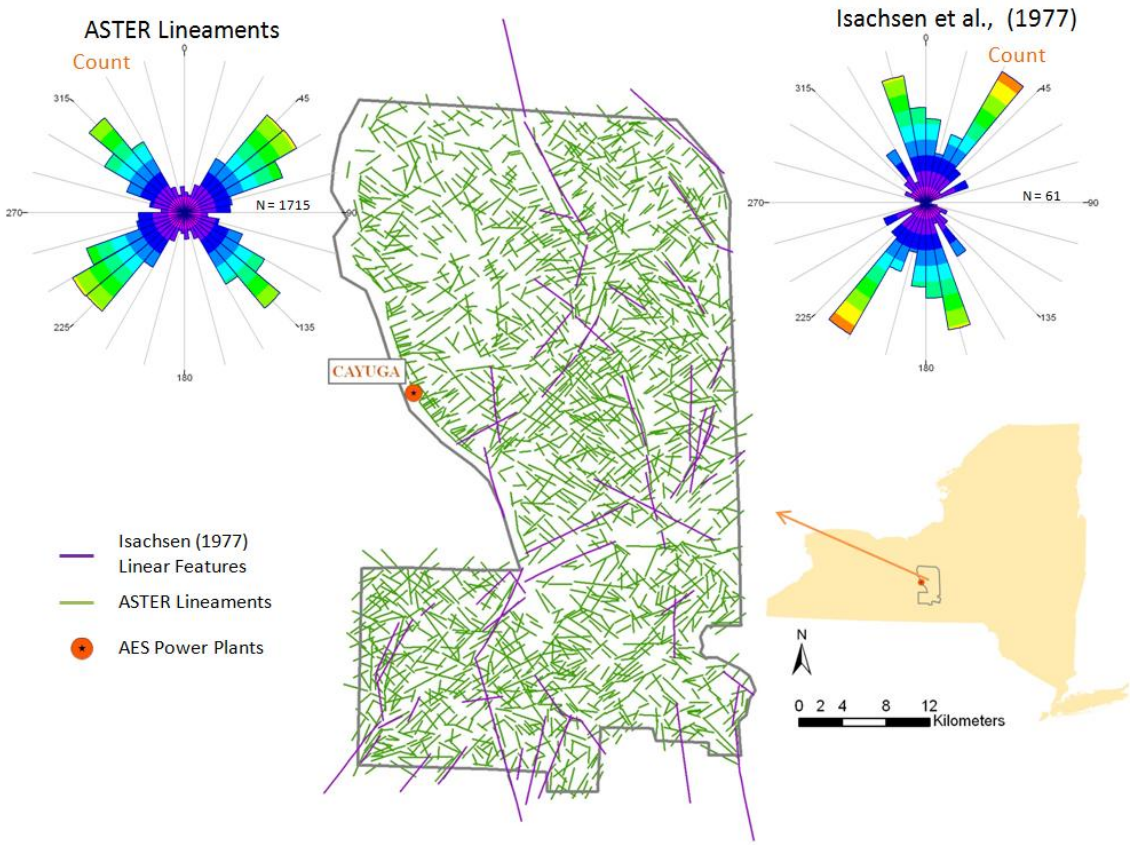

Figure 6.4,5&6-118. Isachsen and McKendree (1977) linear features and ASTER lineaments from this project for the central focus area; rose diagrams are based on count. From Zelazny (2011).

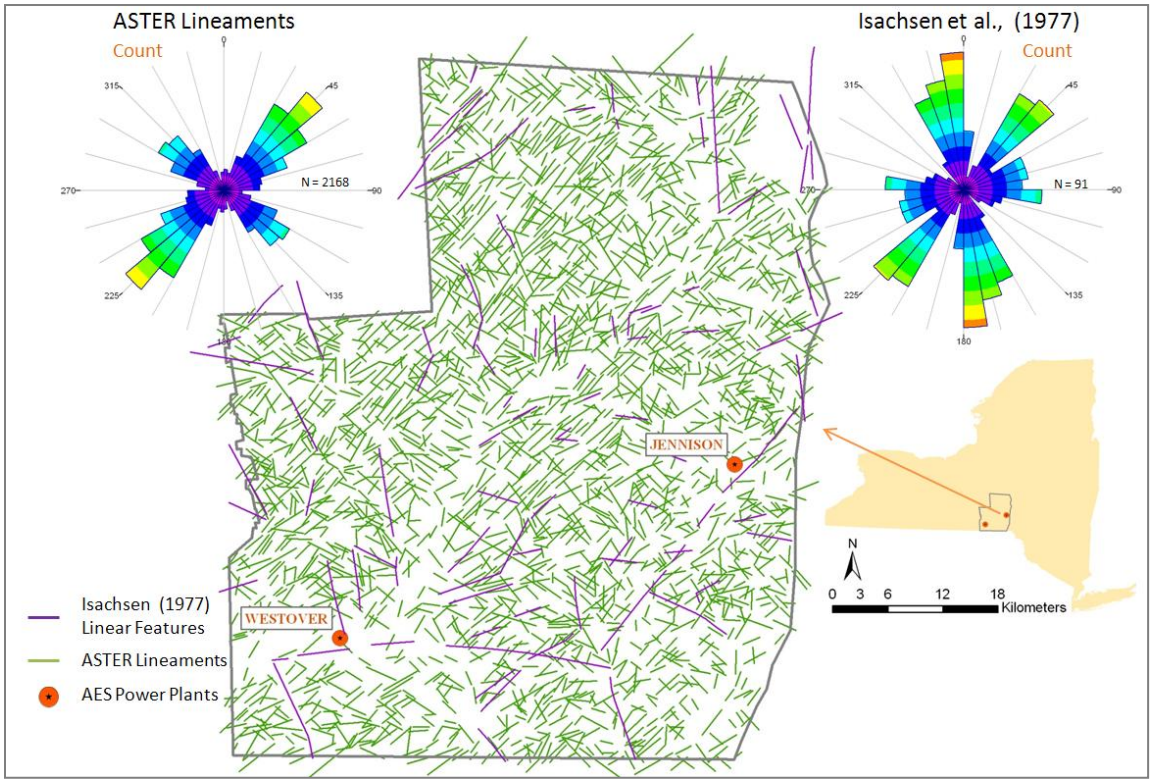

Figure 6.4,5&6-119. Isachsen and McKendree (1977) linear features and ASTER lineaments from this project for the eastern focus area; rose diagrams are based on count. From Zelazny (2011).

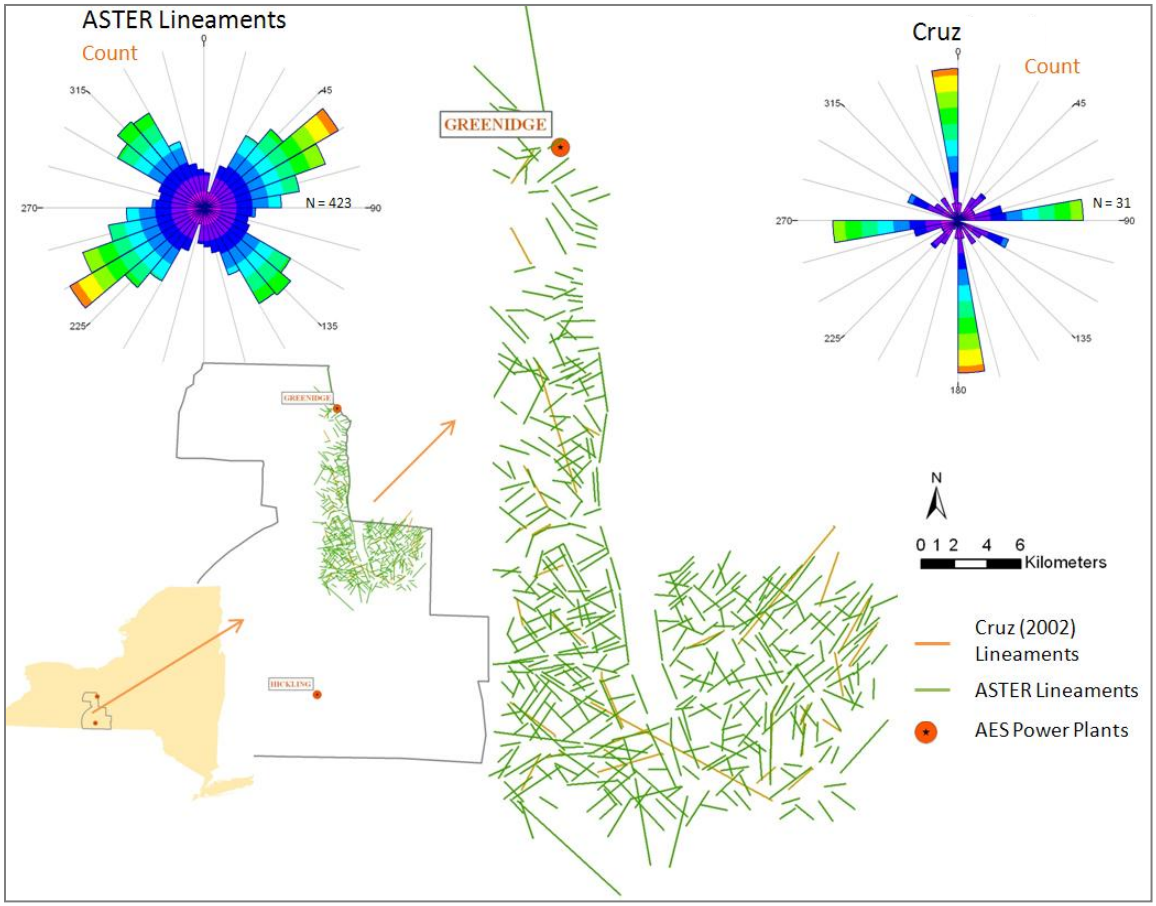

Figure 6.4,5&6-120. Map of the Seneca Lake region showing all Cruz (2005) lineaments and ASTER lineaments from this project and rose diagrams based on count. After Zelazny (2011).

DISCUSSION (INCLUDES SUBTASK 6.7)

The goals of this research were to identify lineaments in order to determine the fracture fabric in the project area, in terms of both the orientation and density of fractures, and to determine the possible location and trend of faults. Such goals seemed possible since previous lineament studies had indicated that faults could be ascertained from the lineament data (e.g., Isachsen and McKendree, 1997; EarthSat, 1997; Jacobi, 2002; 2007a, b; Cruz et al., 2005; and Cruz, 2005). The goal was to use more sophisticated imagery than had been available in the past. Rigorous controls were placed on the lineament identification process (including weekly QC checks of the operator picking the lineaments) in order to assure that the level of lineament recognition remained constant across the project area.

As detailed in the preceding sections, the primary lineament trends that were digitized at a scale of 1:125,000 are NE and NW in both ASTER and DEM images across the entire project area. The digitized

ASTER lineaments have a primary orientation set of NE (45°), a secondary orientation of NW (315°) and a less pronounced trend at EW (90°; Figure 6.4,5&6-48). Rose diagrams, based on both the total count and cumulative length, revealed similar trends. Similarly, the primary trend of lineaments digitized from the shaded relief DEM is NE (35°) and the orientation of the secondary set is NW (330°; Figure 6.4,5&6-49). In the more detailed Cayuga subset where lineaments were digitized at a scale of 1:25,000, the ASTER lineament trends are similar to those in the project area as a whole; the primary trend of the ASTER lineaments is NE (55°) with the secondary trend of NW (315°; Figure 6.4,5&6-47). The secondary orientation mode of the DEM lineaments (NE, 60°) is very similar to the ASTER lineament mode, but the primary orientation mode is noticeably different at NNW (340°).

In detail the DEM lineament orientations deviate from the ASTER lineament orientations across the project area. The orientations of DEM lineaments exhibit relatively large variations in orientation compared to the tight grouping of lineament trends seen in the ASTER rose diagrams. The DEM lineaments have the tightest grouping of orientations in the eastern focus area, with a primary trend of NE (35°) and a rose diagram that is most similar to ASTER rose diagrams. In contrast the DEM lineaments have a relatively wide spread of orientations in western and central focus areas. These variations in rose diagrams suggest that different features contribute to the mix of lineaments in the DEMs compared to the ASTER images. Unrecognized glacial features may be more readily identified as lineaments in the DEM images.

The overall NE and NW lineament trends in all the data sets are compelling. The prevalence and the orthogonality of the dominant lineaments might suggest that they delineate the fracture fabric for the entire project area. However, in the eastern focus area, the NE and NW lineament trends do not correlate with the observed fracture set trends: Set II fractures strike WNW and Set I fractures strike NNE/N. Set III (J1) fractures that strike ENE (65^0) do occur in the eastern focus area as well (Figures 6.4,5&6-8 and 6.4,5&6-9; Terech et al. (2005) and Terech (2006), McGuire et al. (2006), McGuire (2007), and from Jacobi (2007b), but this trend also is not the distinctly NE trend of the lineaments. In fact the lowest numbers of fracture strikes observed in outcrops in the eastern focus area correspond to the modes of lineament orientations in the eastern focus area. Clearly, the fracture fabric Set I and II is not represented by the overall NE and NW lineament trends in the eastern project area. What do the NE and NW lineaments in the eastern project area represent?

Farther west in the central focus area, the same problem exists: what do the NE and NW lineaments represent? In the central focus area the fracture orientation modes (in the first quadrant) are ENE and EW, as found by Engelder and Geiser (1980; Figure 6.4,5&6-6) and the later detailed studies (e.g., Jacobi, 2007b), distinctly not the lineament trend of NE. Thus, NE lineament trend clearly does not represent the general orthogonal Alleghanian fracture fabric measured in the field. In the western focus area, although Set I and Set II fractures have rotated to orientations more compatible with the lineament orientations than

in the central and eastern focus areas, the NE and NW-trending lineaments remain distinctly mis-oriented with respect to the general Set I and set II fracture trends.

These dichotomies in general trend between the lineaments and general fracture trends do not negate the fact that locally, fractures in outcrop coincide with lineament trends at the same buffered locations (e.g., Figures 6.4,5&6-98 to 6.4,5&6-101). However, it is clear that if the general NE-NW lineament fabric represents a single set of structural features across the entire project area, the NE-NW lineament fabric cannot represent the Set I and set II fractures that arc across the project area.

In the central and western focus areas, some of the basement faults proposed on the basis of aeromagnetic anomalies strike NE (Figure 6.4,5&6-103; Jacobi, 2007a). In the eastern focus area, previously proposed faults also strike NE; although these faults were based primarily on lineaments, some are consistent with faults observed on 2D and 3D proprietary seismic data. Also, the secondary mode at about 60^0- to 65^0 that contributes to the apparent strong NE mode in all the lineament histograms (Figures 6.4,5&6-47 to 6.4,5&6-51), and is strongest in Figures 6.4,5&6-49 to 6.4,5&6-51, could be attributed to the population of ENE-striking fractures (Set III, or J1). Thus, it may be that the NE-NW general lineament fabric is a result of fractures associated with fault systems, combined with J1 fractures.

The lack of a clear understanding of the NE-NW lineament fabric does not negate the usefulness of the lineaments for fault delineations. Two points need to be made concerning fault inferences from the present lineament data.

1) Faults can be recognized in the strings of linked density highs in the filtered density data (e.g., Figure 6.4,5&6-79). Some of these strings coincide with fault systems that have already been recognized or proposed. For example, the ENE-striking faults in the southern parts of the western and eastern focus areas are recognizable by ENE-trending strings of high density in the DEM filtered data (Figure 6.4,5&6-80 and see also Figure 6.4,5&6-103). Other proposed fault systems that can be recognized in the strings of high density in the ASTER and DEM filtered lineament data include the northerly (N and NNW) and easterly striking faults near the Finger Lake shores (e.g., Figures 6.4,5&6-68 and 6.2-65 respectively for ASTER, and Figures 6.4,5&6-102 and 6.4,5&6-103 for proposed faults), and the NE-striking faults discussed above (e.g., Figure 6.4,5&6-107). In the project area relatively few NW-striking faults have been proposed (Figure 6.4,5&6-103), but these few do exhibit higher density zones in the filtered lineament data. For example, compare the high density zone of NW ASTER lineaments in the central region of the western boundary of the western focus area (Figure 6.4,5&6-67) with NW fault zones proposed by Jacobi (2007a) on the basis of aeromagnetics, and supporting EarthSat and DEM data (Figure 6.4,5&6-103).

2) A significant proportion of the proposed faults are not represented by sufficient lineaments to be recognized in the lineament data (such as some of Murphy's, 1981, N-striking faults, Figure 6.4,5&6-104). Thus, the presence of a density high string can be used to demonstrate the probability of a fault in the region of the string, but the absence of a density high string does not necessarily mean that the area is free from faults.

In terms of AES power plants, the density maps for all orientations of ASTER lineaments (Figures 6.4,5&6-55 and 6.4,5&6-62) show a high density at the Cayuga power plant, a relatively high density at the Greenidge power plant, and essentially no lineaments at the remaining three power plants because they are sited in broader valleys. These valleys may be considered lineaments, and may themselves indicate faulting. The density maps for all orientations of DEM lineaments (Figures 6.4,5&6-58 and 6.4,5&6-63) display similar density variations as the ASTER lineament density maps discussed above.

	Hickling	Greenidge	Cayuga	Westover	Jennison
Density maps for all ASTER lineaments	no data, but probably high	medium	high	no data, but probably high	no data, but probably medium
Density maps for all DEM lineaments	no data, but probably high	medium	high	no data, but probably high	no data, but probably medium
ASTER filter EW	medium	medium	NO	NO	low
ASTER filter WNW	medium	NO	NO	high-near string	medium
ASTER filter NW	high-near string	high-string	high-string	NO	medium
ASTER filter NNW	NO	high-string	high-string	NO	NO
ASTER filter NS	NO	NO	NO	NO	low
ASTER filter NNE	NO	NO	NO	NO	NO
ASTER filter NE	high-strings	medium	high	low, but near strings	low
ASTER filter ENE	near string	low	high	no	high-string
DEM filter EW	NO	low	NO	medium-near longer strings	NO
DEM filter WNW	NO	NO	NO	medium-near longer strings	NO
DEM filter NW	low	low	High	low	low
DEM filter NNW	NO	NO	high-string	NO	low
DEM filter NS	low	low	NO	NO	low
DEM filter NNE	NO	low	NO	NO	high-string
DEM filter NE	NO, but near strings	high-string	medium	medium-near longer strings	
DEM filter ENE	high-strings	low	medium-high	low, but near string	NO
Isachsen & McKendree (1977)	high	NO	NO	high	high
EarthSat (1997) lineaments	high	high	high	high	high
Murphy (1981) flts	high	high	NO		
Isachsen et al flts	high	high	NO	NO	NO
Jacobi (2007a) flts	high	high	high		high
Jacobi (2007b) flts					
Jacobi (2002) flt zns	high		high	high	high

Table 6.4,5&6-15. Summary of AES power plant locations with respect to lineaments and proposed faults. "High" in the table indicates "high density" for the lineaments and indicates high probability of a (proposed) fault for the other studies. "String" indicates linked high density zones forming a linear element. Yellow indicates 'high" density and tan indicates a possible "high" density.

The implications of the lineament analyses for potential CO_2 subsurface sequestration near the AES power plants can be summarized as the following: in each analysis of lineament data, it appears that most, or all, of the AES power plants in central NYS are close to a relatively high density of lineaments that might indicate fault systems (Table 6.4,5&6-15). Furthermore, some power plants are near known faults or fault systems that are associated with lineaments (e.g., Hickling and Greenidge, Figures 6.4,5&6-103 and 6.4,5&6-104). Thus, it is necessary for any Phase II CO_2 subsurface sequestration research to include a 3D seismic survey in the region of proposed detailed study (such as an injection test well) to determine the extent of the faulting. A horizontal well with an FMI log to determine the details of the fault or fracture character is also critical.

CONCLUSIONS

ASTER, Landsat and DEM images were processed and tested to determine which processing techniques and resulting images delivered optimum imagery for lineament identification in the project area in central New York State. Lineaments were identified and digitized from ASTER and DEM images across the project area. Analyses of the lineaments included determining the spatial density of all the lineaments, as well as the density of "filtered" lineaments—those of a particular orientation. The present lineament data was also tested against previous lineament studies in the same region and against previously published fracture data and proposed/observed faults.

The primary lineaments that were identified and digitized at a scale of 1:125,000 trend NE and NW in both ASTER and DEM images across the entire project area. In the more detailed Cayuga subset where lineaments were digitized at a scale of 1:25,000, ASTER lineament trends are similar to those in the project area as a whole. The overall NE and NW lineament trends in all the present data sets are compelling. The NE and NW lineament trends do not correlate with the observed fracture Sets I and II trends across the entire project area. The lineament source(s) remains unidentified, but the NE lineament trends are similar to the trend of faults that affect basement, based on aeromagnetic anomalies. It may be that the NE-NW general lineament fabric is a result of fractures associated with fault systems, combined with Set III fractures. Locally, fractures in outcrop coincide with lineament trends at the same buffered location, but the general NE-NW lineament fabric does not represent the Set I and set II fractures that arc across the project area.

Faults can be recognized in the strings of linked density highs in the filtered density ASTER and DEM data. Some of these strings coincide with fault systems that have been previously recognized or proposed. However, a significant proportion of the proposed faults are not represented by sufficient lineaments to be recognized in the lineament data. Thus, the presence of a density high string can be used to demonstrate the

probability of a fault in the region of the string, but the absence of a density high string does not necessarily mean that the area is free from faults.

The implications of the lineament analyses for potential CO_2 subsurface sequestration near the AES power plants can be summarized as the following: in each analysis of lineament data, it appears that most, or all, of the AES power plants in central NYS are close to a relatively high density of lineaments that might indicate fault systems. Furthermore, some power plants are near known faults or fault systems that are associated with lineaments (e.g., Hickling and Greenidge). Thus, it is necessary for any Phase II CO_2 subsurface sequestration research to include a 3D seismic survey in the region of proposed detailed study to determine the extent of the faulting.

REFERENCES

Abrams, M., 2000, The Advanced Spaceborne Thermal Emission and Reflection Radiometer (ASTER): data products for high spatial resolution imager on NASA's Terra platform: Int. Journal of Remote Sensing, v. 21, no. 5, p. 847 - 859.

Bradley, W. H., Pepper, F., J., and Richardson, G. B., 1941, Geologic Structure and occurrence of gas in part of southwestern New York: United States Geological Survey v. Bulletin 899, p. 93.

Brett, C.E., Bartholomew, A.J. and Baird, G.C, 2007, Biofacies recurrence in the Middle Devonian of New York State: An example with implications for habitat tracking: Palaios, v. 22, p. 306-324.

Broughton, J. G., Fisher, D. W., Isachsen, Y. W., and V., R. L., 1966, Geology of New York: a short account: Albany, New York State Museum and Science Service.

Cruz, C. A., 2005, Satellite image enhancements, lineament identification and quantitative comparison with fracture data, Central New York State [MS thesis]: SUNY University at Buffalo, 127 p.

Cruz, C., Jacobi, R. D., Everett, J. R., and Staskowski, R. J., 2005, ASTER and Landsat lineaments in central NYS: Image processing and groundtruthing for fractures, *in* Geological Society of America, Abstracts with Programs, p. 58.

Drechsel, C. A., Jacobi, R. D., Everett, J. R., and Staskowski, R. J., 2004, ASTER lineaments, faults, and reservoirs in the Appalachian Basin of New York State, Geological Society of America, Abstracts with Programs, p. 146.

EarthSat (Earth Satellite Corporation), 1997, Assessing the contribution of satellite hyperspectral data to petroleum exploration. New York State Energy Research and Development Authority (NYSERDA) (Albany, New York), 35 pp.

Engelder, T., and Geiser, P., 1979, The relationship between pencil cleavage and lateral shortening within the Devonian section of the Appalachian Plateau, New York: Geology, v. 7, p. 460 to 464.

Engelder, T., and Geiser, P., 1980, On the Use of Regional Joint Set as Trajectories of Paleostress Fields During the Development of the Appalachian Plateau, New York: Journal of Geophysical Research, v. 85, no. B11, p. 6319 - 6341.

Engelder, T., and Lash, G. G., 2008, Marcellus Shale play's vast resource potential creating stir in Appalachia: American oil and Gas Reporter, May edition, 7 pp.

Engelder, T., and Whitaker, A., 2006, Early jointing in coal and black shale: Evidence for an Appalachian-wide stress field as a prelude to the Alleghanian orogeny: Geology, v 34, p. 581-584.

Ettenshon, F.R., and Barron, L. S., 1981, Depositional Model for Devonina-Mississippian Black-Shale sequence of North America: A Tectono-Climatic Approach: United States Department of Energy (Morgantown, WV) Report, 85 pages.

Everett, J. R., Staskowski, R. J., and Jacobi, R. D., 2003, Fracture and satellite hyperspectral analysis for petroleum exploration: World Oil, no. Nov 2003, p. 44-47.

Everett, J. R., Staskowski, R. J., and Jacobi, R. D., 2004, Geochemical indications of fractured carbonate reservoirs in New York from ASTER data, *in* American Assoc. Petrol. Geol, p. A43.

Fernandes da Silva, P. C., Cripps, J. C., and Wise, S. M., 2005, The use of Remote Sensing techniques and empirical tectonic models for inference of geological structures: Bridging from regional to local scales: Remote Sensing of Environment, v. 96, no. 1, p. 18-36.

Fisher, Jodi., Jacobi, Robert., Martin, John., 2010, Compilation of structural features in the northern Appalachian Basin of New York State to assist in site evaluation and CO2 sequestration: Geol. Soc. . Am. Abstracts with Programs, Vol. 42, No 1, p. 121

Fountain, J. C., and Jacobi, R. D., 2000, Detection of Buried Faults and Fractures using Soil Gas Analysis: Environmental & Engineering Geoscience, v. VI, no. 3, p. 201 - 208.

Hatcher, R. D., Jr., 2002, The Alleghanian (Appalachian) orogeny, a product of zipper tectonics: Rotational transpressive continent-continent collision and closing of ancient oceans along irregular margins, in Catalán, J. R. M., Hatcher, R. D., Jr., Arenas, R., and García, F. D., eds., Variscan-Appalachian dynamics: The building of the late Paleozoic basement: Geological Society of America Special Paper 364, p. 199-208

Hess, D. P., 2009, Using geospatial analysis to understand Laurentide Ice Sheet dynamics in New York State from landform morphometry and till fabric [Ph D thesis]: University at Buffalo, 89 p.

Holloway, S., 2005, Underground sequestration of carbon dioxide--a viable greenhouse gas mitigation option: Energy, v. 30, no. 11-12, p. 2318-2333.

Isachsen, Y. W., Landing, E., Lauber, J. M., Rickard, L. V., and Rogers, W. B., 1991, Geology of New York - Simplified Account Albany, NYS Museum Education Leaflet No. 50. 300 pp.

Isachsen, Y. W., and McKendree, W. G., 1977, Preliminary Brittle Structure Map of New York. Map and Chart Series No. 31, Niagara-Finger Lakes Sheet, one map.

Jacobi, R. D., 2002, Basement faults and seismicity in the Appalachian Basin of New York State: Tectonophysics, v. 353, no. 1-4, p. 75-113.

Jacobi, Robert D., 2007a, Final Technical Report (May 31, 2000-May 15, 2007): Innovative Methodology for Detection of Fracture-Controlled Sweet Spots in the Northern Appalachian Basin: Department of Energy/NETL, Morgantown, WV, 453 pp.

Jacobi, R. D., 2007b, Natural gas exploration in Chenango County, New York State: Economic development of stacked reservoirs: NYSERDA (Albany NY) Final report, 62 pp, 94 figures, and 30 tables

Jacobi, Robert, 2010, Geophysical and geological evidence for arcuate Iapetan opening rift faults in the Pennsylvania Salient and New York recess: implications for the ragged Laurentian margin: NYSERDA (Albany NY) Final Draft Report, 42 pp.

Jacobi, Robert D., 2011a, Faults in the Appalachian Basin of NYS: Geol. Soc. Am. Abstracts with Programs, http://gsa.confex.com/gsa/2011NE/finalprogram/abstract_185588.htm, accessed 9/15/2011

Jacobi, Robert, 2011b, Faults in the Appalachian Basin of New York State: AAPG Geosciences Technology Workshop, Success in the Marcellus and Utica Shales: Case Studies and New Developments: Baltimore MD, p. 3.

Jacobi, Robert D., 2011c, Integration of remotely-sensed and geophysical data with ground-truth structure: evidence for fault systems in part of Cayuga County: NYSERDA (Albany NY) Final report, 88 pp.

Jacobi, Robert D. and Fountain, John C, 2002, The character and reactivation history of the of the southern extension of the seismically active Clarendon-Linden Fault System, western New York State, *in* Neotectonics and Seismicity in the Eastern Great Lakes Basin, R. H. Fakundiny, R. D. Jacobi, and C. F. M. Lewis (eds.): Tectonophysics, v. 353, p.215-262.

Jacobi, R. D., and Zhao, M., 1996, Digital imaging and analyses of fractures: Evidence for Appalachian style tectonics in the Appalachian Plateau of western New York: Geol. Soc. Am., Abstracts with Programs, v. 28, n. 3, p. 67 (invited presentation)

Jacobi, Robert D., Fountain, John, Smith, Gerald, Tober, Beth, Loewenstein, Stuart, 2000, FIDs in the Appalachian Plateau of NYS: Indicators of faults and their motion histories, seismicity and hydrocarbon potential: Geol. Soc. Am., Annual Meeting Program, p. P-158

Jacobi, R. D., Eastler, T. E., and Xu, J., 2002, Methodology for remote characterization of fracture systems in enemy bedrock underground facilities: The Environmental Legacy of Military Operations, Russell Harmon and J. Ehlen (eds.): Geol. Soc. Am. Engineering Geology Division, v. 14, p. 27-60.

Jacobi, R. D., Fountain, J., Lugert, C., Nelson, T., Smith, G., Mroz, T., and Martin, J., 2003, Identifying Trenton/Black River targets in the northern Appalachian Basin (NYS): Demonstration of integrated exploration tools:, American Assoc. Petrol. Geol. Annual Meeting p. A44.

Jacobi, Robert D., Cruz, Cheri, Leaver, Al, and Fisher, Jodi, 2011, Seismic Signatures of Faults in the Appalachian Basin of NYS, and the Effect of These Faults on Devonian Black Shales: An Update:

Eastern Section AAPG, 2011 Annual meeting (Washington, DC) http://www.searchanddiscovery.com/abstracts/pdf/2011/eastern/abstracts/ndx_jacobi.pdf Accessed 9/29/2011

Jacoby, C. H., 1966, Effect of geology on hydraulic fracturing of salt: 2nd Northern Ohio Geol. Soc. Symp. on Salt, v. 2, p. 311-320.

Jensen, J. R., 2000, Remote Sensing of the Environment - An Earth Resource Perspective Prentice Hall Series in Geographic Information Science: Upper Saddle River Prentice Hall.

Jensen, J. R., 2005, Introductory Digital Image Processing - A Remote Sensing Perspective Prentice Hall Series in Geographic Information System: Upper Saddle River, Pearson Prentice Hall.

Lash, G. G., and Engelder, T., 2006, Jointing within the outer arc of a forebulge at the onset of the Alleghanian Orogeny: Journal of Structural Geology, v. 29, p. 774 - 786.

Lillesand, T. M., Kiefer, R. W., and Chipman, J. W., 2004, Remote Sensing and Image Interpretation: Hoboken, John Wiley and Sons.

McGuire, K., 2007, Fracture, Lineament and Seismic Data: Identification of Fault Patterns in the Appalachian Basin in East-Central New York State. [M.S. thesis]: SUNY University at Buffalo, 324 p.

McGuire, Kelly M., Jacobi, Robert D., Terech, Nicholas, and Agle, Paul, 2006, Integration Of Fracture Patterns And Lineaments For Fault Mapping In The Appalachian Basin Of Central New York State: Geological Society of America, Abstracts with Programs, v. 41, n. 2, p. 69.

Murphy, P. J., 1981, Detachment structures in south-central New York: Northeastern Geology, v. 3, p. 105 - 116.

O'Leary, D. W., and Friedman, J. D., Pohn, H. A., 1976, Lineament, linear, lineation: some proposed new standards for old terms: Geological Society of America Bulletin, v. 87, p. 1463 - 1469

Peña, S. A., and Abdelsalam, M. G., 2006, Orbital remote sensing for geological mapping in southern Tunisia: Implication for oil and gas exploration: Journal of African Earth Sciences, v. 44, no. 2, p. 203-219.

Rahiman, T., and Pettinga, J., 2008, Analysis of lineaments and their relationship to Neogene fracturing, SE Viti Levu, Fiji: Geological Society of America Bulletin, v. 120, no. 11/12, p. 1544-1555.

Sadorsky, P., 2009, Renewable energy consumption, CO2 emissions and oil prices in the G7 countries: Energy Economics, v. 31, no. 3, p. 456-462.

Smith, G.J., and Jacobi, R. D., 2000, Re-evaluating the Canadaway Group: A Revised Stratigraphic Correlation Chart for the Upper Devonian of southwestern New York State: Northeastern Geology and Environmental Sciences; v. 2, p.173-201.

Smith, Langhorne, and Leone, James, 2011, Vertical and lateral extent and TOC content of Middle and Upper Devonian organic-rich shales, New York State: Eastern Section Am Assoc Pet Geol annual meeting (Washington, DC), http://www.searchanddiscovery.com/abstracts/pdf/2011/eastern/90131, accessed 12/1/11

Stroup, Joshua T., Jacobi, Robert, and Nelson, Travis, 2006, Fracture Intensification Domains, Lineaments And Faults In The Skaneateles Lake Region Of The Alleghanian Plateau Of New York State: Geological Society of America, Abstracts with Programs, v. 41, n. 2, p. 69.

Terech, N., 2006, Fracture Patterns, Lineaments and Seismic Reflection Data: Integration for Fault Mapping in the Appalachian Basin of East-Central New York State [M. S. thesis]: SUNY University at Buffalo, 257 p.

Terech, Nicholas, Jacobi, Robert D., McGuire Kelly, and Agle, Paul, 2005, Fracture patterns, lineaments, and seismic reflection data: integration for fault mapping in the Appalachian basin of east-central New York State: Geological Society of America, Abstracts with Programs, v. 37, n. 1, p. 83.

Van Diver, B. B., 2003, Roadside Geology of New York, Mountain Press Publishing Company, 183 - 232.

van Staal, C.R., 2007, Pre-Caroniferous tectonic evolution and metallogeny of the Canadian Appalachians, *in* Goodfellow, W.D., ed., Mineral Deposits of Canada: A Synthesis of Major Deposit-Types, District Metallogeny, the Evolution of Geological Provinces, and Exploration Methods: Geological Association of Canada, Mineral Deposits Division, Special Publication No. 5, p. 793-818.

Wedel, A. A., 1932, Geologic Structure of the Devonian Strata of South-Central New York: New York State Museum Bulletin, v. 294, 73 p.

Zelazny, M. M., 2011, Lineament mapping using remote sensing techniques and structural geology for CO_2 sequestration site characterization in central New York State: University at Buffalo, Unpub MS thesis

Zelazny, M.M., Csatho, B., Jacobi, R.D., 2010, Lineament identification in New York State using remote sensing techniques for geological CO2 sequestration: Geol. Soc. Am. Abstracts with Programs, v. 42., no. 1, p. 121.

Zhao, M., and Jacobi, D. R., 1996a, Formation of regional cross-fold joints in the northern Appalachian Plateau: Journal of Structural Geology, v. 19, no. 6, p. 817 - 834.